ICAF
International Committee on Aeronautical Fatigue and Structural Integrity

Chinese Aeronautical Establishment

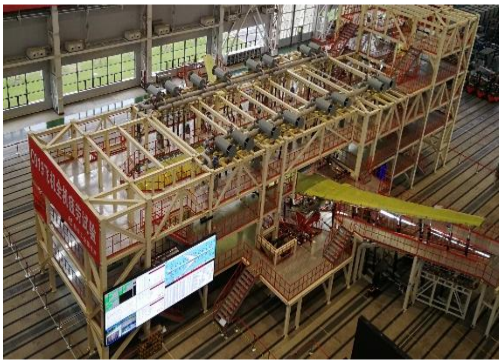
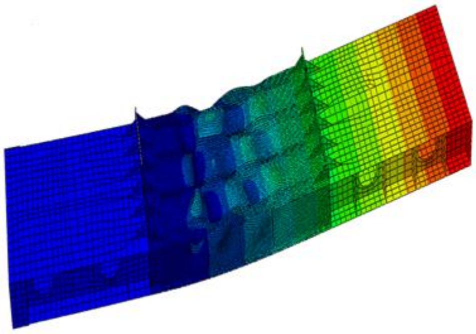


Review of aeronautical fatigue and structural integrity investigations in China during the period June 2021-May 2023

Edited by
SUN Xiasheng
sunxiasheng@cae.ac.cn

Chinese Aeronautical Establishment

CONTENTS

INTRODUCTION 1

1 DIGITAL ENGINEERING 2

1.1 Design and Prediction of Aircraft Structural Strength Performance Based on Digital Twin 2

1.2 Helicopter Fuselage Rectifier Vibration Fatigue Simulation and Test Verification 4

1.3 Digital Twins Technology for Static Strength of Aircraft Structures 6

1.4 Simulation of Flight Flutter Test Excitation Response and Flight Test Application Technology 9

2 FATIGUE CRACK GROWTH AND LIFE PREDICTION METHODS 11

2.1 3D SIFs of Complex Crack Configurations Emanating from Hole 11

2.2 Interior Initiation and Early Growth of Very High Cycle Fatigue Crack in An Additively Manufactured Titanium Alloy 14

2.3 Residual Stress Effects on Crack Propagation Behavior in Welded Integral Aircraft Structure under Biaxial Loading 16

2.4 Kernel Ridge Fatigue Life Prediction Approach for Laser-Directed Energy Deposition Ti-6Al-4V Alloy Based on Pore-Induced Failures 18

3 FATIGUE LIFE ENHANCEMENT METHODS AND REPAIR SOLUTIONS 21

3.1 Gas-pore Effects on Fatigue Lifetime of AM metals by Peridynamics 21

3.2 Study on the Influence of the Shot Peening Forming and Reinforcement Technology on the Fatigue Performance of Panel Structure 23

3.3 Analysis and Optimization of Damage Tolerance of Large Aperture Cold-Expanded Bushing Lug 25

4 STRUCTURAL HEALTH / LOADS MONITORING 27

4.1 Intelligent Fleet Life Management Based on Structural Health Condition 27

4.2 Euclidean Space Method for Distributed Load Recovery from Strain Measurements 29

4.3 Research on the Method of Aircraft Load Prediction and Strain Prediction of Key Structures Based on Machine Learning 31

4.4 Application of Structural Health Monitoring Technology for Full-Scale Fatigue Test 33

5 NDI, INSPECTIONS AND MAINTENANCE 36

5.1 Multi-frequency Ultrasonic Testing Method for Three-Dimensional Woven Composites 36

5.2 Intelligent Radial Image Recognition of Aircraft Structure Damage Based on Deep Learning 38

6 STRUCTURAL INTEGRITY OF COMPOSITE LAMINATES 41

6.1 Study on Buckling and Post-Buckling Design and Analysis Method of Multi-wall Composite Plate 41

6.2 Low-load Omission for Composite Structure Fatigue Test 42

6.3 Static and Fatigue Research on Damage Failure Analysis and Evaluation Model of Composite Horizontal Tail Rib Structure 45

6.4 Rationalized Improvement of Tsai–Wu Failure Criterion Considering Different Failure Modes of Composite Materials 48

6.5 Post-buckling failure analysis of composite stiffened panels considering the mode III fracture 49

6.6 Interaction Formulae for Buckling and Failure of Orthotropic Plates Under Combined Axial Compression/Tension and Shear 51

7 ADVANCED MATERIALS AND INNOVATIVE STRUCTURAL CONCEPTS 53

7.1 Experimental Study on Mechanical Properties of Laser Powder Bed Fused Ti-6Al-4V Alloy Under Post-Heat Treatment 53

7.2 Integral Analysis of Additive Manufacturing Ti6Al4V Titanium Structure 57

8 FULL-SCALE STRUCTURAL TESTING 59

8.1 Crashworthiness pyramid test technology of double passageway composite fuselage structure 59

8.2 Fatigue Design and Test Technology of Helicopter Spherical Flexible Rotor Hub 61

8.3 Rigid Loading Accelerates Full-Scale Aircraft Fatigue Test 64

8.4 Widespread Fatigue Damage Test and Evaluation of Equally Straight Section in Fuselage 67

INTRODUCTION

This review is a summary of the aeronautical fatigue and structural integrity investigations carried out in China during the period June 2021 to May 2023. The review will be presented at the 38th conference of the International Committee on Aeronautical Fatigue and Structural Integrity（ICAF） in the Netherlands and published online on ICAF website.

The topics covered in this review include:

1 Digital engineering
2 Fatigue crack growth and life prediction methods
3 Fatigue life enhancement methods and repair solutions
4 Structural health / loads monitoring
5 NDI, inspections and maintenance
6 Structural integrity of composite laminates
7 Advanced materials and innovative structural concepts
8 Full-scale fatigue testing

The contribution of summaries by Chinese aviation manufacturers, research institutes, universities was voluntary, and is acknowledged with sincere appreciation by the author of this review.

The contributions generously provided by following contributors:

1 AVIC Aircraft Strength Research Institute
2 AVIC Shenyang Aircraft Design & Research Institute
3 AVIC Chengdu Aircraft Design & Research Institute
4 AVIC The First Aircraft Institute
5 AVIC Helicopter Research and Development Institute
6 AVIC Flight Test Establishment
7 COMAC Shanghai Aircraft Design & Research Institute
8 AECC Beijing Institute of Aeronautical Materials
9 Institute of Mechanics, Chinese Academy of Sciences
10 Northwestern Polytechnical University
11 Beihang University
12 Shanghai Jiao Tong University

1 DIGITAL ENGINEERING

1.1 Design and Prediction of Aircraft Structural Strength Performance Based on Digital Twin [1]

At present, the structural strength design of aircraft is still using the traditional "design, manufacturing and test" model established decades ago. The main drawbacks of this traditional development model are as follows：

- The design, manufacture, verification, and use of the aircraft are separated from each other, and the product data and information are managed in isolation, and it is difficult to analyze the causes and trace the problems arising from the development;
- The aircraft service environment is harsh, but the design has made a lot of simplifications for the real multi-physics use environment/load, which cannot fully reflect the process experienced by the aircraft after service, and the traditional load spectrum design method is not accurate enough;
- The simulation model used in aircraft design can only reflect the common features of the aircraft, but cannot reflect the individual differences of physical entities. Therefore, the analysis results can only measure the average level of the aircraft group, and cannot accurately predict the individual performance of the aircraft;
- Due to the failure to build a system model in the digital space, verification and confirmation cannot be carried out in each development and design stage, and a large number of integration and verification work can only be carried out in the physical stage of the whole system, which increases the design and development risk and prolongs the development cycle.

In order to solve the shortcomings of the traditional aircraft flight capability design technology, it is urgent to establish a digital model that can fully express the real-time flight capability of the aircraft, carry out the comprehensive design and simulation of the structure platform system across disciplines and stages, and carry out the physical entity of the aircraft with the digital twin in the digital domain. "Real-time mapping" transforms from a traditional aircraft verification system based on physical tests to a virtual-real verification system based on digital twins.

key technology

By breaking through key technologies such as parametric mapping, multi-scale structural modeling, multi-physics load twinning, and uncertainty control, high-fidelity simulation models are built in the design stage; Realize the mapping of digital twins and physical entities in the structural manufacturing stage; by breaking through the intelligent reduced-order performance prediction technology, realize real-time rapid performance prediction in the use stage of aircraft structures.

Make full use of big data information at all stages of design, manufacturing, use, and maintenance, and combine the development results of emerging technologies such as artificial intelligence to build a high-fidelity digital twin to accurately predict the strength/stiffness characteristics of aircraft structures and effectively evaluate aircraft flight operations ability.

---

[1] AVIC Shenyang Aircraft Design & Research Institute

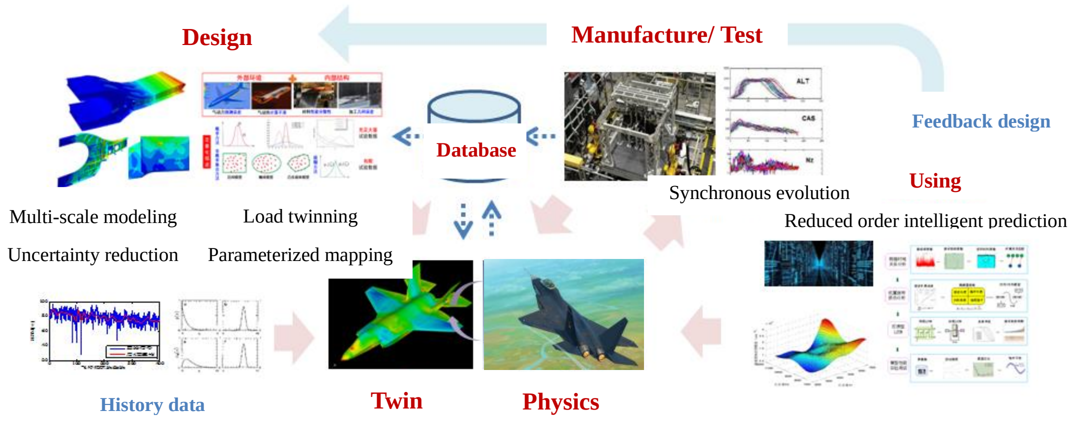

Figure 1: The process of design and prediction of aircraft structural strength performance based on digital twin

Achievements

By studying the multi-scale modeling technology of the key parts of the structure, the digital twin model can realize the panoramic description of the macroscopic and detailed characteristics of the physical entity, and ensure the accurate characterization of the initial defects, fatigue cracks, delamination, and other damages of the aircraft. Taking a key structural test piece as an example, it is divided into three parts: the loading section, the fixed section, and the fatigue box section. The edge strip in the box section has nail holes, which are vulnerable to fatigue damage. The edge strip is selected as the key structure. When performing finite element analysis, the sub-model of key parts will automatically extract the displacement boundary of the component-level model for analysis and calculation, which improves the analysis accuracy of finite element analysis.

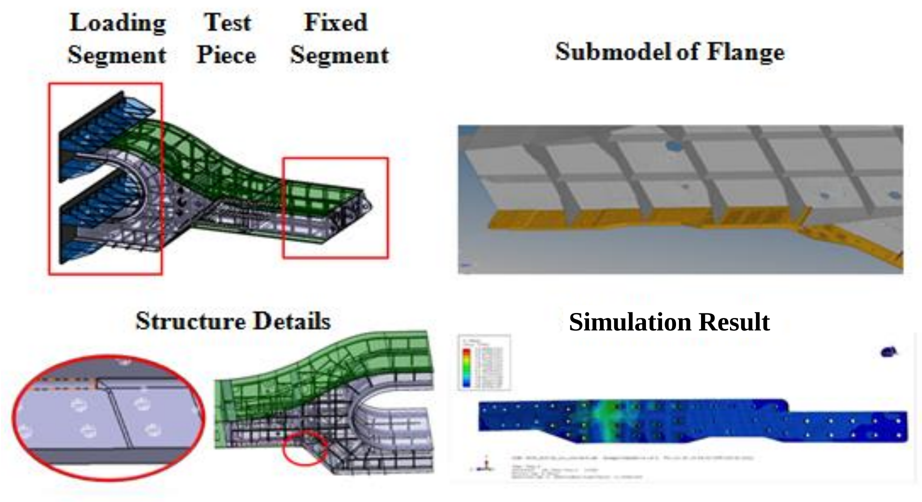

Figure 2: Multi-scale model construction

Based on the measured big data, this technology can realize the high-precision and high-efficiency prediction of the structural life, and obtain the life prediction results with the corresponding reliability level. Taking the stress spectrum and structural parameters at the location of the nail hole as the input, and the crack growth data as the output, the artificial intelligence prediction model is trained. Finally, the prediction results meet the requirements.

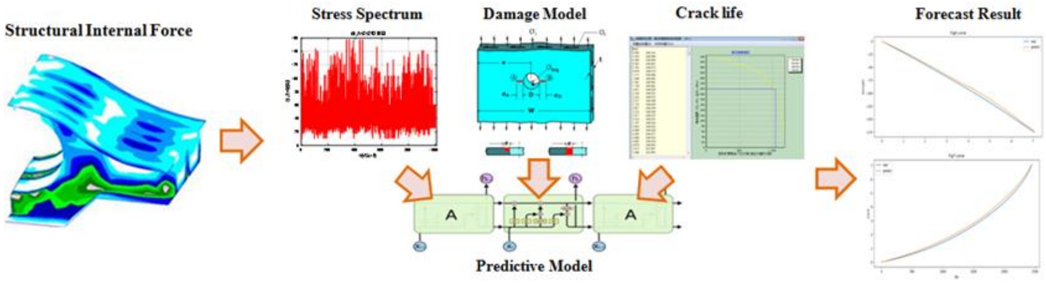

Figure 3: The process of AI prediction

1.2 Helicopter Fuselage Rectifier Vibration Fatigue Simulation and Test Verification [2]

Static aerodynamic loads and structural vibration excitation act on the rectifier. The rectifier is located on the tail of the helicopter and its vibration load consists of a broadband random vibration load and several single frequency harmonic excitations such as main rotor, tail rotor and drive shaft. Figure 4 shows the typical helicopter vibration environment spectrum. The finite element model of the rectifier is shown in Figure 4. Pre-stress modal analysis is performed after applying pressure field caused by aerodynamic calculation. The result of pre-modal analysis shows that the fourth-order modal frequency of the rectifier is close to a certain order of fixed frequency excitation in the vibration environment spectrum, and the modal vibration pattern is shown in Figure 5 a). The maximum local stress in this mode is in the hinge, as shown as Figure 5 b). The stress response of the hinge was calculated using random vibration analysis, and the stress curve of the node at the hazardous part of the hinge is shown in Figure 6. The fatigue life of the hinge is calculated in the commercial program FE-SAFE by using the aluminum alloy bending vibration fatigue S-N curve as the input.

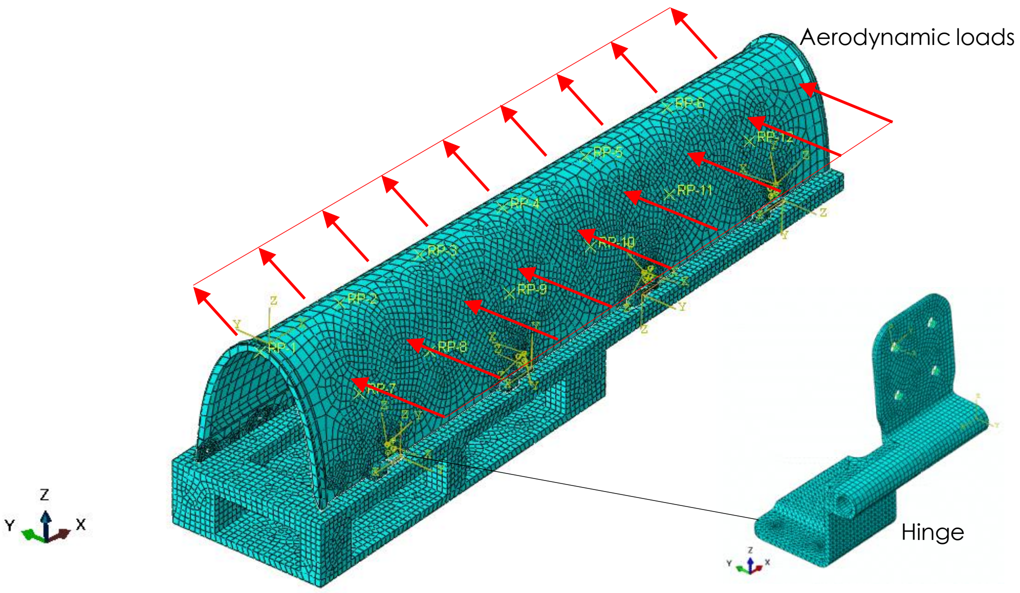

Figure 4: Finite element model of helicopter fuselage rectifier

[2] AVIC Helicopter Research and Development Institute

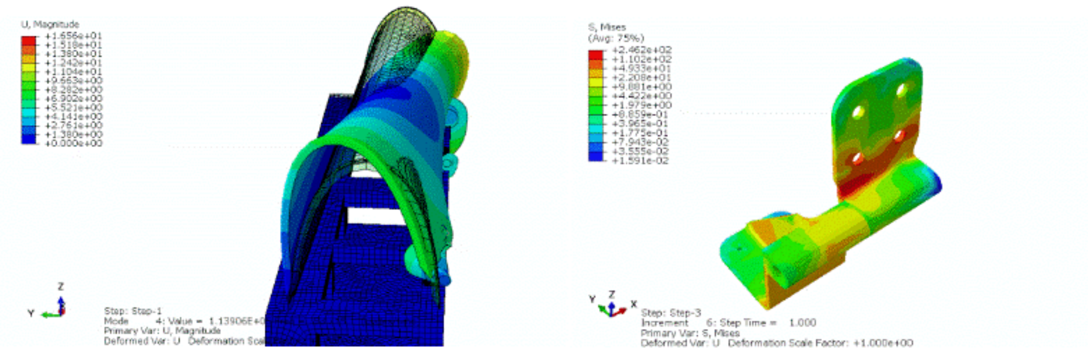

a) Fourth-order modal pattern　　b) modal stress clouds of the hinge

Figure 5: Major mode formations and modal stress distribution of hinge

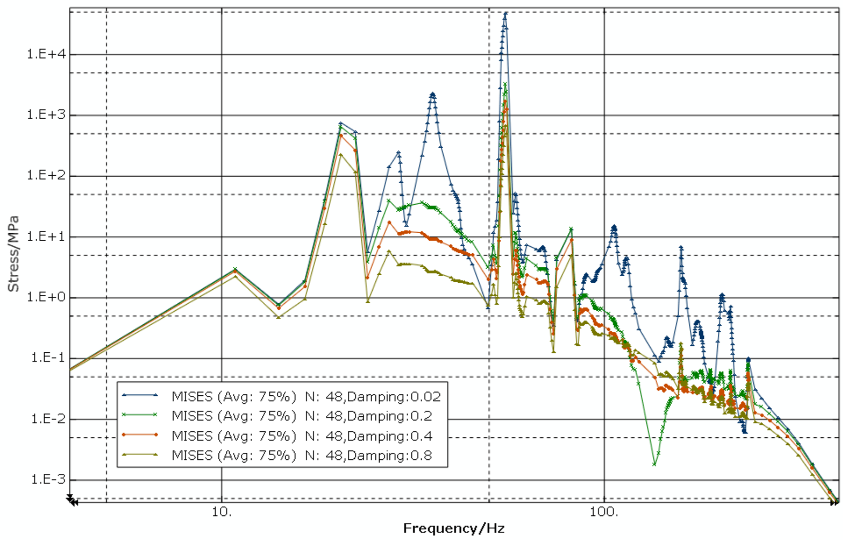

Figure 6: Random vibration analysis of hinge stress in hazardous areas

Compound loading vibration fatigue test verification

In order to verify the simulation results of failure mode and fatigue life for the rectifier, a compound loading vibration fatigue test was conducted, and the test principle is shown in Figure 7. Vibration load is applied by using the horizontal slide of the shaker. Distributed aerodynamic loads are simulated by applying tape to the inner and outer surfaces of the rectifier. The application of static loads in vibration fatigue testing needs to minimize the change in the inherent properties of the structure, so this test uses rubber ropes with an inherent frequency much lower than the inherent frequency of the structure arranged tandem in the static load loading system. The photo of the test is shown in Figure 8 a). The Rectifier hinge was damaged after 660s of testing, and a photo of the hinge damage is shown in Figure 8 b). The test results are consistent with the failure modes predicted by the simulation analysis, and the error between the simulation analysis fatigue life and test results is acceptable, with a life error of 14% after taking the logarithm.

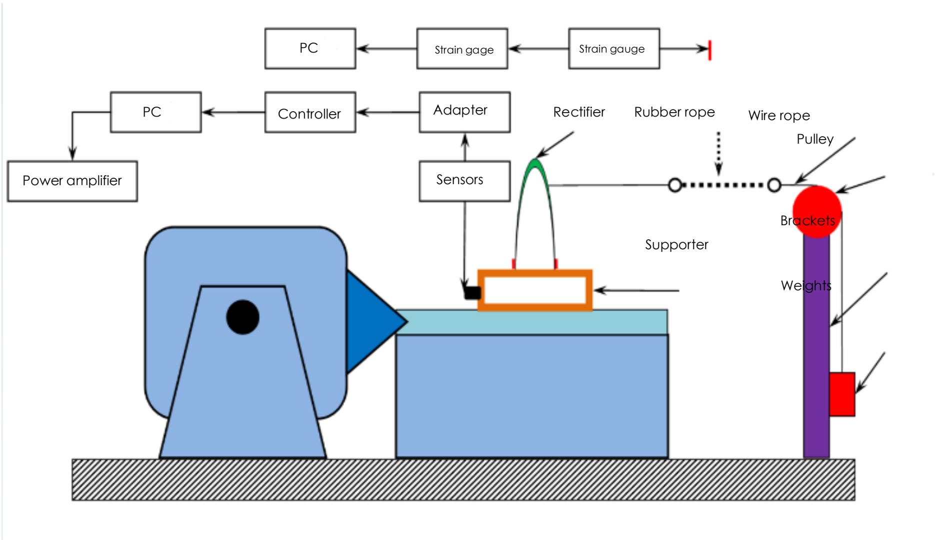

Figure 7: Loading, control, and measurement principal diagram

a) Test site photo

b) Hinge damage area after test

Figure 8: Helicopter fuselage rectifier compound loading vibration test photos

1.3 Digital Twins Technology for Static Strength of Aircraft Structures[3]

Strength Digital twin is a real-time fusion community of shared characteristics of strength digital model and unique personality of aircraft physical entity for whole life cycle. Recently, aiming at Digital twins for static strength of aircraft structures, some studies are carried out from the aspects of high-precision model construction, Virtual testing, Simulation based on Augmented reality and Data mining. Through virtual and real interactive feedback, data fusion analysis, decision selection optimization and other means, new capabilities are added or extended for physical entities.

Several key techniques have been successfully solved in High-precision model construction and Virtual testing, including validation technique for aviation typical structures considering uncertainty, multi-scale model boundary and load conversion, high precision progressive failure analysis of typical structures.

The targets of the developed technology is to accurately describe the true strength performance of the test component considering uncertainty based on the constructed accurate multi-scale model, predict the

[3] AVIC Aircraft Strength Research Institute

failure response of the component under complex load conditions, and eliminate potential test risks in advance.

High precision progressive failure analysis technology

Due to the anisotropic characteristics of composite materials, the stability of composite panel is more complicated. In order to accurately simulate the progressive failure process of composite laminates, the progressive failure analysis method based on the testing of mechanical properties for composite is established. The solution process includes three parts: material initial damage detection, material damage evolution and nonlinear FE solution. Failure analysis requires failure criteria to describe the material state and predict material failure. Material property degradation must establish a stiffness degradation model to describe the stiffness characteristics of a material after damage. Both of them are very important for accurately predicting the damage state and loading characteristics of composites.

The failure criterion applicability of domestic large aircraft material system is studied based on the failure envelope and component experimental data. The failure parameters available in engineering analysis are recommended. At the same time, referring to the Mohr-Coulomb criterion, an improved Hashin criteria considering the in-situ effect of composite laminates and the transverse stress component on the shear strength of the matrix is proposed. Also a concise strategy for determining the stiffness degradation coefficient based on the damage state of the matrix and the degree of fiber damage is presented. The failure process of hat-shaped panels of civil aircraft under compression is simulated (see Figure 9), and the analysis results coincide with test data.

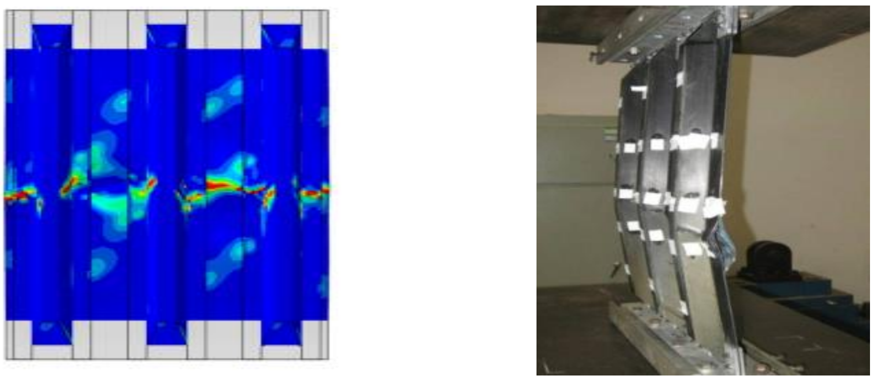

a) Progressive failure analysis results b) Physical test results

Figure 9: Progressive failure analysis of Hat-stiffened panel

Multi-scale model boundary and load conversion technology

In the framework of virtual testing for aircraft structure, multi-scale model boundary and load conversion describes the process of coupling different analysis models in different scales and fidelity. This approach requires an initial prediction of the mechanical response of the full-scale structure by a nonlinear model and then used to define the driving boundary conditions for the next scale model. The multi- scale analysis framework discussed in this paper is an organic fusion of traditional sub-model technique and unmatched multi-grid technique. It is divided into five levels according to the analysis target to realize the rapid transformation of high-fidelity analysis model. Its framework is shown in the Figure 10:

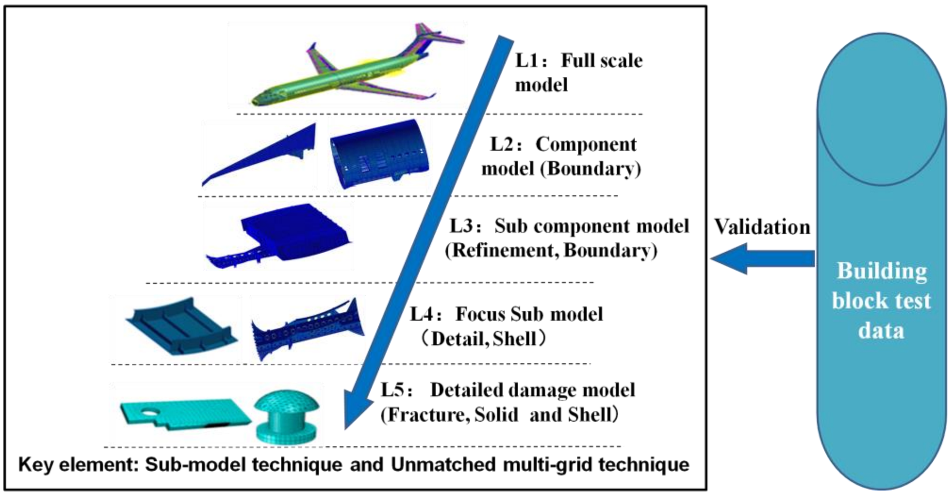

Figure 10: Multi-scale analysis framework

The main purpose of the global model is to provide definitions of boundary conditions for the next scale model. The ultimate failure of complex structures usually occurs at local sites, and the overall structure tends to be in the elastic state. In order to solve the nonlinear damage analysis problem of structural region accurately and efficiently, a so-called unmatched multi-grid (UMG) technology is formed. In the multi-scale model conversion based on UMG technology, a reasonable partition interface is selected, and a simple and effective non-matching interface data transfer method based on the basic theory of multi-grid method is given by using radial basis function interpolation. Figure 11 shows the application of UMG technology in the failure analysis of an aileron connection structure. The errors of stress and failure load estimated by the refined analysis model is less than 10% compared with the test.

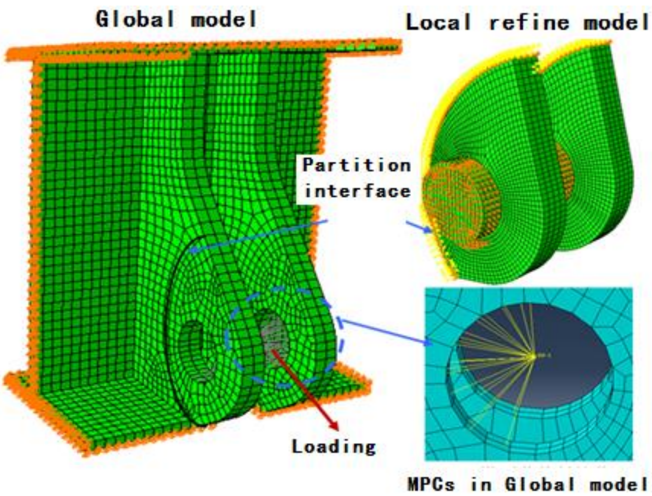

Figure 11: Application of UMG technology in aircraft structure

Application

Aiming at the high load test of a composite wing box structure, the multi-scale static strength model was constructed. The correlation coefficient between the verified model and the experimental strain value is greater than 0.9. At the same time, the progressive failure analysis was conducted before the experiment, estimating the dangerous parts and failure modes of the structure. Real time monitoring and abnormal fault feedback were conducted during the experiment to ensure the safety of the box section test. The typical application of technology is shown in Figure 12.

a) Test wing box structure

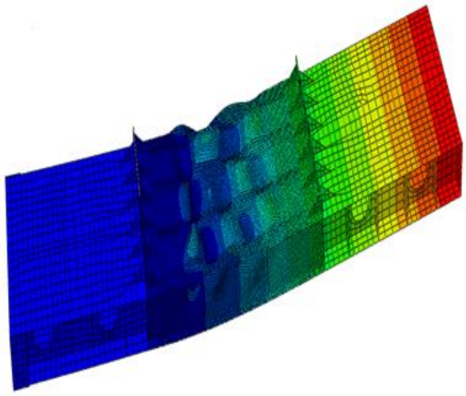

b) Validated analysis model

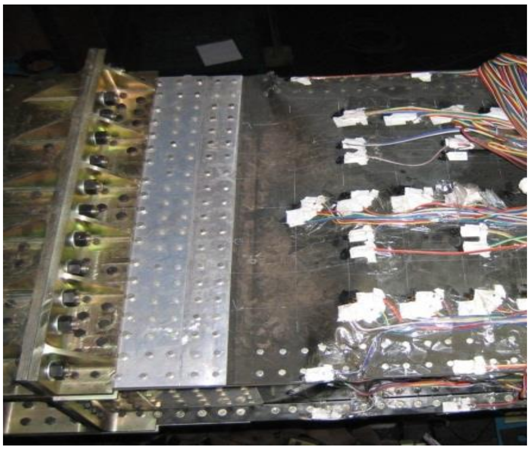

c) Damage location and failure mode

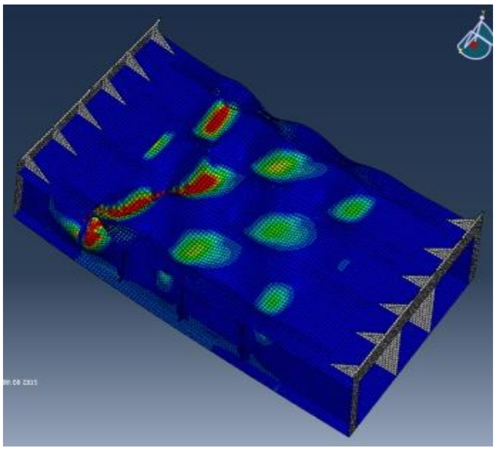

d) Progressive Failure Analysis Results

Figure 12: Typical applications in the composite wing box structure failure test

1.4 Simulation of Flight Flutter Test Excitation Response and Flight Test Application Technology[4]

Based on the finite element model of aircraft structural dynamics, the simulation model of excitation response in flight flutter test is established, and the analysis and research of sensor location optimization, excitation method optimization, excitation response amplitude prediction and flutter boundary prediction are carried out. The simulation results are compared with flight test results, and the response simulation of flight flutter test is analyzed to promote flight test. The simulation of excitation response of flight flutter test will further improve the design level of current flight flutter test, improve the efficiency of flight flutter test, and ensure the safety of flight test.

The full aircraft structural dynamics finite element model of the aircraft adopts the underwing engine and conventional tail layout. Figure13 shows the full aircraft structural dynamics finite element model.

[4]AVIC Flight Test Establishment

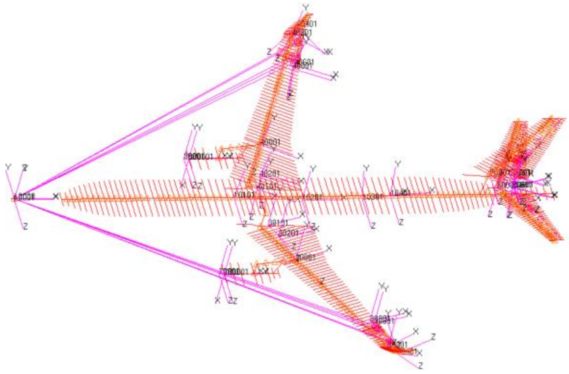

Figure 13: Finite element model of aircraft

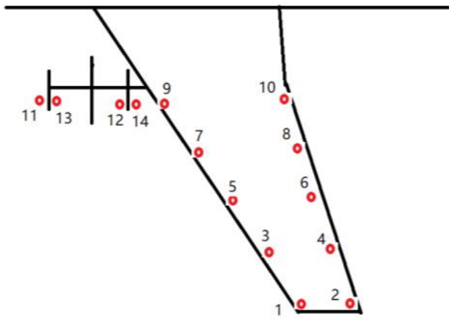

Figure 14: Schematic diagram of measuring points

The location of vibration sensor in flight flutter test should be sensitive to the structural mode to be measured, to better use the test data for structural modal parameter identification. Taking the position arrangement of sensors on the left wing as an example, first arrange 10 measuring points on the left wing of the whole aircraft model, as shown in Figure 14. The control surface sweep excitation model is used for excitation simulation, and the response characteristics under excitation at each position of the model can be analyzed, as shown in Figure 15 The position and number of sensors are optimized by comparing the response characteristics of different measuring points on the leading edge of the wing. Finally, only three vibration sensors are arranged on the leading edge of the wing, as shown in Figure 16.

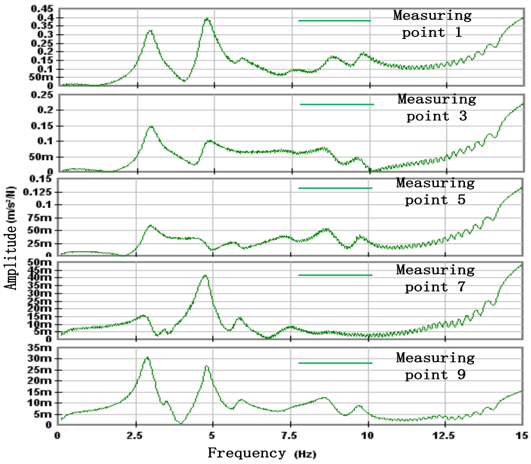

Figure 15

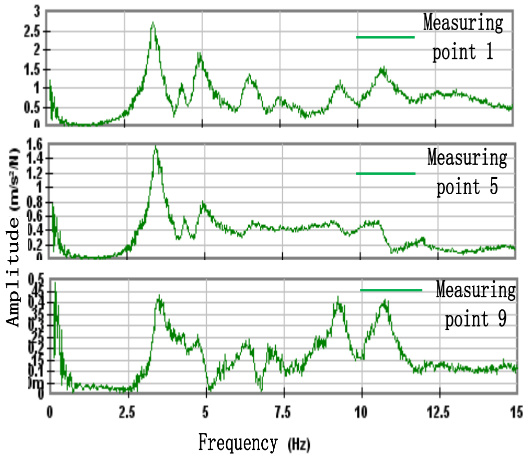

Figure 16

Figure 15: Simulation results of frequency response characteristics of model measuring points

Figure 16: Flight test results of frequency response characteristics of wing leading edge measuring points

The simulation model of excitation response is used to design various excitation methods and analyze the excitation effect. Table 2 shows the modal excitation results of each measuring point of the underwing engine nacelle obtained according to different excitation methods. It can be seen from the table that the modal of the engine nacelle can be obtained not only by the aileron, but also by the elevator and rudder, which provides an important basis for the excitation scheme design and data analysis.

Table 1: Excitation response results of each measuring point under different excitation

Modal	Aileron antisymmetric excitation	Aileron symmetric excitation	Elevator excitation	Rudder excitation
Anti symmetrical pitch of engine nacelle	√			√
Symmetrical side deflection of engine nacelle		√	√	
Symmetrical side deflection of engine nacelle		√	√	
Anti symmetrical side deflection of engine nacelle	√			√
Engine nacelle symmetrical rolling		√	√	
Anti symmetrical rolling of engine nacelle	√			√

Figure 17 shows the flight flutter test excitation results of different excitation methods. Using the test points of modal excitation of elevator and rudder to engine nacelle, better flight test results are obtained than those of aileron excitation.

Using the established simulation model of control surface sweep excitation response, the structural response amplitude can be predicted. Figure 18 shows the comparison between flight test and simulation results of wing tip leading edge vibration value changing with the increase of velocity pressure when the control surface is swept.

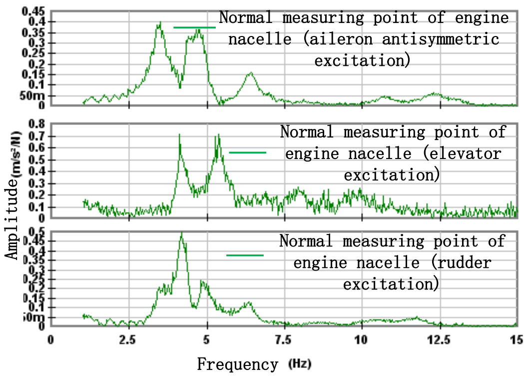

Figure 17

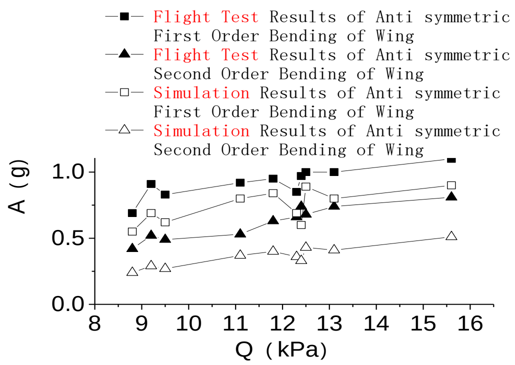

Figure 18

Figure 17: Flight test results of different excitation methods

Figure 18: Response amplitude of aileron sweep excitation

2 FATIGUE CRACK GROWTH AND LIFE PREDICTION METHODS

2.1 3D SIFs of Complex Crack Configurations Emanating from Hole [5]

3D SIFs of complex hole-edge cracks are obtained using the slice synthesis weight function method. The SIFs of unsymmetric corner cracks, unsymmetric and eccentric surface cracks and complex corner-

[5] Shanghai Jiao Tong University

surface cracks emanating from an open hole are obtained. 3D SIFs of part-through crack emanating from an open hole and pin-loaded hole of lug in a general case are also obtained by the present SSWFM. The accuracy of the obtained 3D SIFs is verified by comparing with conventional FEM/Franc3D. The efficiency of the method is about 500 times faster than FEM/Franc3D. This will greatly enhance the fatigue crack growth prediction capability for engineering structures.

Based on slice synthesis weight function method, the 3D SIFs at a given parametric angle φ, $K(\varphi)$, is

$$K_j(\varphi)=\frac{1}{1-\eta^2}\left\{K_{cj}^4\left(c_{yl},c_{yr}\right)+\left[\frac{E_j}{E_{sj}}K_{aj}\left(a_{xj}\right)\right]^4\right\}^{1/4}(-1)^n,\ j=l,\ r \tag{1a}$$

$$E_{s_j}=E_j\left(\frac{\Phi_j}{1-\nu^2}-1\right)\frac{c_j}{a_j},\ a_j/c_j\le 1;\quad E_{s_j}=E_j\left(\frac{\Phi_j}{1-\nu^2}-\frac{c_j}{a_j}\right),\ a_j/c_j>1 \tag{1b}$$

$$\Phi_j=\left[1.0+1.464\left(a_j/c_j\right)^{1.65}\right]^{1/2},\ a_j/c_j\le 1;\quad \Phi_j=\left[1.0+1.464\left(c_j/a_j\right)^{1.65}\right]^{1/2},\ a_j/c_j>1 \tag{1c}$$

where φ is the parametric angle at a point along the crack front. The subscript 'j' represents left or right crack of the hole. E and E_s are Young's modulus of the basic slice and spring slice, c_y and a_x are crack length of basic slice and spring slice, respectively. $\eta=0$ for free surface and $\eta=\nu$ for points inside the body. $n=2$ for $K_i>0$ ($i=a$, c), otherwise $n=1$. K_c and K_a are SIFs of the basic and spring slices, which can be obtained by the 2D WFM Eqs.(2a) and (2b), respectively.

$$\begin{aligned}K_{cj}(c_{yl},c_{yr})=&\int_0^{c_{yl}}\left[\sigma_l(x,y)-S_l(x,y)\right]\cdot m_{cj}\left(c_{yl},c_{yr},r,x\right)\mathrm{d}x\\&+\int_0^{c_{yr}}\left[\sigma_r(x,y)-S_r(x,y)\right]\cdot m_{cj}\left(c_{yl},c_{yr},r,x\right)\mathrm{d}x\end{aligned} \tag{2a}$$

$$K_{aj}(a_{xj})=\int_0^{a_{xj}}S_j(x,y)m_a\left(a_{xj}/t,y/t\right)\mathrm{d}y \tag{2b}$$

where $\sigma_l(x,y)$ and $\sigma_r(x,y)$ is the stress distribution at the crack location in the un-cracked body subjected to external load. m_c is the 2D weight function of main slice and m_a is the 2D weight function of spring slice.

The 3D SIF results of part-through cracks emanating from open hole and pin-loaded hole are given as follows, the results by FEM/Franc3D and existing literature are also given for comparison purpose. The results from the present SSWFM shows high accuracy with good efficiency.

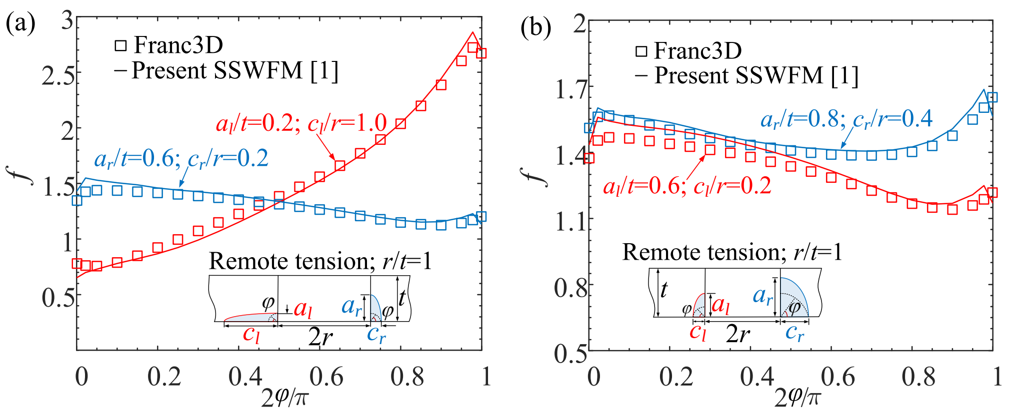

Figure 19: SIFs of two unsymmetrical corner cracks at a hole under remote tension (r/t=1): (a) a_l/t=0.2; c_l/r=1.0; a_r/t=0.6; c_r/r=0.2; (b) a_l/t=0.6; c_l/r=0.2; a_r/t=0.8; c_r/r=0.4.

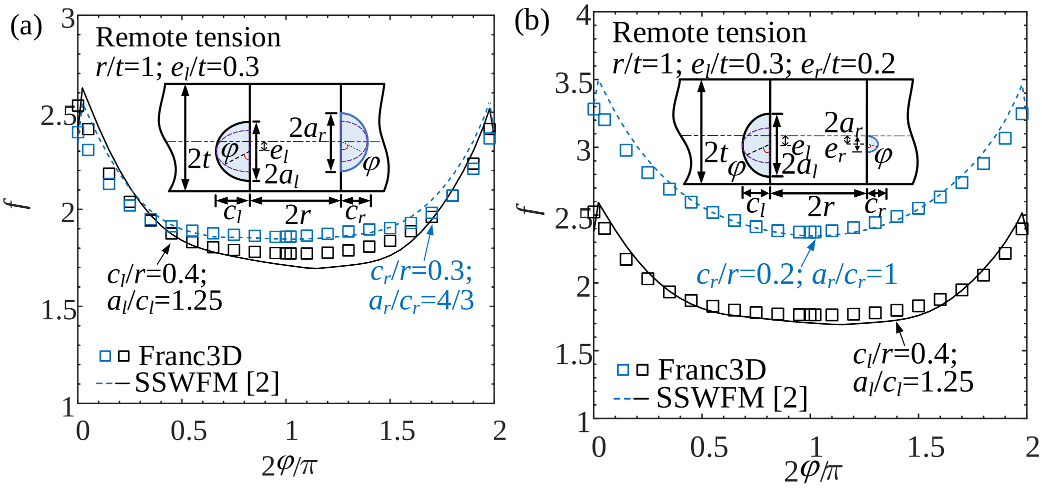

Figure 20: SIFs of two eccentric and asymmetric surface cracks under remote tension (r/t=1): (a) c_l/r=0.4, a_l/c_l=1.25, e_l/t=0.3, c_r/r=0.3, a_r/c_r=4/3; (b) c_l/r=0.4, a_l/c_l=1.25, e_l/t=0.3, c_r/r=0.2, a_r/c_r=1, e_r/t=0.2;

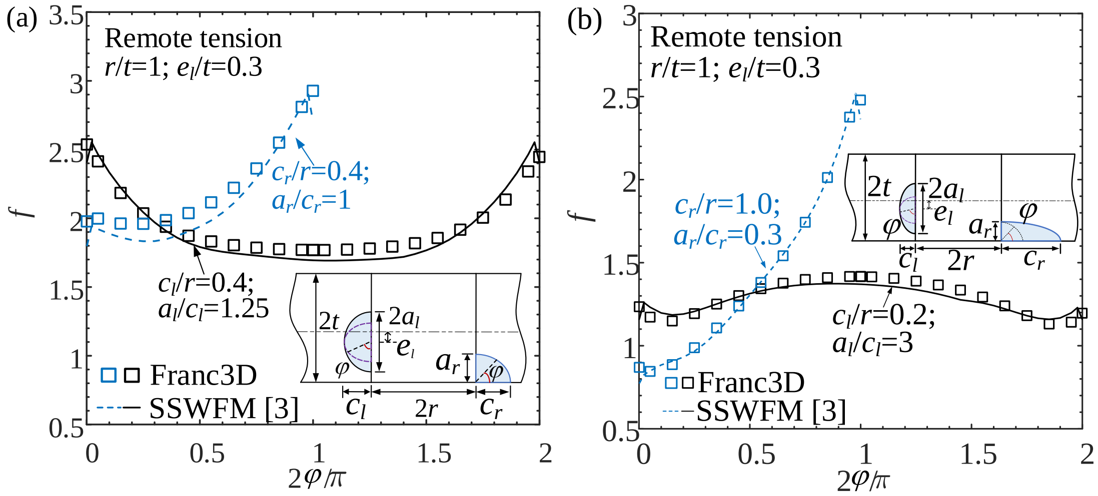

Figure 21: SIFs of surface-corner cracks under remote tension (r/t=1): (a) c_l/r =0.4, a_l/c_l=1.25, e_l/t=0.3, c_r/r=0.4, a_r/c_r=1; (b) c_l/r=0.2, a_l/c_l=3, e_l/t=0.3, c_r/r=1, a_r/c_r=0.3.

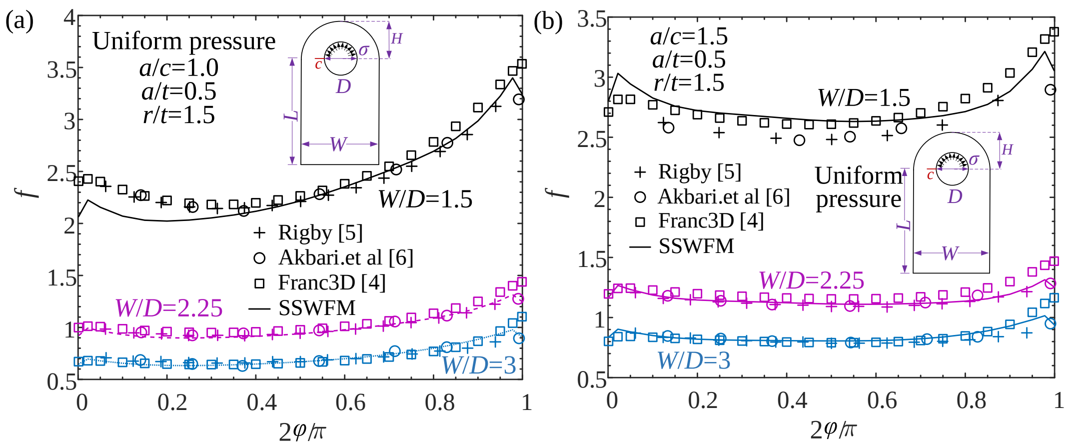

Fig.4 SIFs of single corner crack emanating from an open hole of lug under uniform pressure load on the hole (W/D=1.5; a/t=0.5; r/t=1.5): (a) a/c=1.0; (b) a/c=1.5.

2.2 Interior Initiation and Early Growth of Very High Cycle Fatigue Crack in An Additively Manufactured Titanium Alloy [6]

Additively manufactured (AM) titanium alloys have potential use in aerospace, biomedical and nuclear industries. Some of the components suffer from very high cycle fatigue (VHCF) loadings in service. Differing from the conventionally processed titanium alloys, the AM titanium alloys usually contain defects such as gas porosity or lack of fusion due to the manufacturing process. The defects generally act as the crack origin and lower the fatigue performance of the AM titanium alloys. Hence, it is essential to explore the interior defect induced crack initiation and evolutionary process for VHCF of AM titanium alloys, which will be of great help in the fatigue life evaluation of component parts.

Materials and methods

The material used is an AM Ti-6Al-4V alloy, which was made by the selective laser melting technology on a BLT-S310 machine. The fatigue tests were conducted on an ultrasonic fatigue test system USF-2000A (f = 20 kHz) in air and at room temperature. The stress ratio is -1. The two-step variable amplitude fatigue tests were used, which started from a block of lower stress amplitude $\sigma_{a,L}$ with loading cycles n_L, and then was followed by a block of higher stress amplitude $\sigma_{a,H}$ with loading cycles n_H, except that two specimens experience at first a number of constant amplitude loadings. This loading sequence was repeated until the specimen failed. The detailed information for the two-step variable amplitude loadings of specimens is shown in Table 1. The fracture surface was observed by scanning electron microscope.

Table 2: Loading Information of Specimens under Variable Amplitude Loadings

Specimen No.	$\sigma_{a,L}$ (MPa)	n_L (Cycle)	$\sigma_{a,H}$ (MPa)	n_H (Cycle)	Cumulative Cycles at $\sigma_{a,L}$	Cumulative Cycles at $\sigma_{a,H}$
1	400	3.0×10^6	600	4.0×10^3	5.4×10^7	6.9×10^4
2	400	3.0×10^6	600	4.0×10^3	1.6×10^8	2.1×10^5
3*	350	5.0×10^6	600	4.0×10^3	7.3×10^8	3.4×10^5
4*	350	1.0×10^7	625	4.0×10^3	6.3×10^8	1.7×10^5

*It experiences at first a few constant amplitudes loading σ_a = 350 MPa with 3×10^8 cycles for specimen 3 and 2×10^8 cycles for specimen 4, respectively.

Results

The "tree ring" marks (i.e., difference of morphology characteristic) left on the fracture surface provide the information for the intermediate process of the interior crack initiation and early growth, and make it possible to estimate the equivalent crack growth rate for the interior crack initiation and early growth. For the calculation of the equivalent crack growth rate, the fatigue cracks after and before the block of the lower stress are approximately seen as concentric penny cracks, and the radii in the crack extension with relative clear marks are considered, as shown in Figure 22.

---

6 Institute of Mechanics, Chinese Academy of Sciences

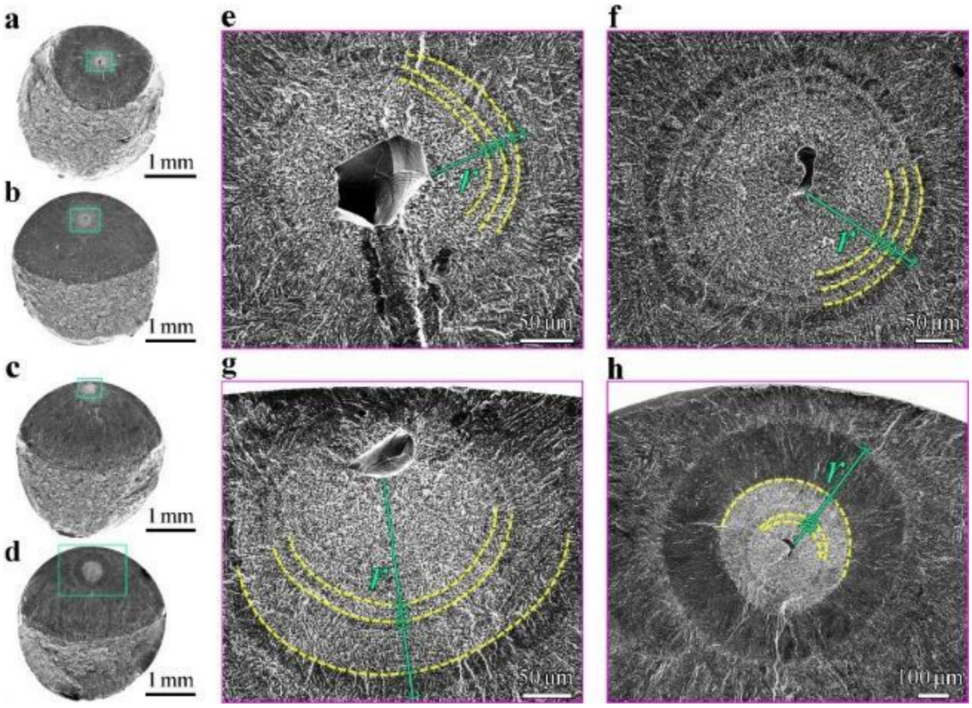

Figure 22: Tree Ring Like Pattern on Fracture Surface under Variable Amplitude Loadings. (a) and (e) Specimen 1. (b) and (f) Specimen 2. (c) and (g) Specimen 3. (d) and (h) Specimen 4. The Dashed Lines Denote the Marks Where a Block of the Lower Stress is Changed to a Block of the Higher Stress, and the Arrows Denote the Radii of Approximately Concentric Penny Cracks for Measurement

Figure 23 shows that the equivalent crack growth rate in crack initiation and early growth stage is much lower than 10^{-10} m/cycle. The ultralow crack growth rate indicates that the crack does not grow in all directions at each loading cycle in the crack initiation and early growth stage in VHCF regime, which extends at first in some local regions after a number of cycles.

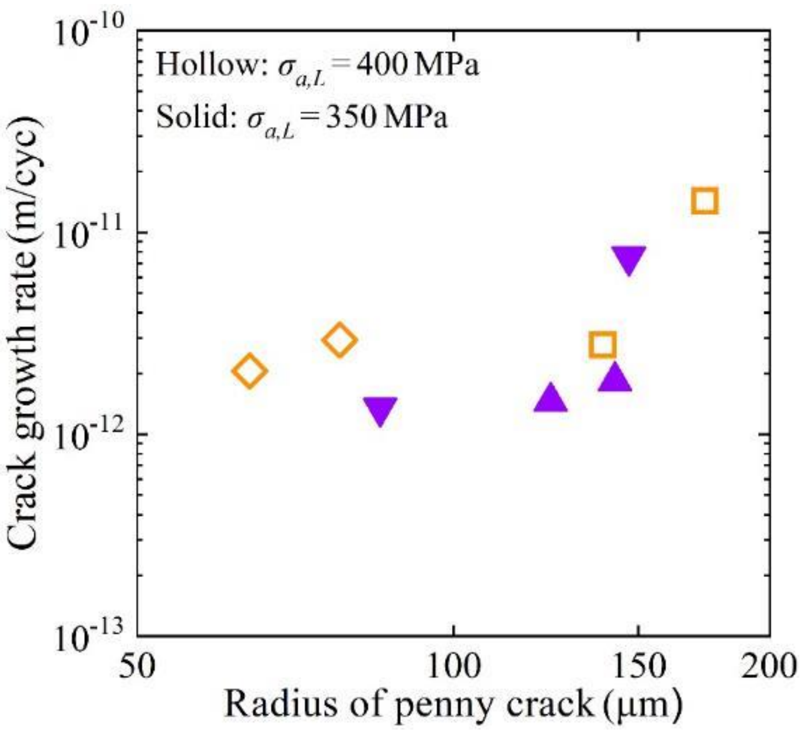

Figure 23: Crack growth rate VS penny crack radius

2.3 Residual Stress Effects on Crack Propagation Behavior in Welded Integral Aircraft Structure under Biaxial Loading [7]

The main conclusions of this study are as follows. In most of the cases, the crack deviation from the initial crack is mainly affected by residual stress at the beginning of crack propagation. The variation of crack path is strongly linked with the residual stress as well as the biaxial loading ratio. In addition, K_I and K_{II} are susceptible to residual stress under biaxial loading conditions. Residual stresses contribute to a higher proportion of K_{II} compared to that of K_I. K_I and K_{II} in the retreating side are more affected by the residual stress.

Material and sample preparation

A 2.286 mm thick 7075-T6 Al alloy sheet is selected. Two plates were welded by FSW-RL31-010 machine in our university. After welding, the as-welded plate was cut into the cruciform shape with the overall length or width of 320 mm, as shown in Figure 24(a) and (b).

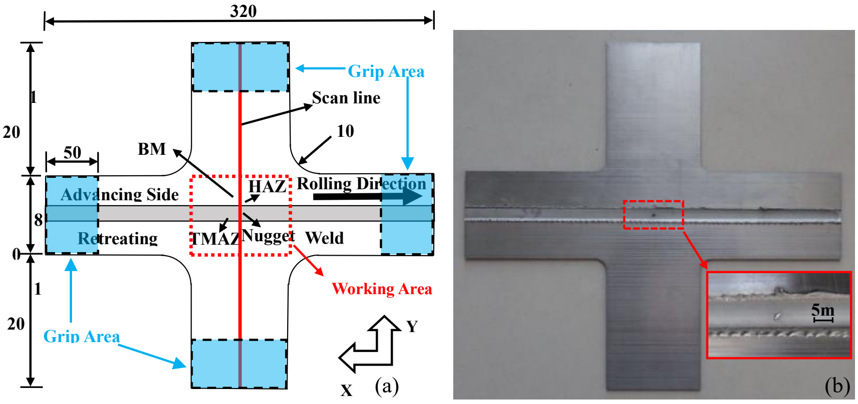

Figure 24: Cruciform sample (a) Sample size (unit: mm) (b) Welded sample

X-ray diffraction measurement

Xstress Robot, an advanced X-ray stress analyzer, was used to measure residual stress in longitudinal and transverse directions shown in Figure 25(a)-(c). The scan line is placed perpendicular to the weld in the centre of the sample shown in Figure 24(a)

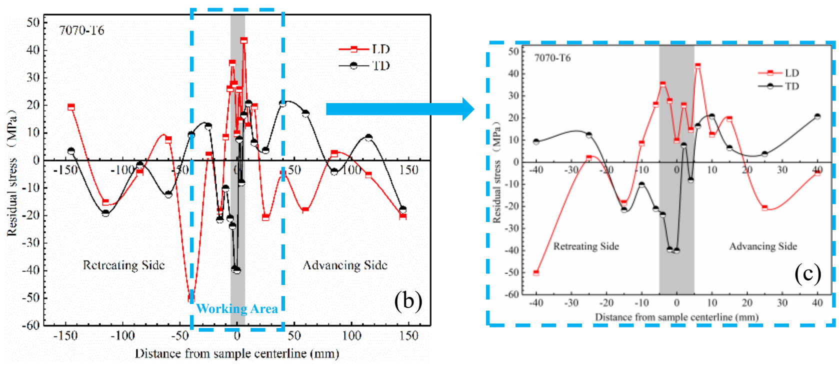

Figure 25: Measurement device and the profile of residual stress in FSW cruciform sample (a) Xstress Robot (b) Residual stresses profile of whole sheet (c) Residual stresses profile of working area (LD and TD mean longitudinal residual stress and transverse residual stress respectively)

---

[7] Northwestern Polytechnical University

Mixed-mode crack propagation model

ABAQUS was used to build the finite element model and to perform finite element analysis. The mesh detail of the finite element model is shown in Figure 26(a)-(c).

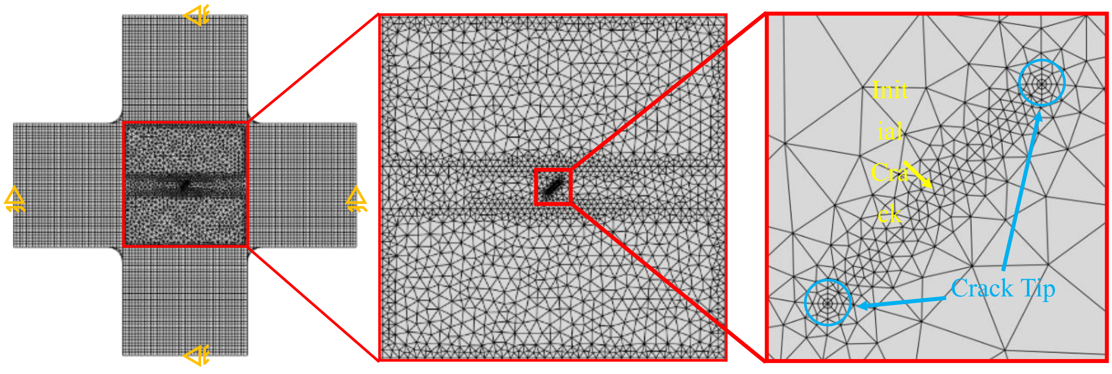

(a) (b) (c)

Figure 26: Finite element meshes used for the numerical simulation of cruciform sample mesh detail (a) in finite element model with boundary conditions (b) in working area (c) around the crack tip

Fatigue crack propagation path

The fatigue crack paths with and without residual stress for five biaxial loading ratios are shown in Figure 27(a)-(e). The crack tips close to the advancing side and the retreating side are defined as "Front 1" and "Front 2" respectively. The crack paths without residual stress (the solid line) agree with the experimental results (as the blue arrow shows), which derived from published literatures.

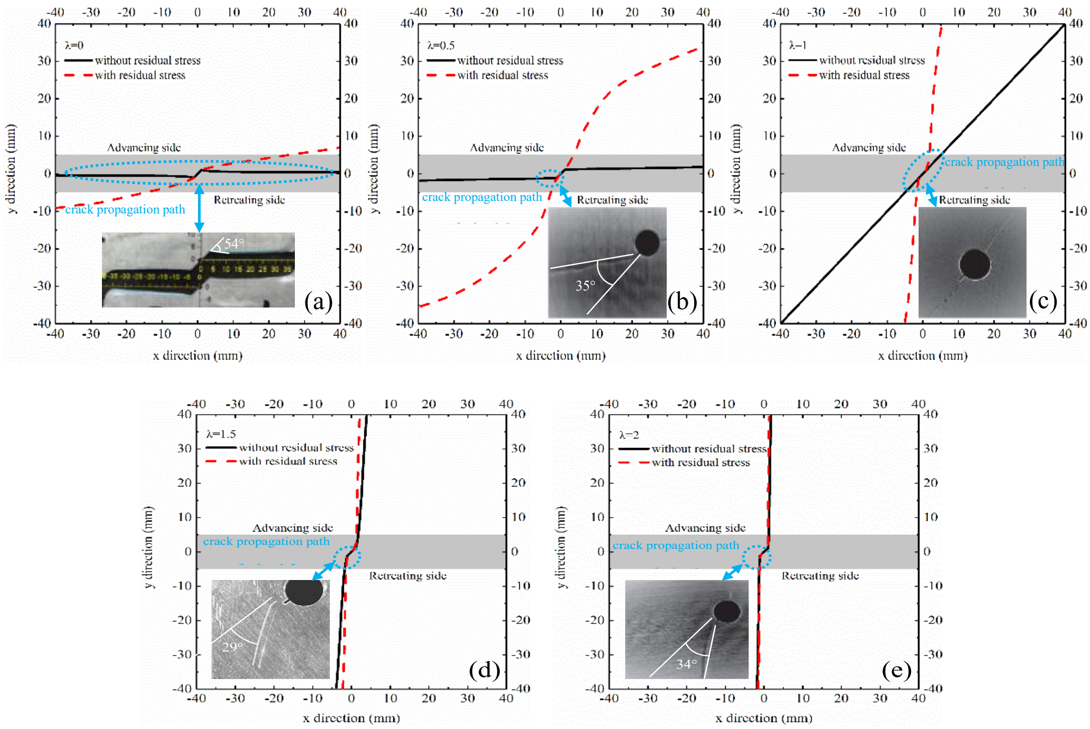

Figure 27: Crack propagation path in working area (a) λ = 0 (b) λ = 0.5 (c) λ = 1 (d) λ = 1.5 (e) λ = 2

2.4 Kernel Ridge Fatigue Life Prediction Approach for Laser-Directed Energy Deposition Ti-6Al-4V Alloy Based on Pore-Induced Failures [8]

Efficient machine learning two-step five features high cycle fatigue life prediction model of laser-directed energy deposition (LDED) Ti-6Al-4V alloy were developed. Fine granular area existence prediction model and subsequent fatigue life prediction model by using ridge classification and kernel ridge regression were employed respectively. Machine learning algorithm and correlation coefficient comparation were utilized to extract efficient input features from post-mortem analysis with the purpose of improving accuracy of final prediction models. Microstructure indicators and stress intensity features have great potential for fatigue life prediction. Pore type and existence label of fine granular area are microstructure indicators. Stress intensity factor range, aspect ratio of pore, the shortest pore distance to the free surface are stress intensity features. This article extends the knowledge of providing a method in order to realize beforehand fatigue life prediction of LDED Ti-6Al-4V alloy.

Post-mortem analysis

Figure 28 (a) to (c) illustrate typical fish-eye pattern in fracture surface of LDED Ti-6Al-4V alloy under 750, 800, and 850 MPa respectively. The fish-eye was marked in red dashed circle. In the yellow dashed circle and outside the center white circle, fine granular area (FGA) as well as rough area could be observed. Figure 28 (d) demonstrates typical fracture surface without FGA. Crack initiation (Stage I), crack propagation (Stage II), and the final fracture (Stage III) constitute fatigue life of this typical specimen. The crack initiation inducing pore was located at the center of the crack initiation region. In this article, pore type was also employed as a parameter for fatigue life prediction model of LDED Ti-6Al-4V alloy. Pore type was classified according to the relationship between pore size and microstructure characteristic because it would have impact on fatigue behavior as well as fatigue life of LDED Ti-6Al-4V alloy. Typical pore morphologies of pore types are illustrated in Figure 29.

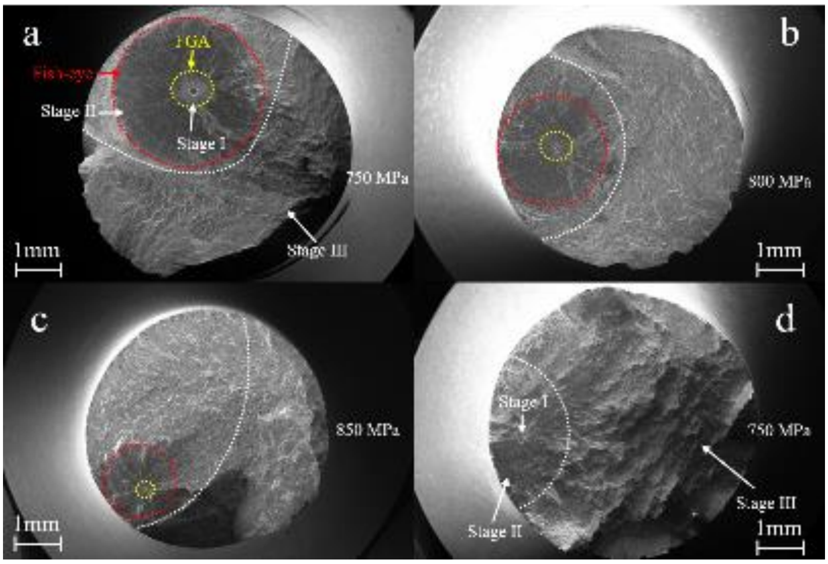

Figure 28: (a)~(c) Typical fracture surfaces of internal pore initiation specimens with FGA under 750, 800, 850 MPa, respectively; (d) typical fracture surface of an internal pore initiation specimen without FGA under 750 MPa.

[8] Beihang University

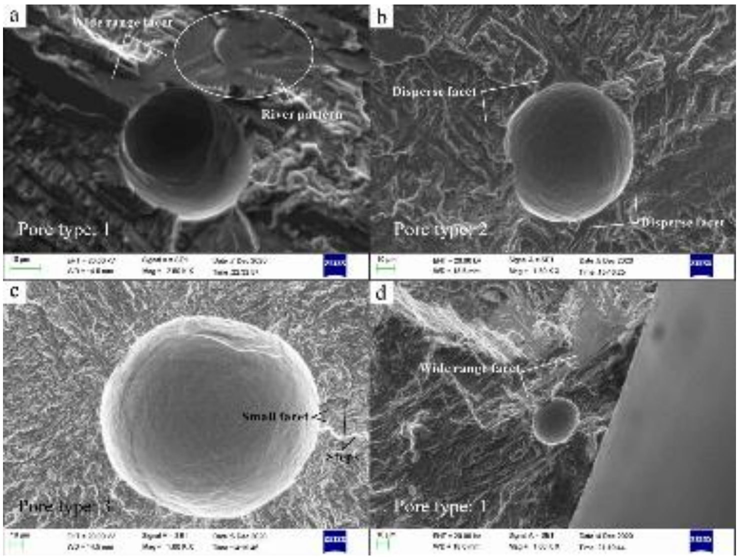

Figure 29: Typical pore morphology of (a) internal small pore (pore type I), (b) internal medium pore (pore type II), (c) internal large pore (pore type III), (d) subsurface small pore (pore type I).

Model development methods

Feature importance indicators model were employed before constructing fatigue life prediction models. And the fatigue life prediction models of LDED Ti-6Al-4V alloy were composed of 2 parts: (1) fish-eye existence prediction model and (2) final fatigue life prediction model. Diagram of model development method is demonstrated in Figure 30.

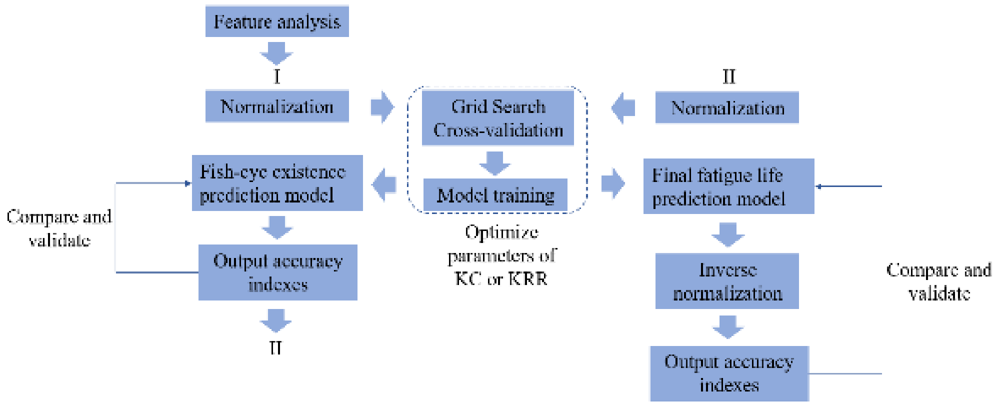

Figure 30: Diagram of model development method

Feature analysis

Feature analysis is a critical part for developing ML fatigue life prediction models. Refinement of appropriate input features might improve the accuracy and efficiency of ML models by a large margin. Mechanical factors used in traditional models could be considered as input features reference due to rationality and limited suitability. Feature analysis algorithms also could be employed to measure the importance of concerned features to some extent in mathematical field. AdaBoost algorithm and AdaBoost Regressor in Scikit-learn ML toolbox were used to calculate feature importance for fish-eye existence and fatigue life prediction, as is demonstrated in Figure 31. Figure 32 shows that all correlation coefficients of features with each other were less than 0.5 for both fish-eye existence and fatigue life prediction. Some correlation coefficients are even close to zero. These results reveal that selected features are low correlated with each other.

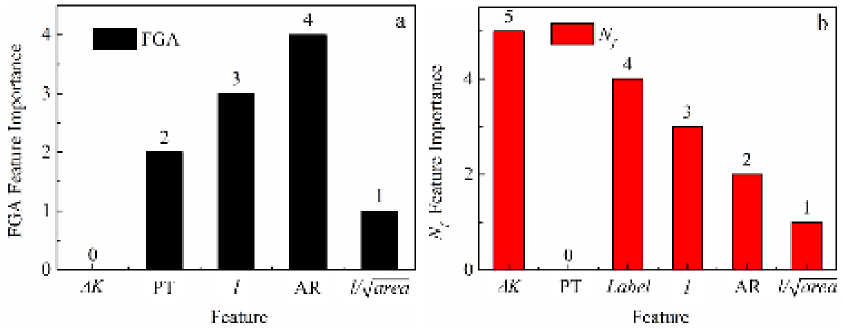

Figure 31: Feature importance for (a) fish-eye existence and (b) fatigue life prediction

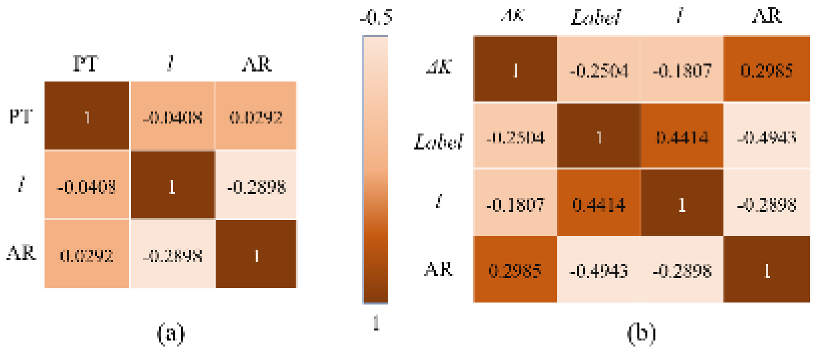

Figure 32: Feature correlation analysis: (a) fish-eye existence and (b) fatigue life prediction input features

Fatigue life prediction model

Kernel ridge regressor in Scikit-learn ML toolbox was employed to construct fatigue life prediction model. Input features were selected as ΔK, *Label*, l, and AR. Predicted fatigue life results fall into factor of two err bounds although only one point is located slightly outside the upper factor of two err bound as sketched in Figure 1.8. Considerable number of points are located very close the middle line. This indicates that the predicted results of test data are almost equal to experimental test data.

The input features are analyzed as: (1) l and AR are important features due to they affect the stress concentration nearby pores. (2) Only stress measurement might not enough to explain the mechanism fatigue behavior of LDED Ti-6Al-4V alloy with pore and other factor like ΔK might be necessary to consider. ΔK describe stress state and the localized stress field around pore. These could be seen as driving factor for fatigue crack initiation. It might be more comprehensive to evaluate stress state and predict fatigue life by ΔK and stress measurement factors. (3) Pore type have impact on the fatigue crack initiation mechanism. Therefore, it is an important factor when develop fatigue life prediction model. (4) Some researchers suggested that dislocation interaction or accumulation of irreversible plastic deformation around the crack tip is responsible for the formation of crack initiation at the early stage of crack initiation and propagation. Some researchers indicated that the grain refinement is owing to dislocation interactions in the vicinity of the crack source or at the crack tip resulted from locally high stress. This high strain localization leads to the excessive cyclic plastic deformation. In general, these processes are corresponding to the formation of FGA. Furthermore, it is well accepted that FGA consumes more than 90% of fatigue life and the formation of FGA plays a vital role in observing crack initiation and early propagation of LDED Ti-6Al-4V alloy in high cycle fatigue life region.

3 FATIGUE LIFE ENHANCEMENT METHODS AND REPAIR SOLUTIONS

3.1 Gas-pore Effects on Fatigue Lifetime of AM metals by Peridynamics[9]

The peridynamic approach consists of two main parts, i.e. computation of fatigue damage and modelling of gas-pore. Fatigue damage is considered as the gradual degradation of critical bond stretch in peridynamics, in which the exact degradation amount is obtained by fatigue lifetime data, as shown in Figure 33. Modelling of gas-pore is based on the bond decomposition strategy in peridynamics, in which the original bond is decomposed into many sublevel bonds for an elaborate description of interactions between two material points.

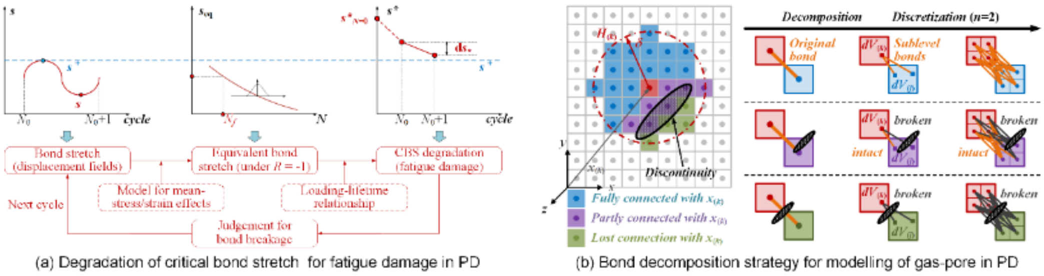

Figure 33: Peridynamic approach: (a) computation of fatigue damage; (b) modelling of gas-pore.

Crack initiation mode and fatigue lifetime

It reveals that the specimens display various crack initiation modes, as shown in Figure 34(a)~(d). For defect-free cases, fatigue cracks always initiate at the 'smooth' surface; for specimens with a surface pore, fatigue cracks always initiate at the surface pore; for specimens with an internal pore, however, fatigue cracks initiate either at the 'smooth' surface or at the internal pore.

The crack initiation mode has an obvious impact on fatigue lifetimes, as shown in Figure 34(e), in which the black dash denotes the fatigue lifetimes in defect-free cases. For specimens with an internal pore but crack initiations at the 'smooth' surface, in which gas-pores are commonly small and far from the specimen surface, fatigue lifetimes are comparable to those in defect-free cases. For specimens with an internal pore and crack initiations also at the internal pore, in which gas-pores are commonly lager and closer to the specimen surface, fatigue lifetimes show clear decrease if compared with those in defect-free cases.

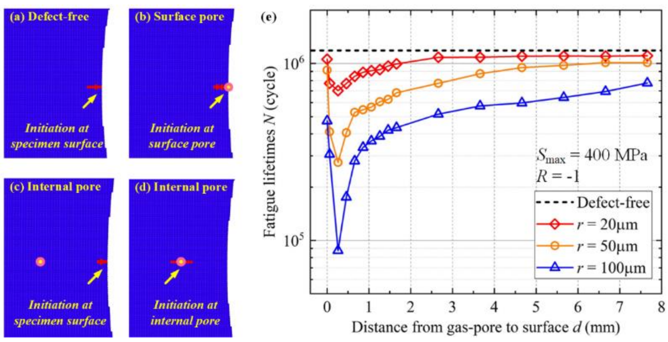

Figure 34: Effects of gas-pore locations and sizes on (a)~(d) crack initiation modes and (e) fatigue lifetimes.

[9] Beihang University

Gas-pore effects and fatigue failure process

It is easy to understand that larger gas-pore size leads to shorter fatigue lifetimes, but it is somewhat surprising in Figure 35 that effects of gas-pore locations are more obvious than effects of gas-pore sizes, and subsurface gas-pore is the most dangerous; in fact, such conclusions obtained by PD simulations are consistent with recent experiment observations by some research groups. The above gas-pore effects can be explained from the perspective of the process of fatigue failure, as shown in Figure 35, in which the outer side crack has to coalesces with specimen surface to form a longer single-edged crack before its propagation to fracture. Therefore, the shortest lifetimes for specimens with a subsurface gas-pore is resulted from the combined effects of easier crack initiation to coalescence as well as less cycles for small crack propagations after coalescence.

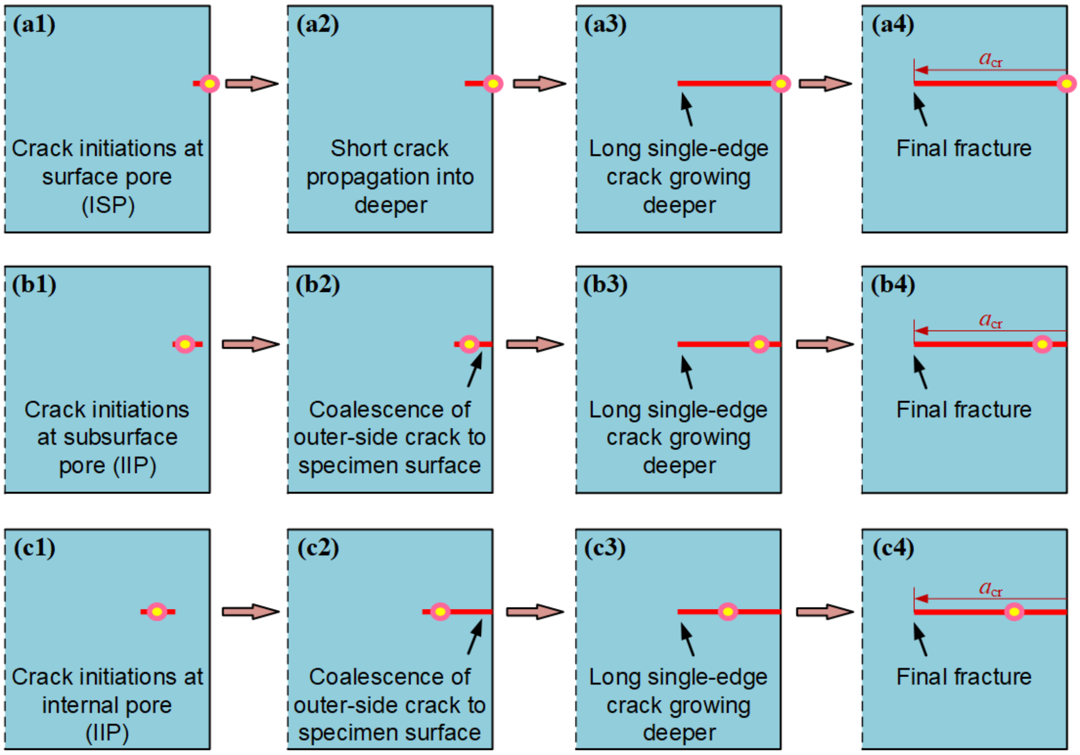

Figure 35: The process of fatigue failure for specimens with an internal pore.

From qualitative perspective, PD results accord with the predictions by approach based on Murakami parameter; however, PD simulations focus on crack behaviors during the whole process of fatigue failure, while the approach based on Murakami parameter aims at correlating fatigue lifetimes with cyclic loadings and pore characteristics. In certain sense, PD simulations possess the potential to support or supplement the approach based on Murakami parameter.

More can also be concluded from this PD study for fatigue evaluations on AM metals. Due to the features of AM processing and materials, it is impractical to characterize material fatigue properties by fatigue lifetimes obtained by smooth specimens, and it is also questionable whether specimen data obtained in laboratory can be reliably applied to evaluations on parts in service. Rather than by phenomenological correlations in the present methodology, fatigue evaluation methods for AM parts should be developed by emphasizing the whole process of fatigue failure.

3.2 Study on the Influence of the Shot Peening Forming and Reinforcement Technology on the Fatigue Performance of Panel Structure[10]

The shot peening forming technology is a kind of curved plate forming method in recent years. The surface of the Panel formed certain compressive stress zone during the shot peening forming process, which is beneficial to the fatigue performance of the Panel, but at the same time, because of the larger projectile used in the shot peening forming, a large crater was formed on the surface of the panel, and the surface defect was introduced, which is unfavorable to the fatigue performance of the Panel . Therefore, the comprehensive effects of different shot peening process parameters on the fatigue properties of the panel are different. In order to eliminate the adverse effect caused by shot peening, the shot peening strengthening method is usually used to strengthen the wall structure and enhance its fatigue performance. It is necessary to study the fatigue properties of the Panel structure after shot peening and strengthening under different process parameters.

In this work, the structural fatigue and damage tolerance properties of the aircraft Panel were compared with those of the original material after the special shot peening and strengthening process parameters were processed and the related tests were designed. The changes of DFR_{base}, $DFR_{cut\text{-}off}$, crack propagation rate and fracture toughness of the structure after shot peening and strengthening were studied respectively.

The test and analysis show that the fatigue performance of shot peening forming and strengthening process is equivalent to the original plate under the maximum shot peening rate and strength parameters. By considering the bending effect of the test piece itself, the structural fatigue performance of shot peening and strengthening process is higher than that of the original plate after the modification. After the shot peening and strengthening process, the crack growth rate and fracture toughness of the structure have not changed greatly.

Study on the influence of DFR_{base} value and $DFR_{cut\text{-}off}$ value

The test results are shown in Table 3. The results show that the fatigue performance of the wall plate after shot peening and strengthening is similar to that of the base material and slightly improved.

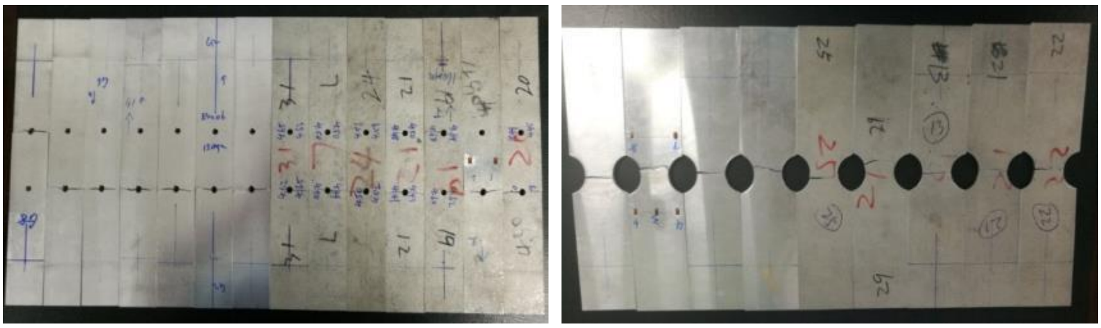

(a) DFR_{base} Value test (b) $DFR_{cut\text{-}off}$ Value test

Figure 36: DFR Base Value and closing value test

[10] AVIC The First Aircraft Institute

Table 3: Comparison of Fatigue Properties of the Panel Structures before and after the shot peening forming and Reinforcement Process

Category	Material	State of process	Test result /MP*a*	DFR Percentage increase
DFR_{base}	2024-T351	Original plate	134.94	+1.38%
		The shot peening	136.80	
	7B50-T7751	The shot peening（1.2mm）	117.48	+0.91%
		The shot peening（1.4mm）	118.54	
$DFR_{cut\text{-}off}$	2024-T351	Original plate	181.90	+13.59%
		The shot peening	206.61	
	7B50-T7751	The shot peening（1.2mm）	188.43	+6.24%
		The shot peening（1.4mm）	200.19	

Study on the influence of fracture toughness

Compact tensile (CT) specimens were used in the test. The results show that the fracture toughness of the wall plate after shot peening and strengthening is slightly lower than that of the original structure, which is basically the same.

Table 4: Comparison of fracture toughness of the panel shot peening forming and strengthening process

Size	The value of K_{IC}（or K_Q）					
	2024-T351	2024-T351 shot peening	Results comparison	7B50-T7751	7B50-T7751 shot peening	Results comparison
60×20×21	34.77	34.54	-0.6%	20.08	19.12	-5.02%
100×10×35	46.36	45.87	-1.06%	21.99	22.91	4.01%

Study on the Influence of Crack Propagation Rate

The results show that the shot peening and strengthening process have very limit effect on the crack growth rate of the panel structure.

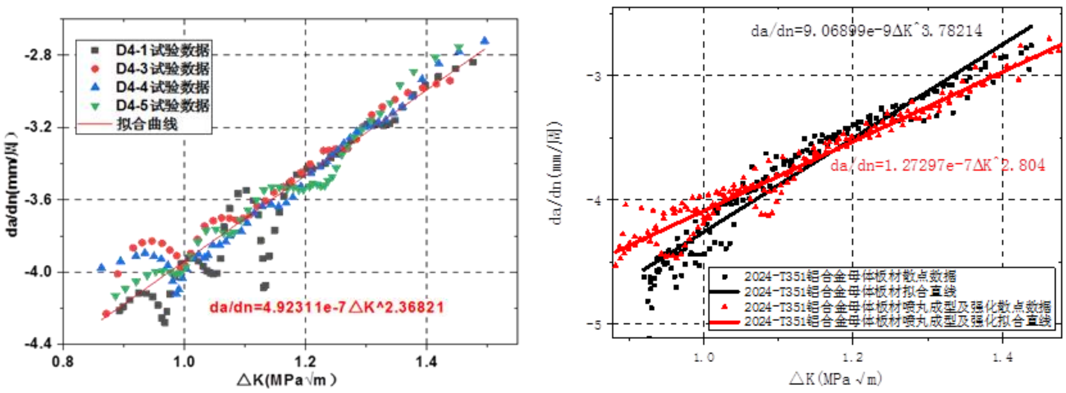

(a) Test results of crack propagation rate of 7B50 (b) A comparative curve of crack propagation rate of 2024

Figure 37: Test results of crack propagation rate

3.3 Analysis and Optimization of Damage Tolerance of Large Aperture Cold-Expanded Bushing Lug[11]

The main conclusions of this study are as follows: The damage tolerance of large aperture cold-expanded bushing lugs can be evaluated reliably by using the damage tolerance analysis method considering residual stress; by optimizing the interference amount of the bushing, the residual compressive stress at the hole edge can be effectively increased, the crack propagation can be suppressed, and the damage tolerance of the lug can be improved.

Simulation analysis of residual stress

The circumferential stress of the cold-expanded bushing during the simulation is shown in the figure.

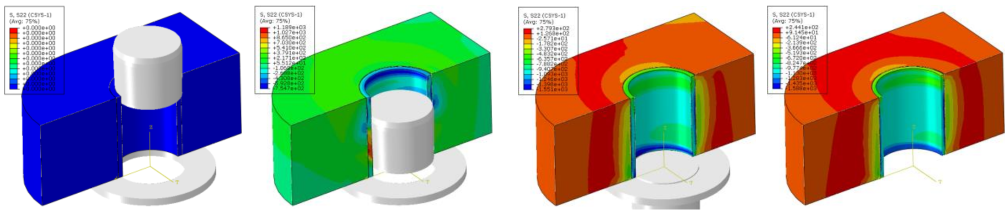

① Initial state ②Mandrel drawing process ③Mandrel drawing completed ④After cutting the inner wall of the bushing

Figure 38: Circumferential stress during simulation of cold-expanded bushing reinforcement (cross-sectional view of symmetrical plane)

Damage tolerance analysis

According to the theory of elastic fracture mechanics, the superposition method can be used to calculate the stress intensity factor. It can be obtained that $K_A = K_B + K_C$ as shown in Figure 39, where P is the load and σ is the stress distribution at the crack surface of intact structure. The stress intensity factor of intact structure $K_A = 0$. Therefore $K_B = -K_C$.

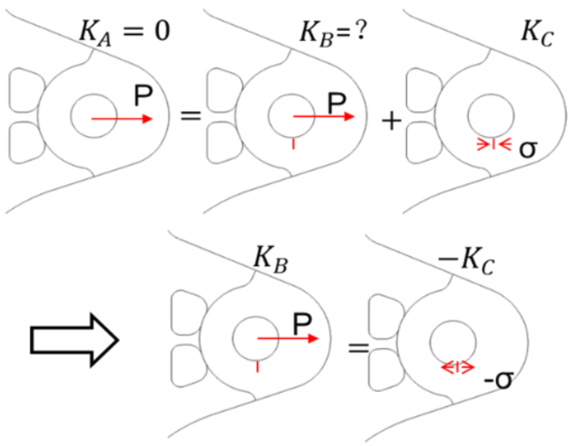

Figure 39: Linear superposition theory

The stress distribution on the crack surface was introduced to analyze the crack propagation, and the crack leading-edge stress intensity factor and the crack propagation life were obtained. The Crack propagation analysis result is shown in Figure 40.

[11] AVIC Chengdu Aircraft Design & Research Institute

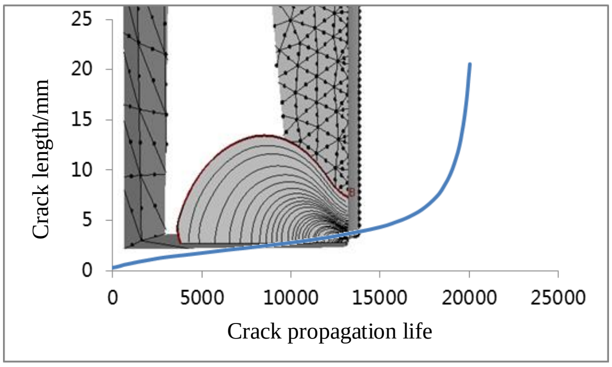

Figure 40: Crack propagation analysis result

In order to verify the reliability of damage tolerance analysis, the analysis results were compared with the non-destructive testing results of fatigue specimen. Figure 41 shows the comparison between the analysis result and the test result, the analysis result is basically consistent with the test result, and the damage tolerance analysis method is accurate and reliable.

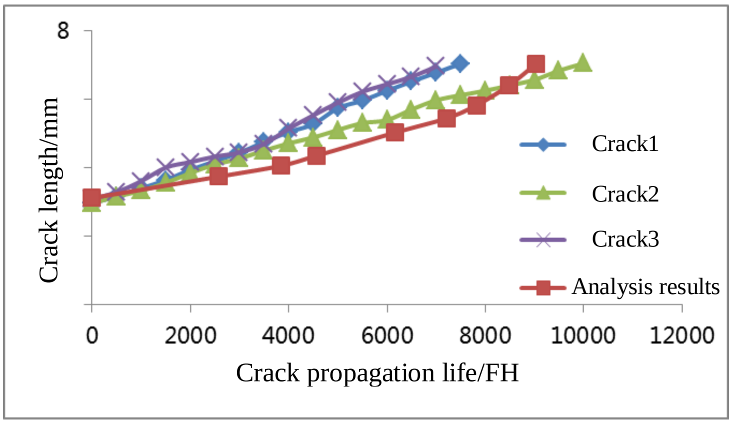

Figure 41: Comparison of analysis and test results

Optimal design of damage tolerance

After increasing the interference amount of the cold-expanded bushing, through the simulation analysis, the residual compressive stress at the hole edge increases obviously and the crack propagation is suppressed effectively.

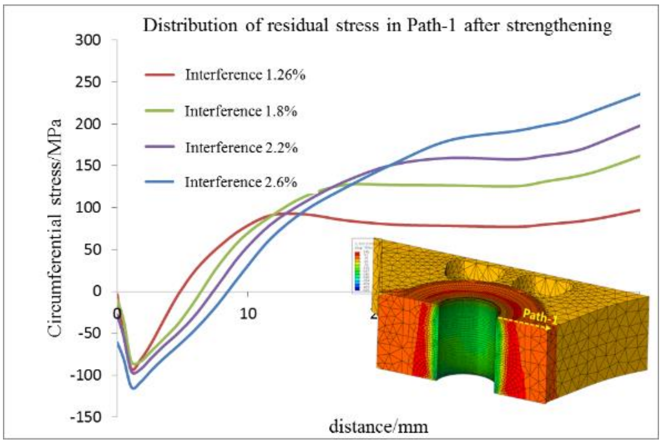

Figure 42: Comparison of residual stress at hole edge under different interference amounts

The results in Figure 43 show that the greater the interference, the greater the residual compressive stress along the hole edge, the better the suppression effect of crack propagation. However, the larger the interference amount, the greater the pulling force of the mandrel, which will increase the risk of the mandrel stuck during the bushing installation. In order to prevent sticking of mandrel, pulling force shall not be greater than 50% maximum pulling force of pulling gun. The drawing force of mandrel with different interference is analyzed. It can be seen that the drawing force of mandrel increases with the increase of interference. Therefore, if 2.2% interference is selected, good damage tolerance can be achieved under the premise of effectively controlling the risk of jamming of mandrel.

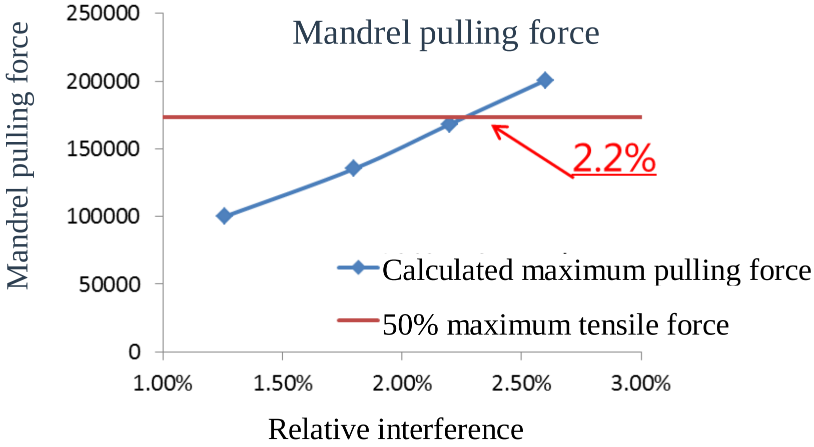

Figure 43: Pullout force of mandrel with different interference amount

The fatigue test of 2.2% interference amount of the lug was carried out. After the crack propagated to 3 mm, the test was continued for 16000FH, and the crack did not propagate, indicating that the crack propagation could be effectively suppressed by increasing the residual compressive stress at the hole edge.

4 STRUCTURAL HEALTH / LOADS MONITORING

4.1 Intelligent Fleet Life Management Based on Structural Health Condition[12]

While pursuing high mobility and high stealth, the aircraft structure platform is required to have the characteristics of high load capacity, light weight, long life and low maintenance cost. In order to achieve the above targets, in addition to using the advanced fatigue design method to carry out structural fatigue design in the design stage, and during the service stage monitoring the key parts and develop SPHM system based on monitoring data to achieved precise management of fleet life. High efficiency, accurate evaluation for the health state of key parts, and life management based on multiple constraints are the two key technologies to realize precise management of fleet life.

Key technologies

Through the establishment of coverage design, manufacture and service of life cycle data management method, the key parts life evaluation model of aircraft structure driven by reduced-order model is built by the data of each stage and accurate evaluation of the health status of individual machines in the cluster and the conclusion of life consumption. At the same time, using the large data analysis and artificial

[12] AVIC Shenyang Aircraft Design & Research Institute

intelligence technology, the conclusions of structural health assessment, structural maintenance data, training intensity, annual training plan and other constraints such as maintenance economy, fleet retention rate, etc. Establishing fleet life management model to achieve precise management of fleet life.

Subject of Study

The object of the study is the docking zone between the wing and the fuselage of the fighter, which is the fatigue key part, and the structure is shown in the figure below.

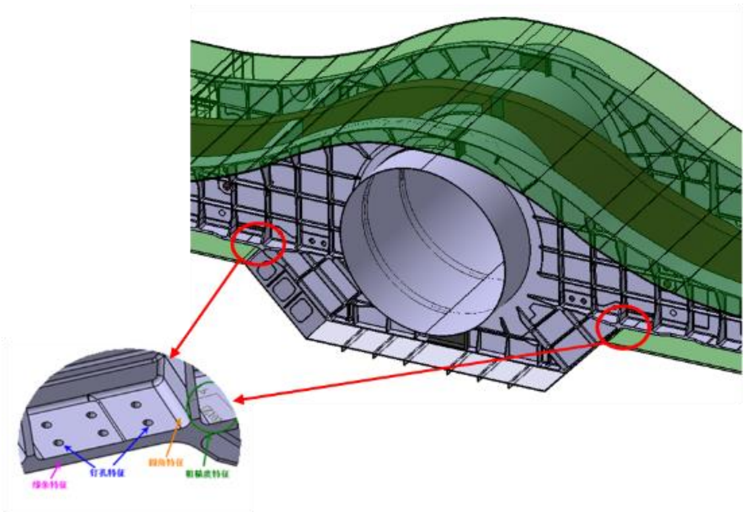

Figure 44: Test piece for docking zone between wing and fuselage

In the crack initiation stage, the fatigue life is calculated by the nominal stress method. In the crack growth stage, the key structural parameters are extracted based on the model of the crack propagation stage, and geometric size, initial crack length, material data and load spectrum data are used as the input, residual strength and crack growth are used as the output, and the Walker formula is used to calculate the key structural parameters. As the test is carried out, the test data is accumulated，using the test and simulation data to the establish the reduced order model. Based on the reduced order model, we can predict the damage condition of the structure and access structural health state efficiently.

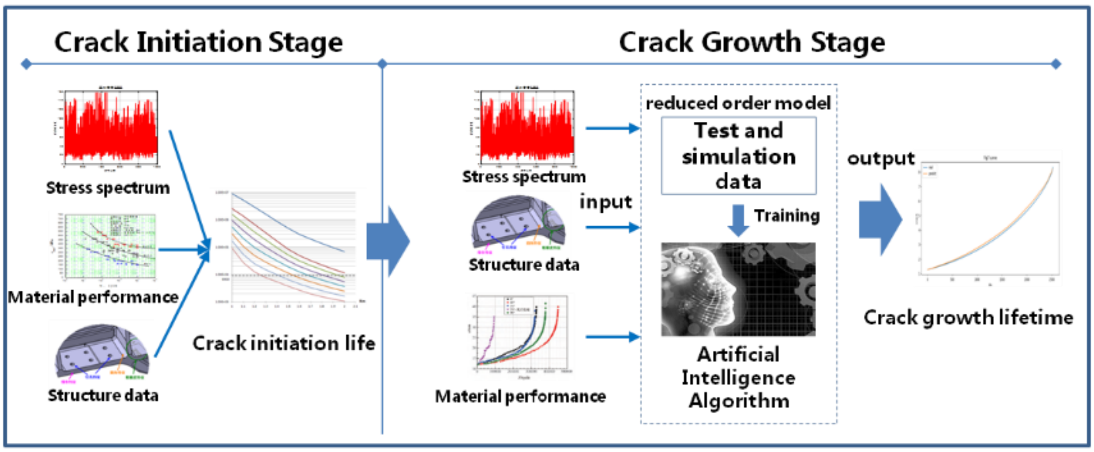

Figure 45: Health state assessment based on reduced order model

Aircraft fleet life management based on the healthy state of aircraft structure can improve the combat capacity and maintenance economy of aircraft fleet by comprehensive analysis of structural health status, maintenance data, training intensity of flight training subjects and flight data of pilots, introducing constraints like annual training plan, maintenance economy and fleet retention rate, and using AI Technology to solve optimization by multiple constraints.

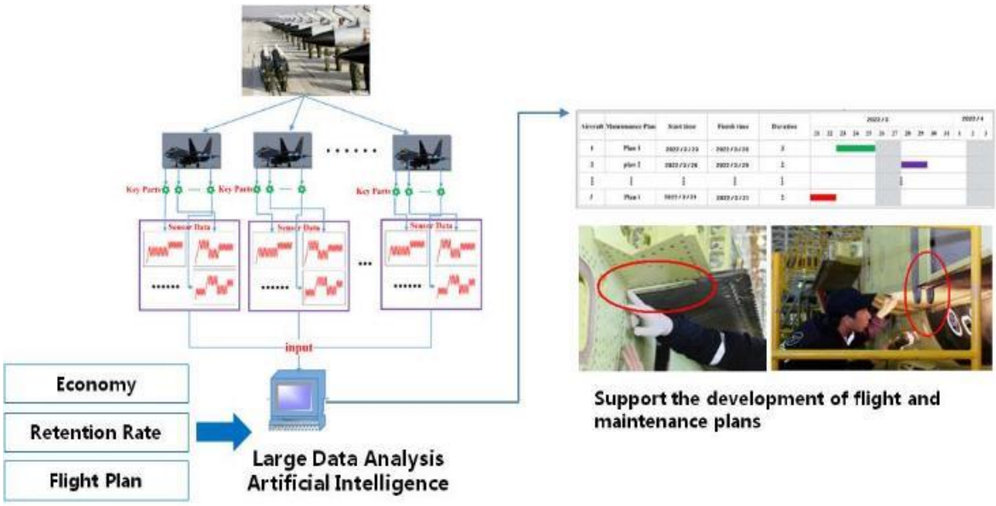

Figure 46: Intelligent Fleet Life Management Based on Structural Health State

4.2 Euclidean Space Method for Distributed Load Recovery from Strain Measurements[13]

In order to solve the selection of basis load cases, a stepwise method based on Schmidt's orthogonalization of the maximum vertical distance to select the basis vectors from Euclidean space is proposed, which is called Euclidean space method. The general idea is to select the vector with the largest vertical distance from the current Euclidean space in turn to form a new Euclidean space until all vectors are in that Euclidean space and the selected vectors are the basis cases. The process is shown in Figure 47.

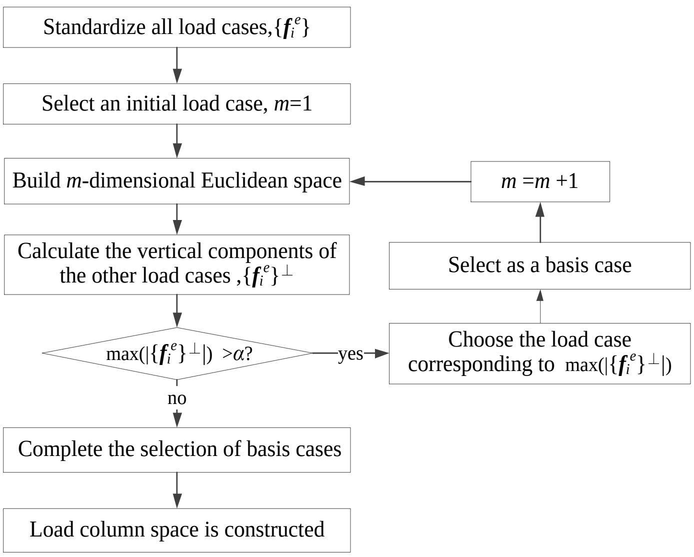

Figure 47: The flowchart of selecting basis load cases based on Euclidean space method

---

13 AVIC Chengdu Aircraft Design & Research Institute

The process of distributed load inverse approach based on Euclidean space method is shown in Figure 48. The key point is to first select load basis cases from the load space, and then further select strain basis cases from the strain space under the premise that the strain basis cases include the load basis cases. The candidate strain set in Figure 48 refers to the set of strain measurement points that can be arranged in the structure.

Furthermore, Tikhonov's regularization method is used to reduce ill-conditioning of the inverse matrix.

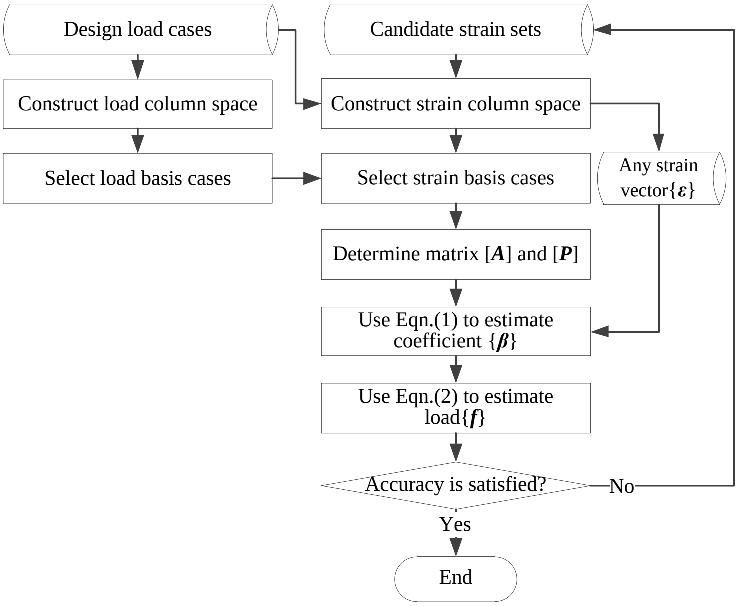

Figure 48: The process of distributed load inverse approach based on Euclidean space method

Case study

Load rams and fiber-optic sensor data of a certain aircraft wing fatigue test are used as a case study to verify the Euclidean Space method proposed in this paper. There are 749 unique load cases in the fatigue test spectra, i.e. M=749. There are 24 load rams that have applied loads through whiffletrees to the lower wing surfaces, i.e. n=24. There are 116 effective strain measurements from optical fiber sensors along the beam, which are used as the candidate strain set in this example (g=116).

First, 23 load basis cases are stepwise selected from the load column space, shown as Figure 49, and then 82 strain basis cases are stepwise selected from the strain basis cases, and the influence coefficient matrix [$A_{116,82}$] and the basis load matrix [$P_{24,82}$] are determined.

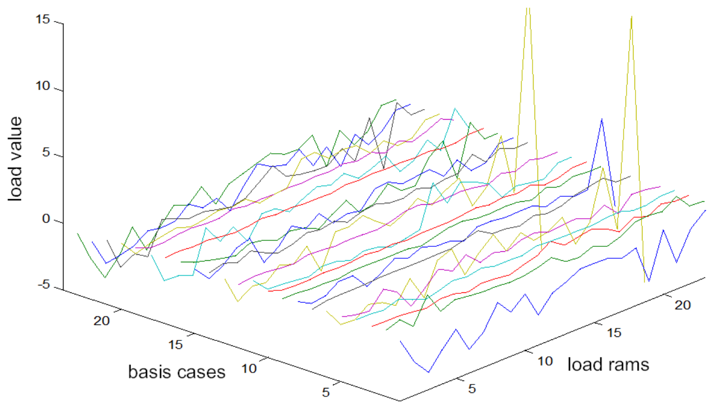

Figure 49: Distributed loads at 23 load basis cases

If the distributed loads of 749 test cases is unknown, only the strain distribution $\{\varepsilon_i\}$ at each case is known, Tikhonov regularization method are used to predict the load rams of 749 load cases based on $[\boldsymbol{A}_{116,82}]$ and $[\boldsymbol{P}_{24,82}]$. The overall loads of sub-components (wing root shear/bending moment/torque, control surface shear/hinge moment) are further calculated according to position of the actuators, and the predicted load values are compared with the actual values to verify the prediction accuracy and robustness of Euclidean Space method, shown as Figure 1.2-4.

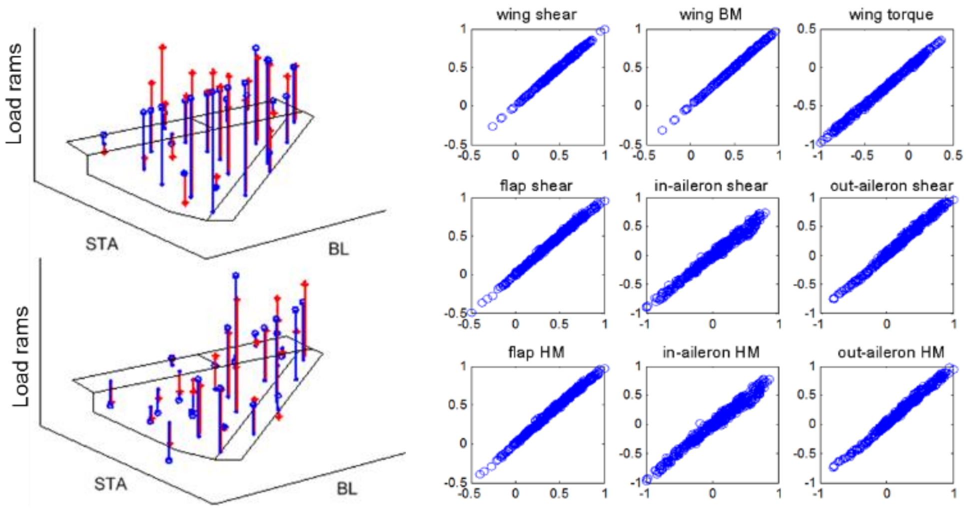

a) Load distribution (b) sub-component Load

Figure 50: Load prediction comparisons

4.3 Research on the Method of Aircraft Load Prediction and Strain Prediction of Key Structures Based on Machine Learning[14]

In this study, neural network and support vector machine (SVM) are used to establish the load prediction model of the tail wing root (Figure 51) of the large-scale conveyor and the strain prediction model of key structures of aircraft. The neural network model is shown in Figure 52. The prediction results of shear based on neural network are compared and analyzed with those of traditional multivariate linear regression model, as shown in Figure 53(a). The black line is the true value of shear, the red line is the prediction result of neural network, and the blue line is the prediction result of multivariate linear regression. Figure 53(b) is a comparison of relative errors. It can be seen that the prediction accuracy of neural network model is better than that of multivariate linear regression model.

The SVM model is shown in Figure 4. The prediction results of key structures strain based on SVM are compared and analyzed with those of traditional multivariate linear regression model, as shown in Figure 55 (a). The black line is the true value of strain, the red line is the prediction result of SVM, and the blue line is the prediction result of multivariate linear regression. Figure 55 (b) is a comparison of relative errors. It can be seen that the prediction accuracy of SVM model is better than that of multivariate linear regression model.

[14] AVIC The First Aircraft Institute

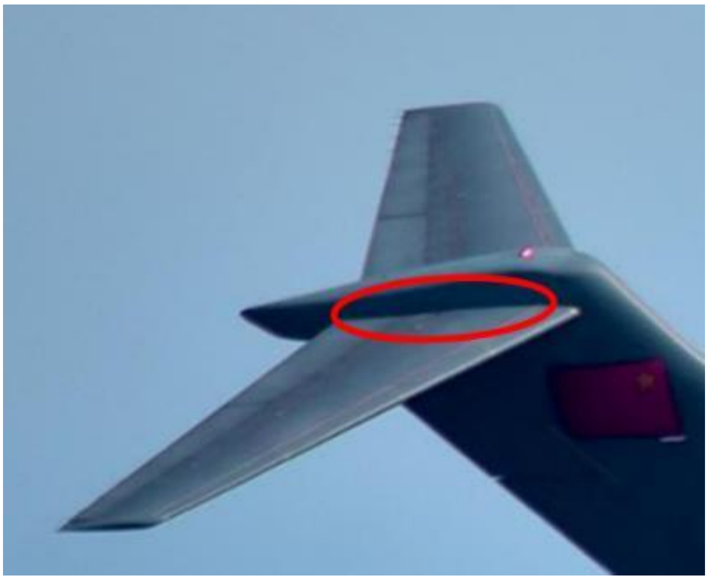

Figure 51: The tail wing root of the large-scale conveyor

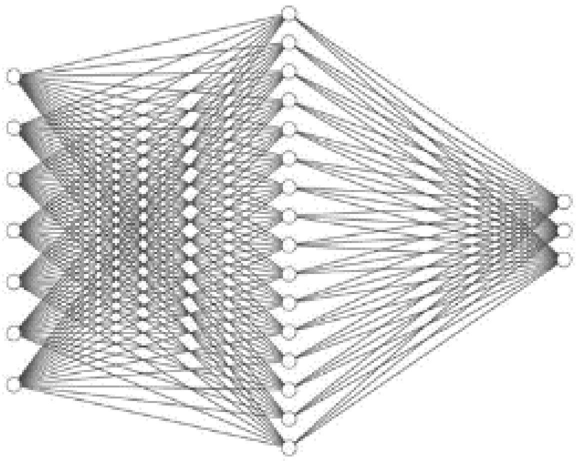

Figure 52: Neural network model

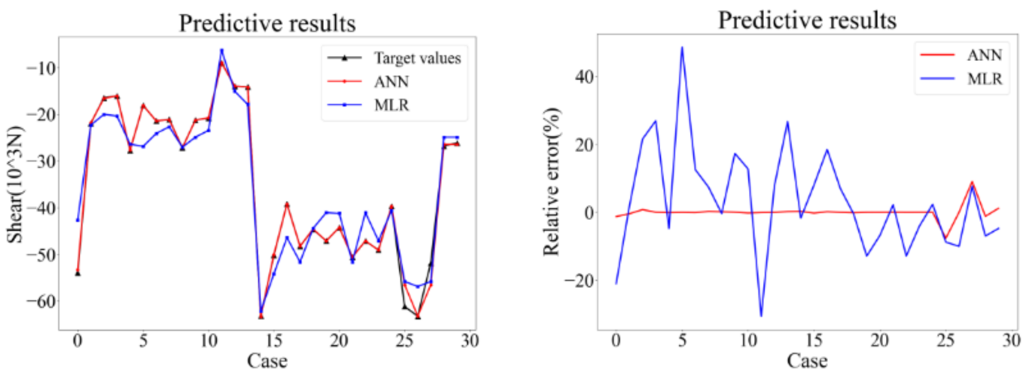

a）Comparison of prediction results b）Comparison of relative errors

Figure 53: Load prediction results of neural network and multivariate linear regression model

（Red line: Neural network；Blue line：Multivariate linear regression）

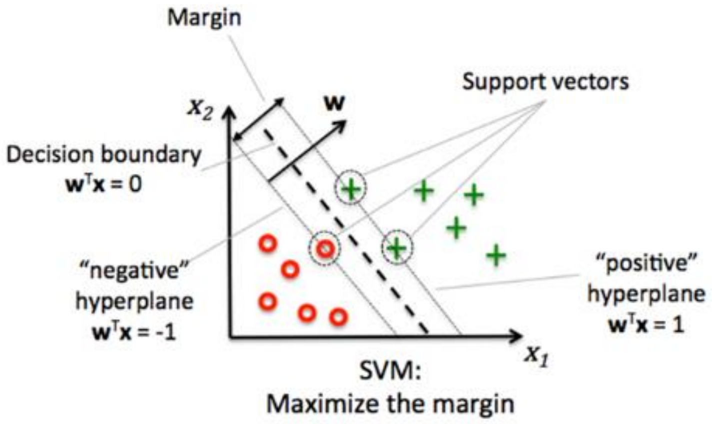

Figure 54: Support vector machine model

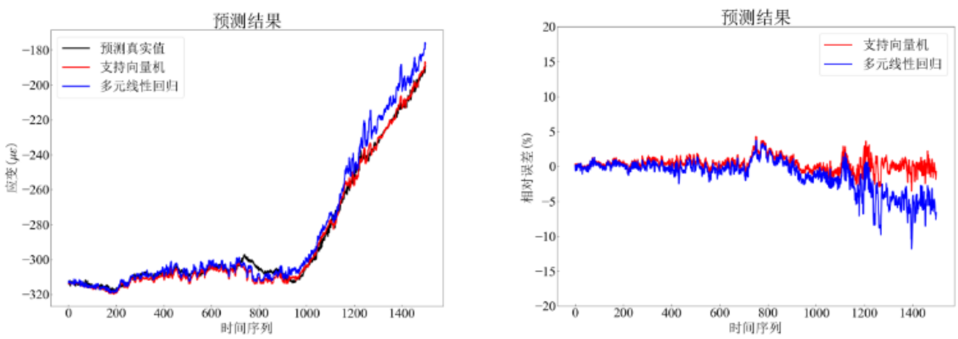

a）Comparison of prediction results

b）Comparison of relative errors

Figure 55: Strain prediction results of key structures of support vector machine

4.4 Application of Structural Health Monitoring Technology for Full-Scale Fatigue Test[15]

Full scale aircraft structural fatigue test is an important means to expose the weak parts of civil aircraft structural design, formulate reasonable inspection and maintenance intervals, and determine the structural life of civil aircraft. Meanwhile, found the structural damage in the test timely and accurately plays a vital role in the safety of the test and the final test report. Structural health monitoring technology has become one of the hotspots in the field of full-scale aircraft structural fatigue test due to its characteristics of automatic real-time monitoring, sensitive to micro-cracks, and less affected by human factors. However, the full-scale aircraft structural fatigue test is characterized by complex loading scheme, complex test environment and long test period, which pose challenges to test monitoring technology and test follow-up personnel. In response to these challenges, the Aircraft Strength Research Institute of China (ASRI) has developed a set of integrated structural health monitoring system, which includes multiple monitoring subsystems (acoustic emission, guided wave, intelligent coating, strain, machine vision, etc.), and has been successfully applied in the C919 full scale aircraft structural fatigue test. The integrated system also has the function of remote data integration control, which can realize the synchronization of test load and one-way data transmission between Shanghai and Xi'an. To support Xi'an Control Center to carry out real-time data acquisition, data synchronization, data analysis, data

15 AVIC Aircraft Strength Research Institute

storage, comprehensive diagnosis, damage warning and other work for the C919 full scale aircraft structural fatigue test in Shanghai test plant, to achieve the purpose of real-time monitoring of the test. At present, the system has successfully found abnormal damage such as air leakage in the C919 full scale aircraft structural fatigue test, effectively assisting the C919 full scale aircraft structural fatigue test.

Guided-wave-based damage detection

Guided wave structure health monitoring is an effective means of health monitoring. In full aircraft fatigue test, conducting guided wave structure health monitoring in the area of concern is helpful to timely understand the aircraft structure status and carry out necessary early warning for damage.

In the full aircraft fatigue test, the guided wave monitoring system developed the following key technologies: automatic triggering technology under selected load conditions, third-party software control and acquisition technology, and damage index early warning database technology based on normal distribution. These key technologies can be applied to guided wave health monitoring in many engineering structures.

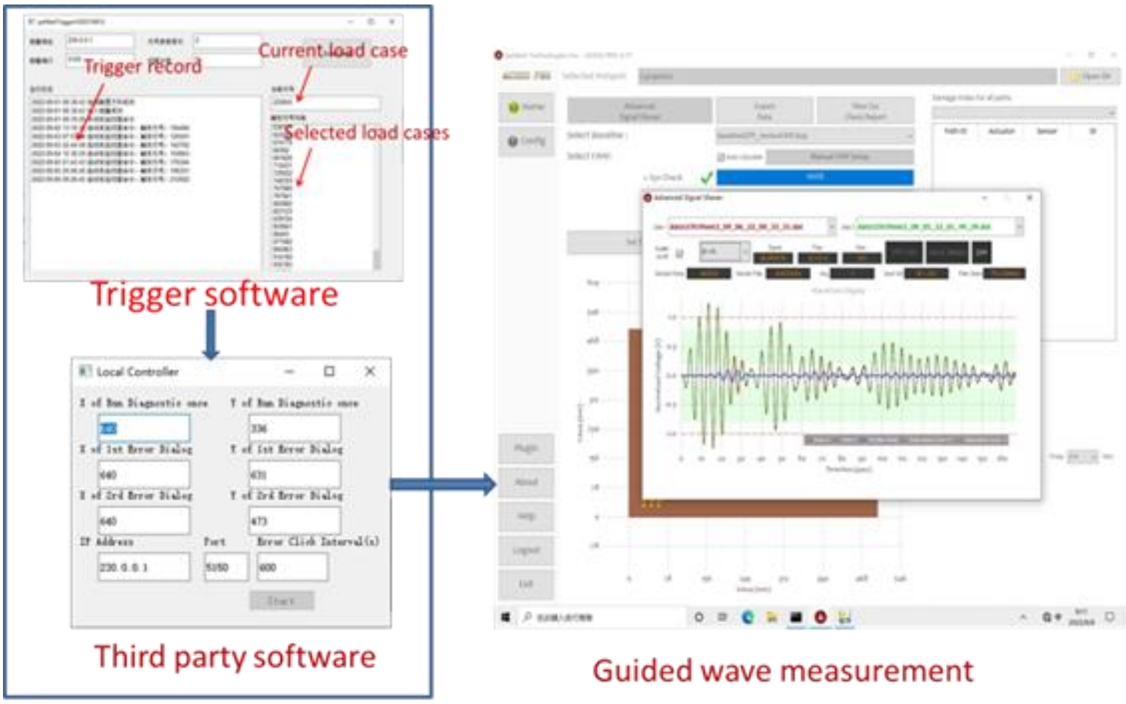

Figure 56: Automatic guided wave acquisition under selected load

Acoustic emission monitoring system

Faced with complex aircraft structure, complex test load spectrum, complex test environment, high background noise, and the need for real-time processing of massive data, the acoustic emission monitoring system, based on load synchronization, data cleaning, data segmentation, rapid data extraction and other technologies, has established an early warning model for damage to key parts of the aircraft, and has conducted real-time processing, analysis and storage of remote and massive acoustic emission data. It effectively solves the problems of low monitoring efficiency, great difficulty in damage identification and unreliable identification in acoustic emission damage monitoring of whole aircraft fatigue test. The discovery of air leakage points in full-scale aircraft fatigue test further verified the effectiveness of the system, show in Figure 57.

Figure 57: Air leakage point

Machine vision inspection system

A machine vision damage detection system based on computer vision and robot structure design is developed for the purpose of automatic damage detection in the fatigue test of aviation structures. The key technologies of machine vision damage detection system contain: robot structure design for limited space including global imaging, object recognition and path planning, which can autonomously identify the parts to be detected in the full-size structure and realize automatic scanning, then complete clear imaging of key structural details on the basis of ensuring the structure safety; the damage recognition based on neural network, which is able to ignore the interference of surface texture, scratch, stain and other factors, and achieve rapid and accurate detection of millimeter damage.

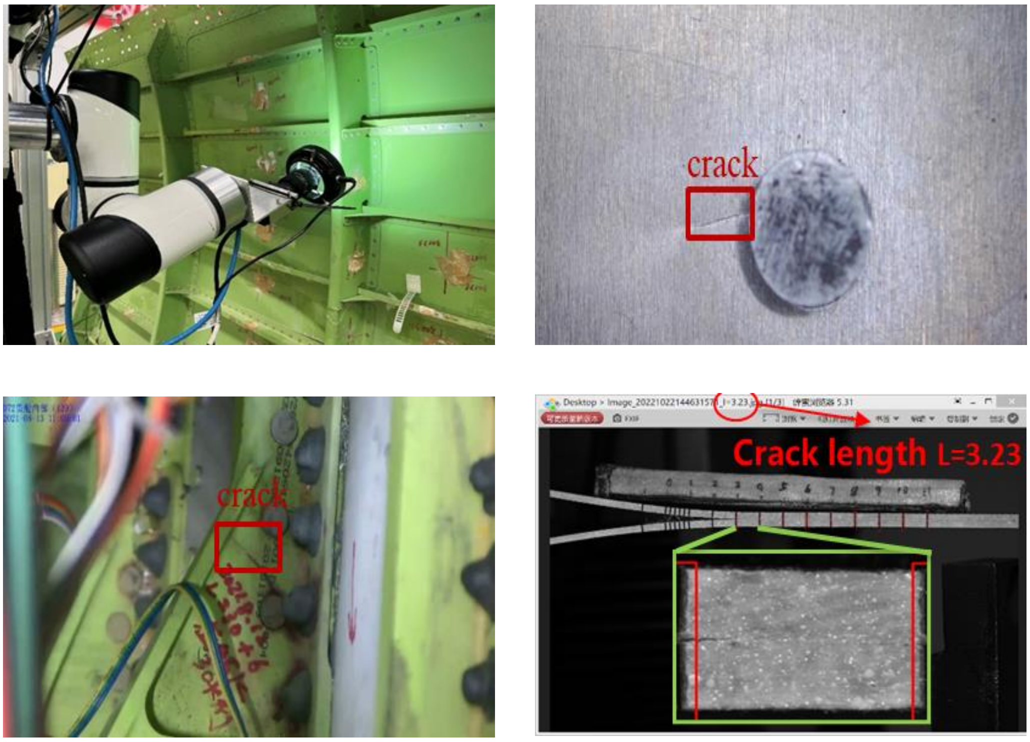

Figure 58: Machine vision damage detection system

5 NDI, INSPECTIONS AND MAINTENANCE

5.1 Multi-frequency Ultrasonic Testing Method for Three-Dimensional Woven Composites[16]

Three-dimensional woven composite material is a new type of composite material that uses fiber braid woven by weaving technology as reinforcement, and the resin is injected into the preformed part by the RTM process and finally cured. Different from the traditional composite laminate structure, the spatial interlocking network structure of three-dimensional woven composite materials fundamentally avoids the generation of delamination damage and significantly enhances the impact resistance. While maintaining the integrity of the bearing deformation of components, three-dimensional woven composite materials also have the advantages of high specific strength, large specific modulus, and easy to form complex structures at one time, and are widely used in aviation and the field.

Research on methods for ultrasonic detection of three-dimensional woven composites

As the most used nondestructive testing method for the detection of resin matrix composites, ultrasonic testing has a good detection effect and obvious defect characteristic signals for defect types such as delamination, debonding, and porosity. Compared with three-dimensional woven composite materials and laminates, there is no delamination, debonding defects, and whether it is inter-bundle pores or dry spots in the bundle, can be regarded as the unwetted area of the resin inside the structural parts, due to the difference in acoustic impedance between the unwetted area and the completely wetted area, so there is ultrasonic reflection and projection transmission at the interface of the two areas, Figure 59 is the C-scan results of the 5M ultrasonic line array probe commonly used to detect composite materials, the C-scan results can be seen, The unwetted areas of the resin have different depths, different geometries, and are irregularly distributed. In this experiment, multiple frequencies of ultrasonic waves were selected to detect the internal defects of three-dimensional woven composites.

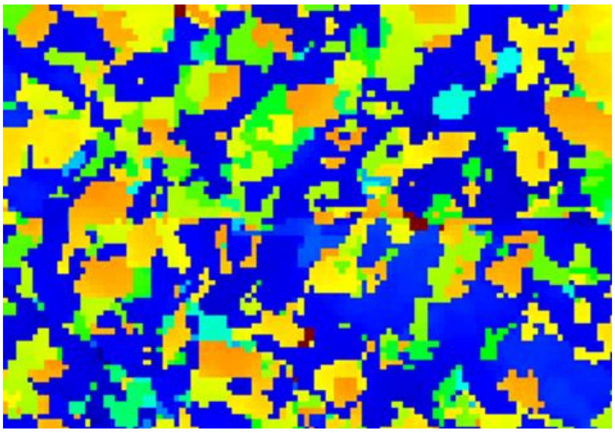

Figure 59: C-scan results of a three-dimensional woven composite

A three-dimensional woven composite blade was intercepted from a rotor as a research sample, the sample was a structural part with variable thickness and variable curvature, the thickness range was between 4mm~12mm, and the shape and size information of the blade were shown in Figure 60.

[16] AVIC Aircraft Strength Research Institute

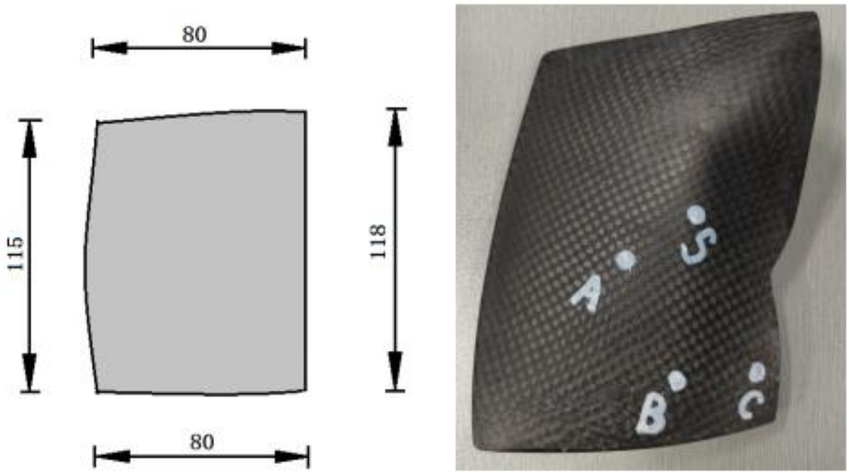

Figure 60: Specimen shape and point location diagram

The ultrasonic reflectance method is used to compare the reflected signals of 1 reference point and 3 reference points, and the ultrasonic reflection signals are shown in Figure 61.

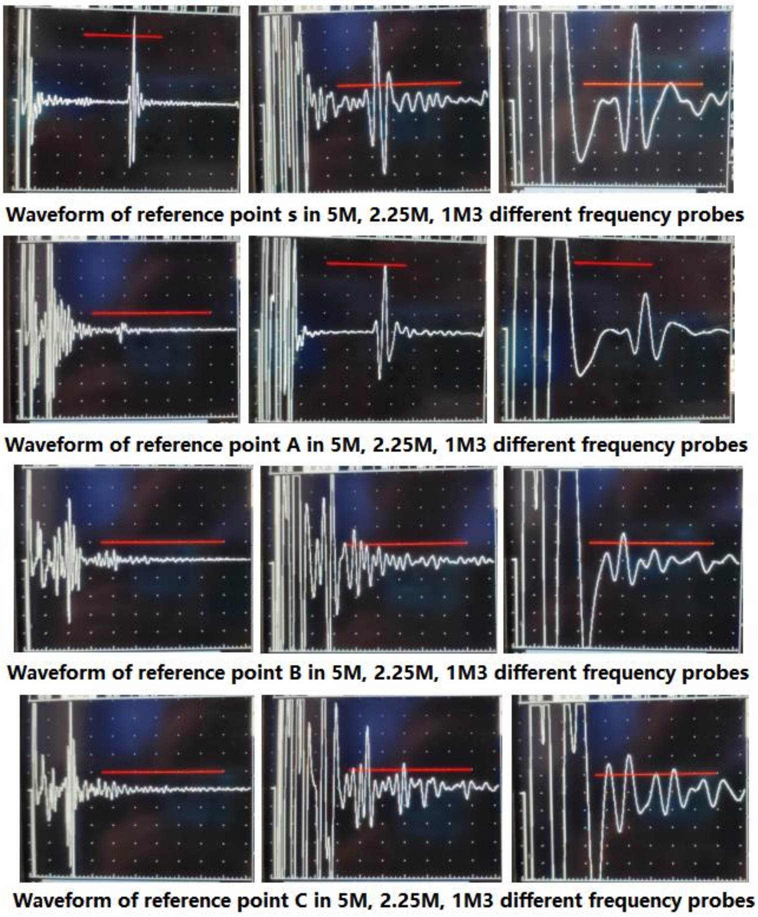

Figure 61: Reference point C waveform plot under 3 different frequency probes

It can be seen from the waveform chart that the reflected echoes at the three reference points are significantly different under the excitation of different frequencies of sound waves, which are summarized in Table 5.

Table 5: The reflected echo at the reference point is excited by sound waves at different frequencies

Probe frequency	*points S*	*points A*	*points B*	*points C*
5M (40dB)	The reflected echo on the underside is pronounced	No backdrop reflected echoes	No backdrop reflected echoes	No backdrop reflected echoes
2.25M (22dB)	The reflected echo on the underside is pronounced	The reflected echo on the underside is pronounced	No backdrop reflected echoes	No backdrop reflected echoes
1M (30dB)	The reflected echo on the underside is pronounced	The reflected echo on the underside is pronounced	The reflected echo on the underside is pronounced	No backdrop reflected echoes

Reference point ultrasonic echo signal analysis

(1) The reference point S has obvious reflected echoes at three different frequencies. The next three reference points are compared to the echo signal at reference point S at the same frequency and gain, respectively.

(2) When reference point A is detected by a 5M probe, under the same gain as the reference point S, no obvious reflected echo on the bottom surface is seen, and a group defect wave appears near the upper surface; When using 2.25M and 1M probes, the echo signal reflected on the back surface is obvious at the same gain as the reference point S.

(3) When reference point B is detected with 5M and 2.25M probes, under the same gain as the reference point S, no obvious reflected echo on the bottom surface is seen, and a group defect wave appears near the thickness of 1/2 of the upper surface; When using a 1M probe for detection, the reflected echo signal on the back surface is obvious at the same gain as the reference point S.

(4) When the reference point C is detected by three different frequency probes, there is no obvious reflected echo at the same gain as the reference point S, and the defect echo is distributed in many places and different thicknesses.

5.2 Intelligent Radial Image Recognition of Aircraft Structure Damage Based on Deep Learning[17]

In the process of aircraft structural strength test and field operation, the structure such as wall panel, skin, wing and control surface are prone to crack, broken nail and other damage under complex alternating load and external impact. In view of the aircraft structure internal damage detection, at present mainly rely on ray, ultrasonic detection and other technical means. At present, the damage determination of X-ray images mainly relies on manual work, and there are many missed detections in the actual detection process. The safety risks of aircraft structures can be greatly reduced by carrying out the intelligent recognition of damage of X-ray images based on deep learning.

Research Method

Due to the large cost of aircraft structure ray image acquisition, and the large amount of aircraft structure

[17] AVIC Aircraft Strength Research Institute

surface crack damage data, the shortcomings of insufficient ray crack image data can be compensated by using aircraft structure surface crack images through transfer learning. According to the damage data in ASRI aircraft structural damage database, aircraft surface structural cracks were trained as source domain data, and the obtained network weights were used to initialize the backbone network of the ray crack detection model, and the empirical knowledge learned from surface structural cracks was used to detect cracks in ray images. The overall research idea is shown in Figure 62.

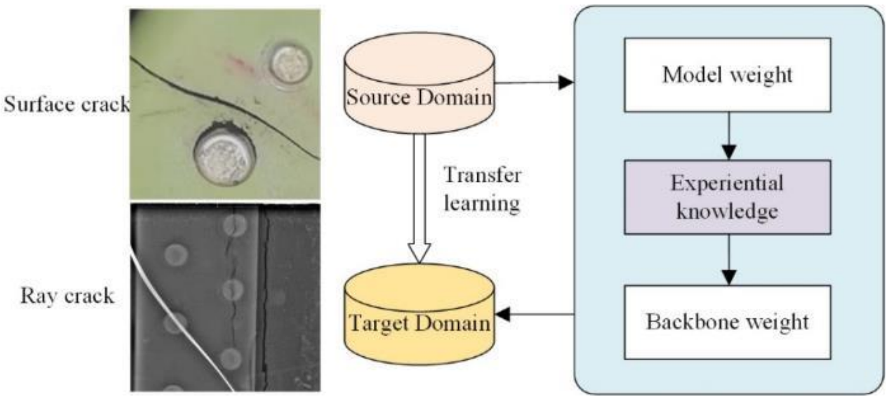

Figure 62: Overall Research Approach

Data Processing

Due to the large differences between aircraft structure surface cracks and ray cracks, it is necessary to preprocess the ray image before deep learning training. Aiming at the problems of noise, low contrast, scattering and so on in the original ray image, the ray image is filtered and enhanced. Figure 63 shows the enhancement effect of various filtering methods on the ray image. It can be seen from the figure that CLAHE method has obvious enhancement effect on the ray image and can significantly improve the crack features in the ray image.

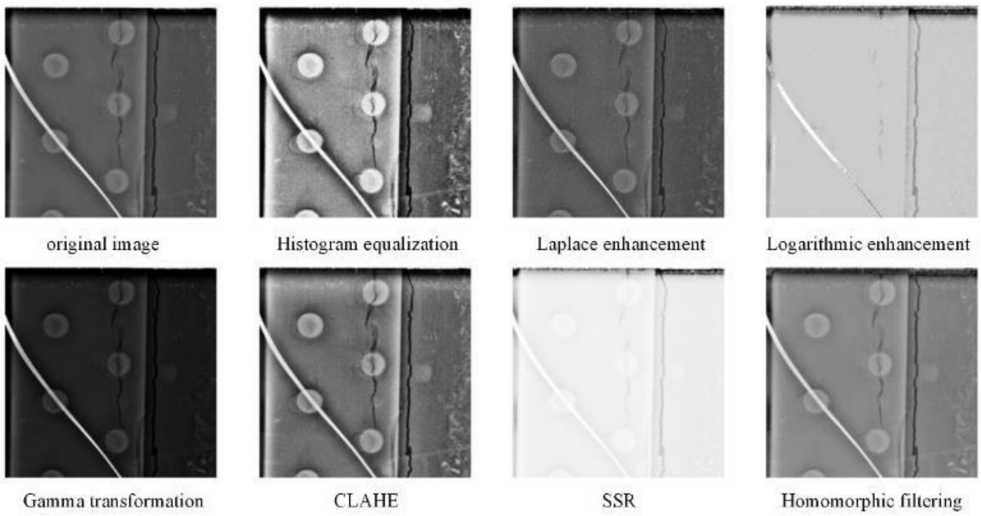

Figure 63: X-ray image enhancement results

Network Model

Ray intelligent detection of crack network model aircraft structure architecture using YOLOv7 as a whole. The CA attention mechanism is added between the middle and high-level features of the output of the backbone network, and the CA attention mechanism is added after strengthening the up-sampling module of the feature extraction network. Finally, the prediction results are obtained by using Yolo Head. The overall structure of the network is shown in Figure 64.

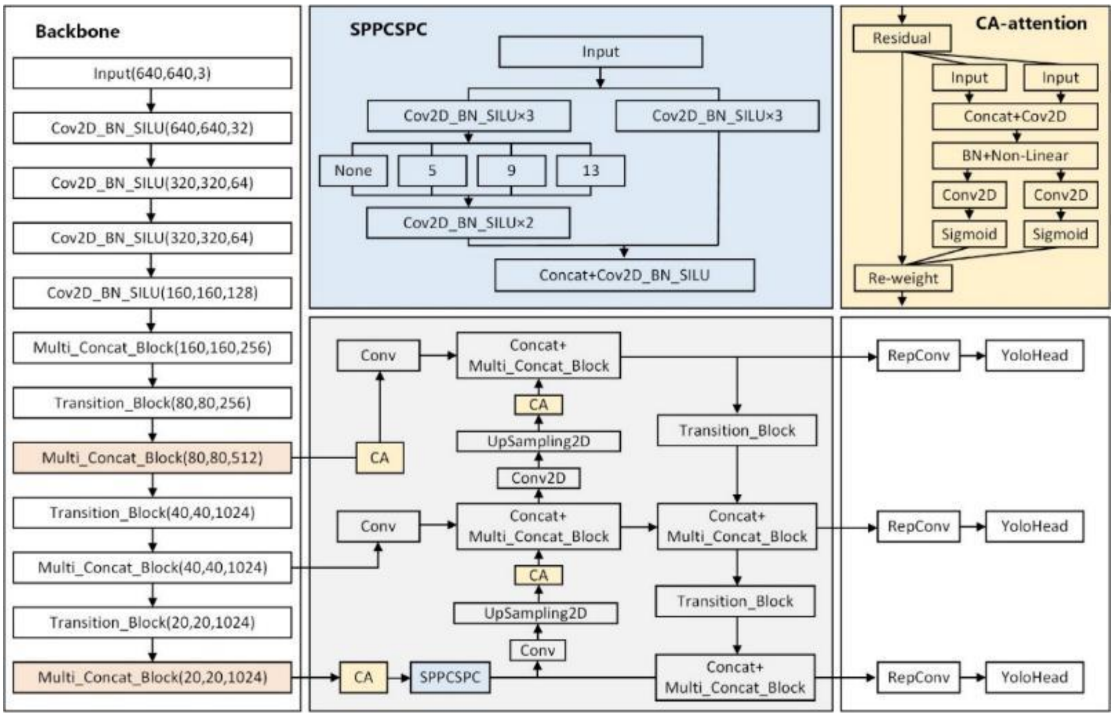

Figure 64: Intelligent ray crack detection network model based on attention mechanism

Detection Result

Based on the above detection network model, the aircraft structural crack and ray crack images were detected respectively, and the detection results were visualized based on Grad-CAM. By adding CA attention mechanism, the crack region focused by the network can be more accurate, and the crack detection rate reaches 96.3%, Some detection results are shown in Figure 65.

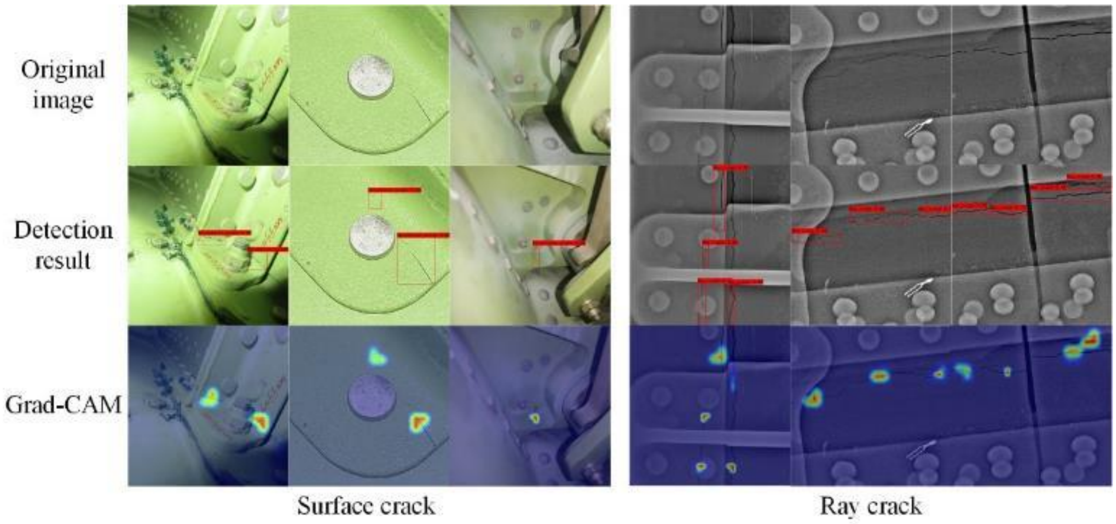

Figure 65: Results of intelligent identification of cracks in aircraft structure

6 STRUCTURAL INTEGRITY OF COMPOSITE LAMINATES

6.1 Study on Buckling and Post-Buckling Design and Analysis Method of Multi-wall Composite Plate[18]

With the progress of manufacturing technology, composite structures have been used more and more for the structure of airframe, and have been successfully applied to the main bearing structures such as wing panel. In order to realize the precise control of aircraft weight, it is necessary to study the buckling, post-buckling design and analysis method of composite wing panels.

Key techniques

The key techniques of buckling, post-buckling design and analysis of composite panel were solved by fining finite element analysis of a certain aircraft wing and comparing with the results of full-scale static test, such as the detailed nonlinear simulation analysis of full-size wing structure, the determination of critical instability point based on displacement field and the gradual damage analysis of integral wing structure.

DFEM simulation

Figure 66 is a DFEM model for a certain aircraft wing, which simulates the structural details such as opening, convex, stiffening and fastener, and accurately matches the actual structural stiffness of the wing. Figure 67 shows the process of quickly and accurately determining the critical buckling point of an integral wing structure by displacement field method. Figure 68 illustrates the process of failure prediction of wing structure by means of progressive damage analysis (composed of stress analysis, material failure criterion and damage material performance degradation).

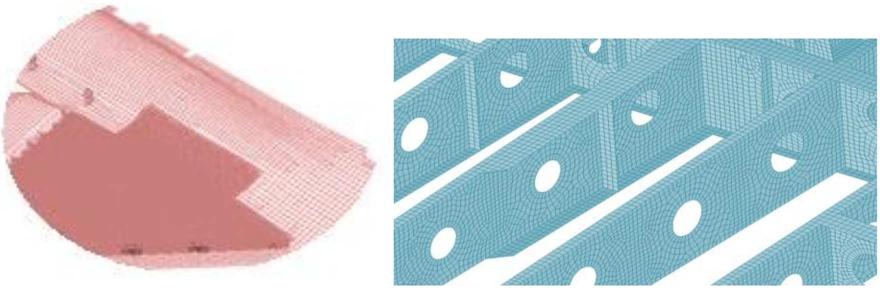

Figure 66: DFEM of full-size wing

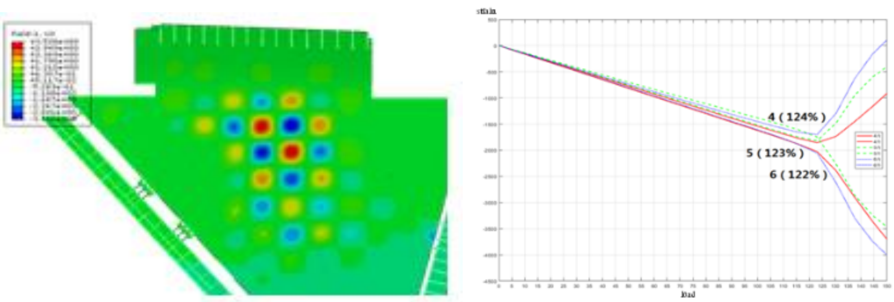

Figure 67: The critical buckling point of an integral wing structure

18 AVIC Shenyang Aircraft Design & Research Institute

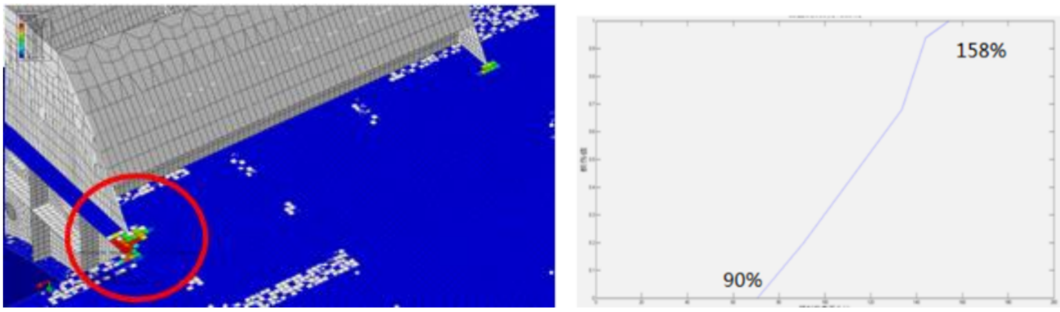

Figure 68: Progressive damage analysis of integral wing structure

Comparing with the full-scaled static test

Figure 69 shows the comparison of the buckling, post-buckling analysis and full-scale static test of the whole wing structure. The comparison shows that the nonlinear buckling results agree well with the test, with an average error of 9.5 %, and the accuracy of the analytical method is verified.

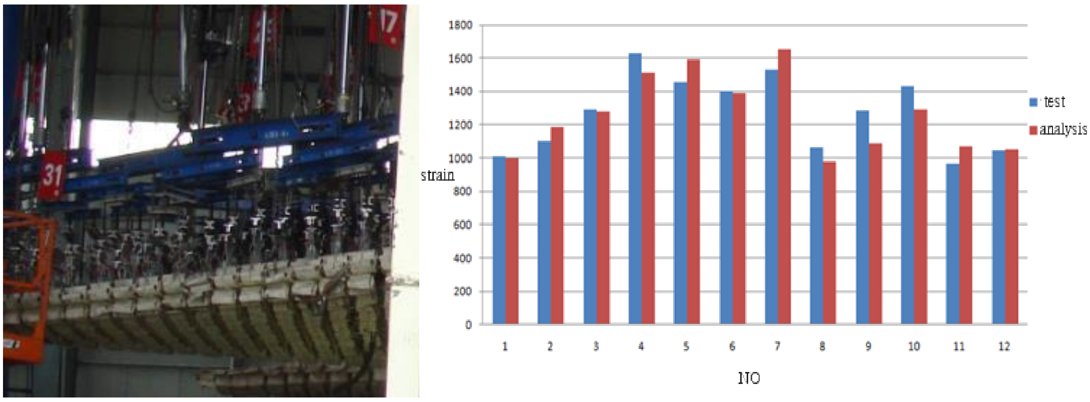

Figure 69: Contrast analysis with full-scale static test

6.2 Low-load Omission for Composite Structure Fatigue Test[19]

In the face of in-plane stress fatigue critical details, the second method is conservative since the fatigue threshold is comparable to the limit load level. For fatigue critical details with out-of-plane stress, the conservatism of the second method is questionable because the fatigue threshold is not very high relative to the failure load. This paper uses the fatigue threshold test data of a certain type of out-of-plane stress fatigue critical details and its limit load as the basis to demonstrate the correctness and feasibility of the second method.

Test piece and installation loading

The test pieces include typical out-of-plane stress detail test pieces of the horizontal tail section of a certain type of aircraft, that is, test pieces such as the stringer run-out, the triangular area of the beam, the four-point bending of the rib R angle, the pull-off of the fastener, and the bending of the rib R angle. The materials used for the test piece are shown in Table 6. The configuration and installation of the compression test piece at the stringer run-out is shown in Figure 70. The configuration and installation of the tensile test piece in the beam triangle area are shown in Figure 71, the configuration and installation

[19] COMAC Shanghai Aircraft Design and Research Institute

of the four-point bending test piece at the rib R angle are shown in Figure 72, the configuration and installation of the fastener pull-off test piece of the rib and skin connection are shown in Figure 73, and the configuration and installation of the rib R-angle bending test piece are shown in Figure 74.

Table 6: Material selection table of test piece

Material	***Specification***	***Single layer thickness (mm)***	***Material selection part***
carbon fiber unidirectional belt	CYCOM X850 resin Medium mold high strength carbon fiber IM+ Automatic tape laying。	0.185	Stabilizer skin, spar
	CYCOM X850 resin Medium mold high strength carbon fiber IM+ Manual pasting。		Stabilizer stringer
carbon fiber fabric	CYCOM 970 resin Standard mode high strength carbon fiber T300 Manual pasting	0.216	Stabilizer Rib
Structural film	/	-	Skin and Stringer Interface

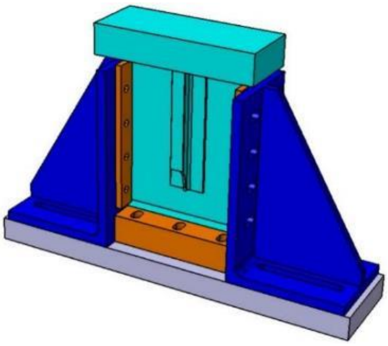

Figure 70: Schematic diagram of the installation of the compression test piece at the Stringer run-out

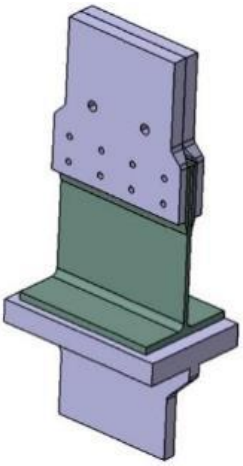

Figure 71: Schematic diagram of installation of tensile test piece in beam triangle area

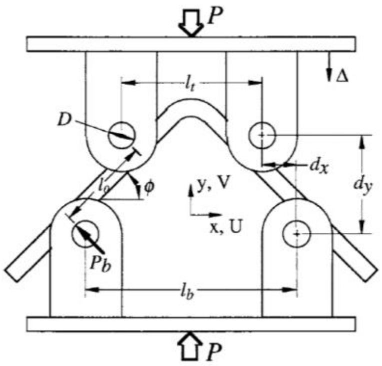

Figure 72: Schematic diagram of installation of four-point bending test piece with rib R angle

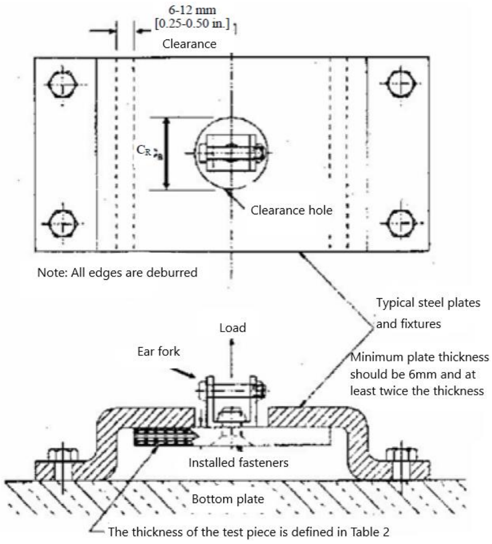

Figure 73: Schematic diagram of the installation of the pull-off test piece for the connection between the rib and the skin panel

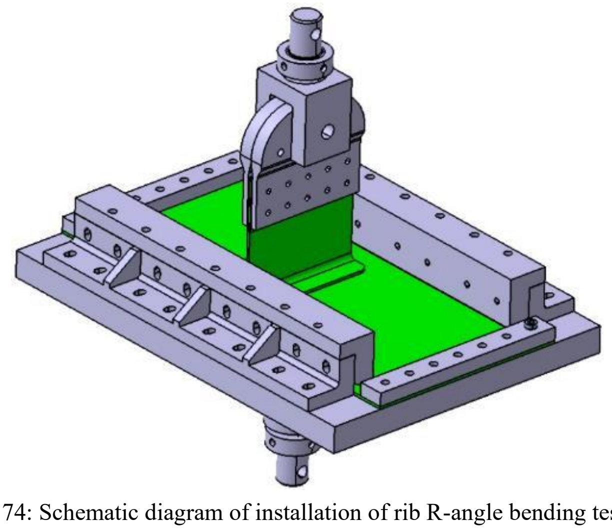

Figure 74: Schematic diagram of installation of rib R-angle bending test piece

Analysis of test results

The fatigue threshold value is the stress or strain corresponding to the 107 lives. The comparison between the fatigue threshold value of each detail and its stress under the limit load is shown in Table 7. It can be seen that 30% of the limit load is less than 60% of the fatigue threshold value. Therefore, it is conservative to take 30% of the limit load as the low load omission limit when the fatigue threshold test of the out-of-plane stress details has not been completed.

Table 7: Comparison of the fatigue threshold value of each detail and the stress under the limit load

Detail name	Fatigue Threshold (MPa)	60% fatigue threshold (MPa)	Limit load (MPa)	30% limit load (MPa)	$\frac{30\%\ limi}{60\%\ fatigue}$
Stringer run-out	74.7	44.8	56.9	17.1	38%
Beam triangle area	24.5	14.7	1.1	0.33	2.2%
Four-point bend of rib R angle	13.6	8.2	2.9	0.87	11%
Fastener pull-off	34.1	20.5	4.7	1.42	6.9%
Rib R angle bending	9.3	5.6	11.8	3.55	63.5%

Discussion

Fatigue threshold values of five types of typical out-of-plane stress fatigue critical details of composite flat tails are obtained through experiments；

For the 5 types of details, the two methods for value taking of the low load omission limit (i.e. 60% of the fatigue threshold value or 30% of the limit load) are compared, and it is proved that taking 30% of the limit load is a conservative approach, resulting in Load spectrum that will not lead to under-assessment；

The ratio of the fatigue threshold value of structural details with out-of-plane stress to its failure strength is not very high. In order to ensure that the out-of-plane fatigue characteristics of the structure meet the design requirements, the design stress level under the limit load needs to be controlled.

6.3 Static and Fatigue Research on Damage Failure Analysis and Evaluation Model of Composite Horizontal Tail Rib Structure[20]

In recent years, composite materials are basically used in the horizontal tail of civil aircraft in China and abroad. Although composite materials have been widely used in tail wing structures, their failure mechanisms are complex and there are many influencing factors. Compared with flat plate structures, the failure modes of stiffened rib structures are more complex. Rib structures will encounter various types of damage in the process of aircraft manufacturing, assembly and operation. Different types of damage will lead to different failure modes of the structure. Whether its residual strength meets the ultimate bearing capacity of the structure, and whether it needs to be repaired, these problems must be faced in the damage assessment of aircraft structures. Effective damage assessment plays an important role in the repair decision of composite materials.

Finite element model

The finite element model established for the composite horizontal tail rib structure is shown in Figure 75. The overall geometric dimension of the model is about 792mm×236mm, the grid size is 4mm×4mm.The web, stiffeners and load diffusion joints are simulated by shell element (S4R). The bonding element is arranged between the web surface and the lower edge strip surface of the five stiffeners, and

[20] AVIC Aircraft Strength Research Institute

the binding (tie) constraint connection is adopted. Hashin failure criterion is adopted for model failure.

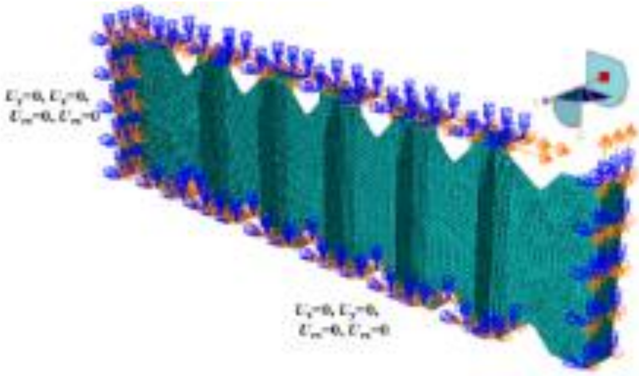

Figure 75: Finite Element Model of Composite horizontal tail rib

The material system of web and rib is CYCOM977-2-35-12KHTS-134 unidirectional and CYCOM977-2A-37-3KHTA-5H-280 fabric, with single layer thickness of 0.134mm and 0.280mm respectively. The material parameters are shown in Table 8. The strength of bonding element is taken as t_n=85.9MPa, t_s=t_t=117MPa, G_{Ic}=0.133N/mm, G_{IIc}=G_{IIIc}=0.459N/mm, and BK criterion is adopted, $\eta = 2$。

Table 8 Composite material parameters used for horizontal tail rib

	E_1 (GPa)	E_2 (GPa)	G_{12} (GPa)	G_{23} (GPa)	v_{12}
134 unidirectional	137.5	7.91	4.1	4.1	0.37
280 fabric	66.16	61.04	6.54	8.76	0.04
	X_t (MPa)	X_c (MPa)	Y_t (MPa)	Y_c (MPa)	S (MPa)
134 unidirectional	2293	1516	85.9	267.3	106
280 fabric	895.5	922.6	872.6	885.7	119

Damage mode of composite flat tail rib structure and its influence on residual strength and stiffness

The cumulative damage analysis of composite horizontal tail rib shows that there is no debonding failure at all web/rib interfaces at the rat hole position near the 1 # rib. Under the action of shear load, the damage mode of horizontal tail rib is shown as 0 ° layer fiber compression failure and 90 ° layer matrix compression failure, as shown in Figure 76.

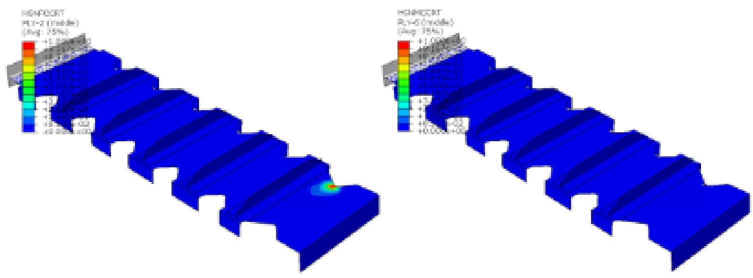

(a) 0 ° layer fiber compression failure (b) 90 ° layer matrix compression failure

Figure 76: Damage mode of composite wing rib at peak load

The distance D is defined as the minimum distance from the boundary of the initial damage area to the top of the rat hole, as shown in Figure 77. According to the calculation results, the critical distance between the initial damage area and the final failure area determines the residual strength of the flat tail rib.

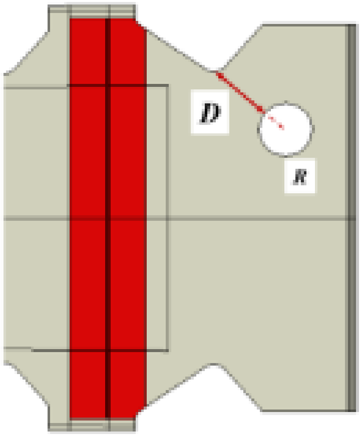

Figure 77: Schematic diagram of critical distance Dc

The relationship curve between strength recovery rate, stiffness and damage characteristics is shown in Figure 78. It can be seen from Figure 78 that with the increase of the length from the critical failure zone, the S_{RM} gradually approaches to a constant, indicating that the initial damage has no effect on the bearing capacity of the flat tail rib at this time.

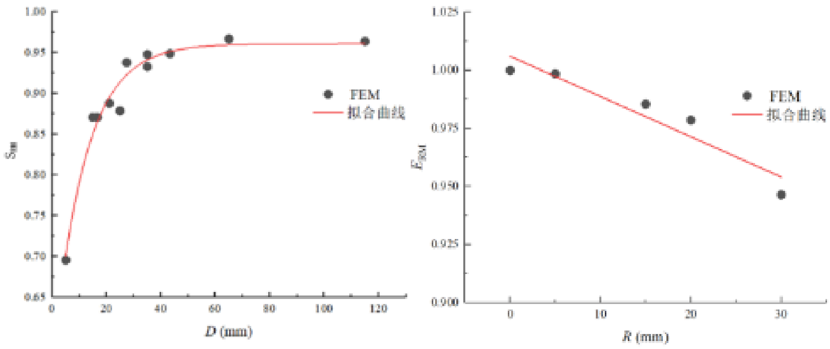

a) strength recovery rate with minimum distance top   b) stiffness recovery rate with initial damage opening radius

Figure 78: Relationship between strength recovery rate, stiffness and damage characteristics

For the defect/damage of the web of the horizontal tail rib structure, when the distance between the initial defect/damage area and the final damage area is greater than the critical distance, the initial damage of the horizontal tail rib has no effect on the stress distribution at the dangerous location of the structure. When the distance between the initial defect/damage area and the final damage area of the structure is less than the critical distance, the initial defect/damage area has mutual influence on the stress distribution near the key damage area of the structure. For the 15mm initial defect/damage size studied in this paper, the critical distance is 40mm. Based on the results of finite element analysis, this paper establishes a curve model of the relationship between the initial damage size of the web, its distance from the key damage area and the residual strength, which improves the design and engineering evaluation ability of the composite horizontal tail rib structure, and has certain engineering practical value for the design and evaluation of the residual strength of the horizontal tail rib structure.

6.4 Rationalized Improvement of Tsai–Wu Failure Criterion Considering Different Failure Modes of Composite Materials[21]

Advances in the design methodology of aircraft structures require deep understanding about the failure behaviour of materials, particularly the fibre reinforced polymer (FRP) composites, which have been increasingly used in modern civil aircrafts for improved fuel efficiency and payload capacity. The effective design of structural composites for aircrafts must ensure the safety of the components while maximising the lightweight potential of FRPs, which relies on accurate prediction of the material strength during the design phase. Whilst various failure criteria and analysis approaches have been proposed for FRP composites structures during the last decades, their predictive accuracy is still limited in industrial applications. This research has enabled further refinements and corrections to the existing failure theories for FRPs and therefore provided designers with more confidence about the predictive accuracy for the strength of composites in aeronautic structures.

Improvements and verification

The Tsai–Wu failure criterion is widely used in the design and failure analysis of composite structures due to its simplicity and high prediction accuracy. However, the Tsai–Wu criterion still cannot distinguish the failure modes of composite materials, which limits its further application in practice. In this study, an improved criterion was proposed based on the reasonable assumption that composites exhibit infinite strength under pure hydrostatic pressure. Some coefficients in the quadratic tensor expression of the Tsai–Wu failure criterion are redetermined using the basic strength value of the material, including the coefficient F12, under four different stress states (fiber tension and compression, matrix tension and compression). The reconstructed Tsai–Wu failure criterion can distinguish the failure modes based on different coefficient values under different stress states. In the progressive damage analysis of composite materials, the stiffness can be reduced in different manners based on each failure mode. Experimental verifications for different kinds of unidirectional composites under various stress states was conducted, which are presented in Figure 79-Figure 81, demonstrating that the improved Tsai–Wu failure criterion has a better prediction ability and accuracy than the original criterion.

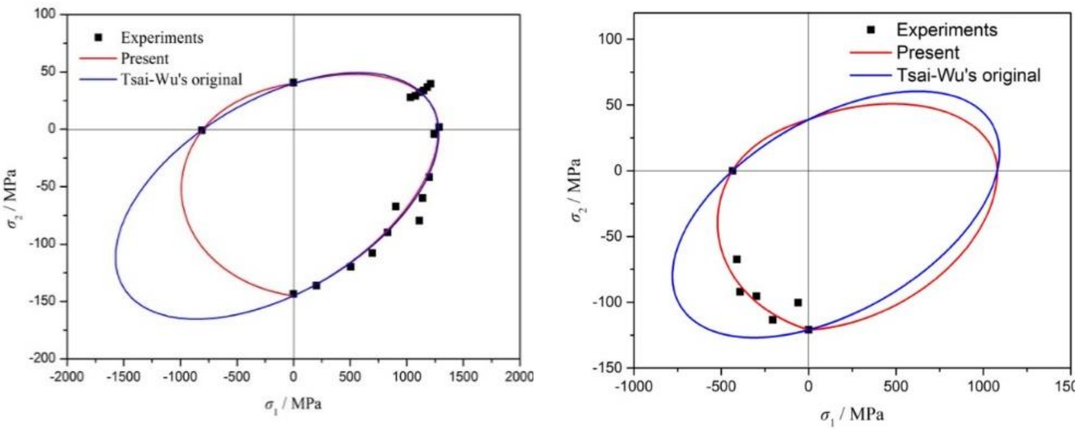

a) b)

Figure 79: Comparisons between the predicted failure envelopes and experimental results under the σ1−σ2 biaxial stress state for (a) E-glass/MY750, and (b) E-glass/epoxy.

[21] AVIC Aircraft Strength Research Institute

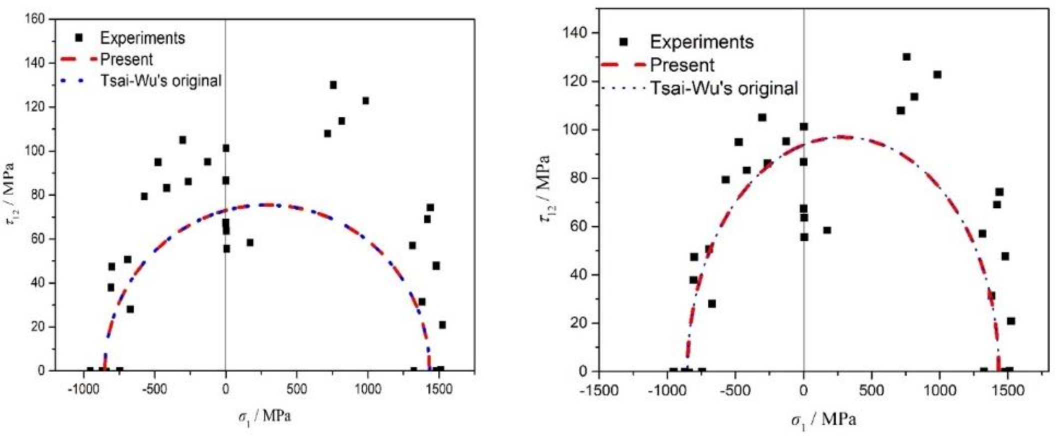

a) σ1−τ12 b) σ1−τ12

Figure 80: Comparison of the predicted failure envelopes and experimental results under the σ1−τ12 biaxial stress state for T300/BSL914C (a) with S21 = 73 MPa and (b) with the modified S21 = 93.8 MPa.

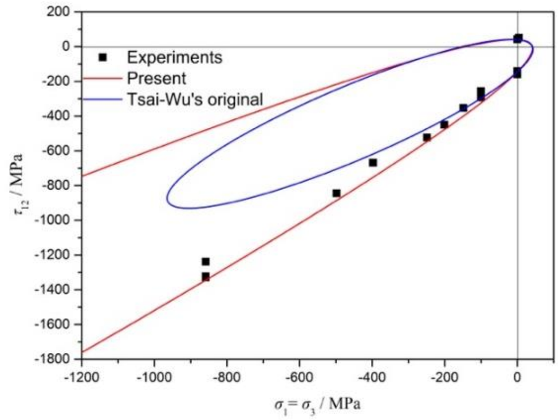

Figure 81: Comparison of the predicted failure envelopes and experimental results under the τ12−σ1 (σ1 = σ3) stress state for T300/BSL914C.

6.5 Post-Buckling Failure Analysis of Composite Stiffened Panels Considering the Mode III Fracture[22]

Fully utilizing the post-buckling capacity of stiffened composite panels is important to reduce the weight of aeronautical composite structures. However, owing to the complex post-buckling failure modes and mechanisms, there are no effective analysis methods. This research explores the impacts of the mode III fracture energy on the damage behavior of the stiffener–skin interface of composite stiffened panels under post-buckling conditions.

Methods and key findings

To characterize the bonding interface damage, an interface damage initiation criterion considering the effects of through-thickness compression on the shear failure was used and combined with the Reeder damage extension criterion, which considers the mode III fracture. The mode III fracture toughness characteristics of the damage evolution of the stiffener–skin interface were obtained using the edge crack torsion test method. Moreover, the compressive deformation response, buckling load, buckling modes,

[22] AVIC Aircraft Strength Research Institute

failure load, and failure modes of the panel were obtained by a compression test of I-shaped stiffened panels. Based on the aforementioned experimental data and numerical model, the post-buckling behavior of the I-shaped stiffened composite panels with an open cross-section stiffener was studied. It was found that the mode III fracture energy caused by the longitudinal shear stress τ31 played a major role in the stiffener–skin interface damage extension of the stiffened panels, as shown in Figure 82. Therefore, the mode III fracture behavior should not be ignored in the post-buckling analysis. As presented in Figure 83, the numerical analysis method developed can accurately predict the damage initiation and evolution processes of the composite panel interface. The method can be effectively used for post-buckling analysis of aeronautical composite panels.

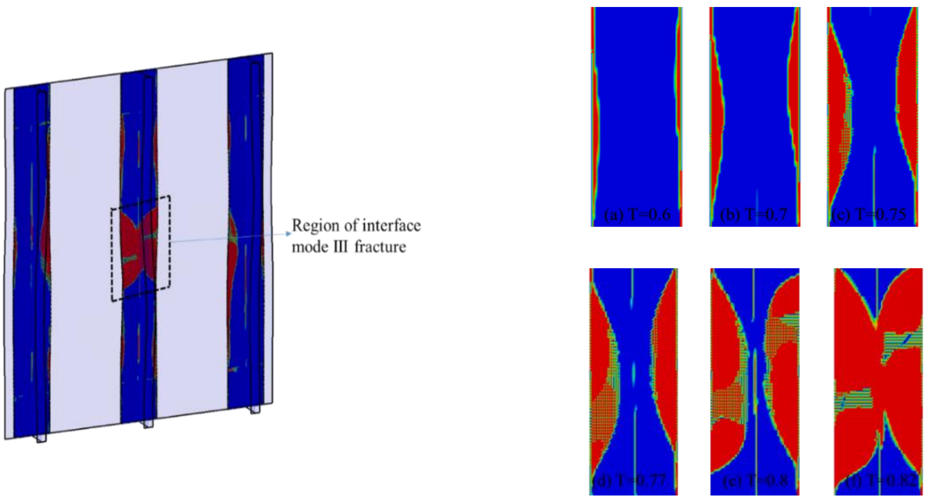

a) b)

Figure 82 Damage extension of the I-shaped stiffened panel: (a) The mode III fracture zone at the panel interface; (b) Damage extension of the mode III fracture zone at the interface.

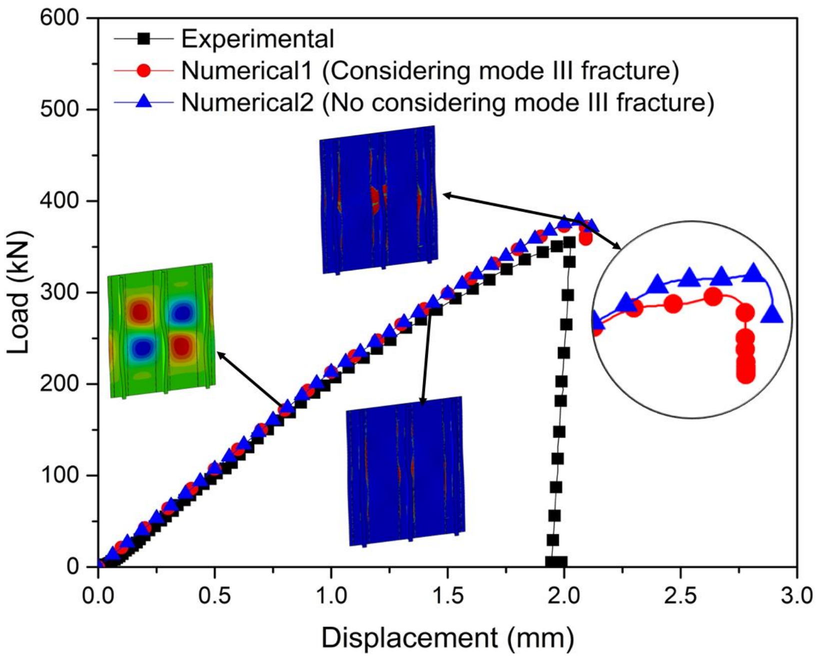

Figure 83 Load–displacement curves of experimental and finite element analysis.

6.6 Interaction Formulae for Buckling and Failure of Orthotropic Plates Under Combined Axial Compression/Tension and Shear[23]

For the stability design of orthotropic plates, especially the postbuckling design, the failure envelope of panels should be calculated as well as the buckling interaction curve under combined loads. However, the failure envelopes have been mainly obtained by biaxial tests or finite element simulations. Until now, an interaction formula for failure under combined loads that can predict the failure envelope more accurately has not been found. In the present study, interaction formulae were constructed by using axial tension/compression and in-plane shear loads for orthotropic plates. The buckling interaction and failure interaction formulae of orthotropic plates under combined loads were constructed. The predictions of the buckling interaction curves and failure envelopes were in excellent agreement with the combined compression and shear test data of composite panels with symmetric and balanced lay-ups.

Experiment

An interaction function was constructed based on the axial compression/tension and shear loads of orthotropic plates. The coefficients of the polynomial function were determined by uniaxial test results. Buckling interaction and failure interaction formulae under combined axial tension/compression and shear loads were established. To verify the validity of the interaction formulae, buckling and failure tests of five kinds of Ω-stringer stiffened composite panels (See Figure 84a) under combined compression and shear loads were carried out. Combined compression and shear load tests were conducted on a new combined loading experiment system designed by the Aircraft Strength Research Institute of China, as shown in Figure 84b.

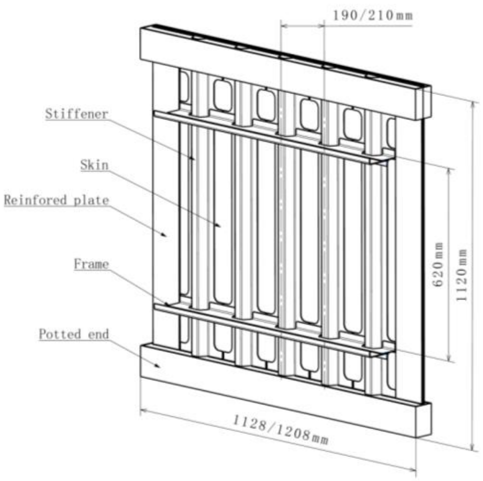

a)

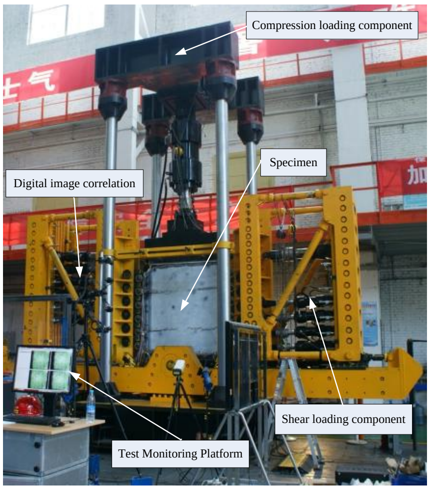

b)

Figure 84 (a) Structural configuration of the panel and (b) Combined compression and shear loading test system

Buckling interaction curves and failure envelopes

Based on the uniaxial load test results of orthotropic plates, the buckling load and bearing capacity under any proportion of the combined loads could be predicted by using the proposed interaction formulae. The buckling interaction curves and failure envelopes predicted by the proposed interaction formulae were in excellent agreement with the test results, as shown in Figure 85 and Figure 86. As shown in Figure 85, the predicted buckling interaction using the formula proposed in this paper is compared with the test

[23] AVIC Aircraft Strength Research Institute

results for different loading conditions. The initial buckling loads under combined loads are presented in Table 9.

Table 9: Initial buckling loads of stiffened panel under combined compression and shear.

Specimen number	Initial buckling loads(kN)				
	Compression	Shear	Combined loads (Compression: Shear)		
P1	544:0	0:292	301:199	429:141	179:237
P2	789:0	0:351	391:250	535:170	227:291
P3	708:0	0:359	388:257	561:185	238:315
P4	909:0	0:486	519:331	709:226	311:397

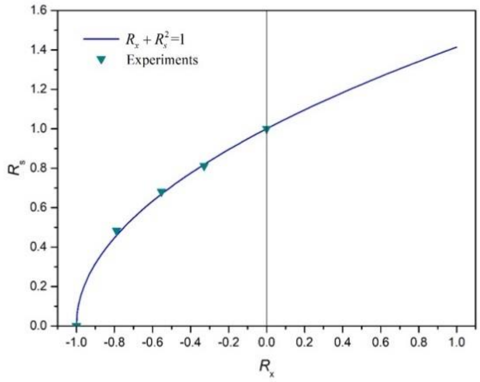

a) P1

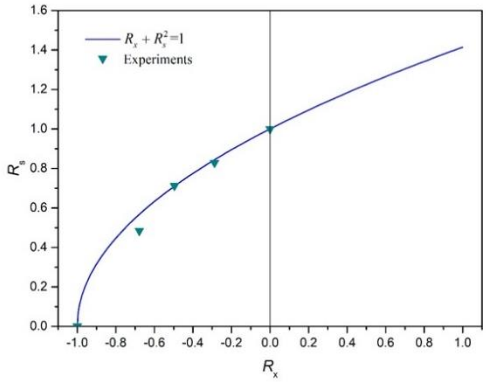

b) P2

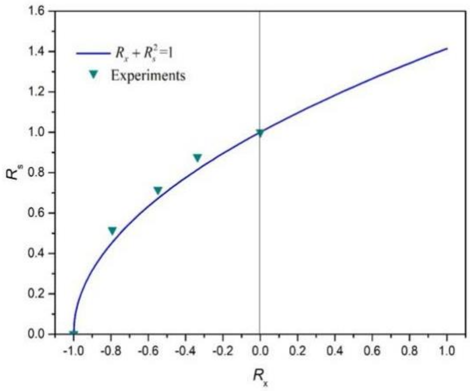

c) P3

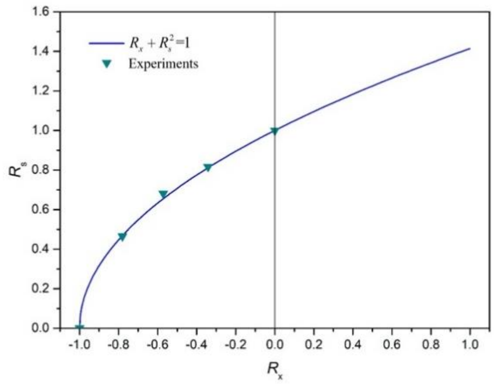

d) P4

Figure 85: Comparison of predicted and experimental buckling interaction curves under combined compression and shear

The bearing capacity of a plate with an arbitrary ratio of combined axial and shear loads can be determined by the proposed failure interaction formulae through uniaxial tension, compression, and shear load test results. Moreover, when the tensile strength of the panel is approximately infinite, the failure interaction formulae under combined compression and shear loads still have sufficient accuracy for engineering calculations. As shown in Figure 86, the failure envelopes predicted by the proposed interaction formulae were in excellent agreement with the experimental results under combined compression and shear loads. The interaction formulae under other types of combined loads can be easily obtained by using the methods proposed in this paper.

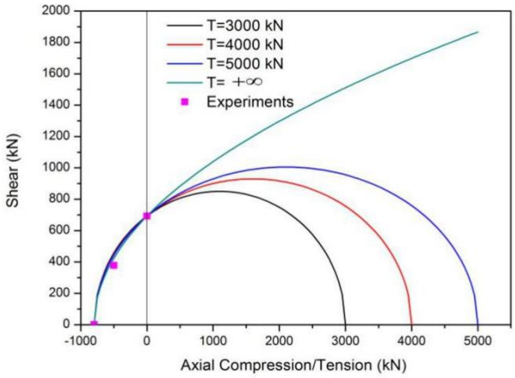

a) P1

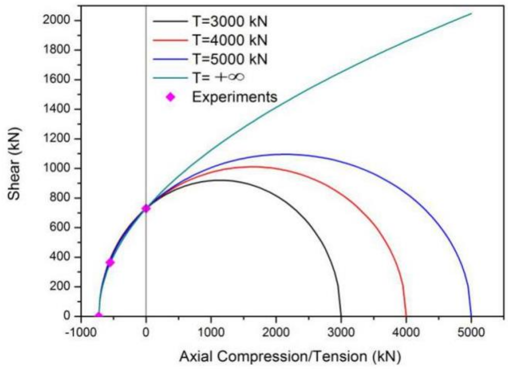

b) P2

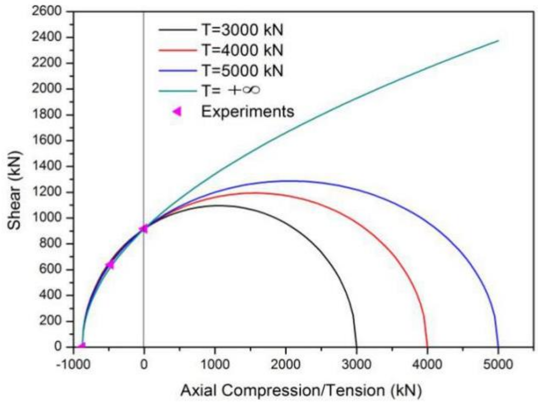

c) P4

Figure 86: Comparison of the predicted and experimental failure envelopes under combined compression and shear loads.

7 ADVANCED MATERIALS AND INNOVATIVE STRUCTURAL CONCEPTS

7.1 Experimental Study on Mechanical Properties of Laser Powder Bed Fused Ti-6Al-4V Alloy Under Post-Heat Treatment[24]

The mechanical and fatigue resistance of additively manufactured (AM) metals is based on its microstructural features and defects, that can be mitigated by post-processing. Currently, understanding the effect of metallurgical defects on fatigue life is a significant step towards the wider application of AM alloys. Here, the tensile properties of laser powder bed fused (L-PBF) Ti-6Al-4V alloys, with varied annealing temperatures (650 – 950℃) were studied, and fatigue resistance under the optimized annealing temperature was investigated.

Experimental procedure

The cylindrical Ti-6Al-4V parts with different build directions (BD) were prepared by L-PBF (see Figure 87), and some of the as-built cylindrical samples were treated at 650◦C, 750◦C, 800◦C, 850◦C and 950◦C for 2h, followed by furnace cooling.

---

[24] AECC Beijing Institute of Aeronautical Materials

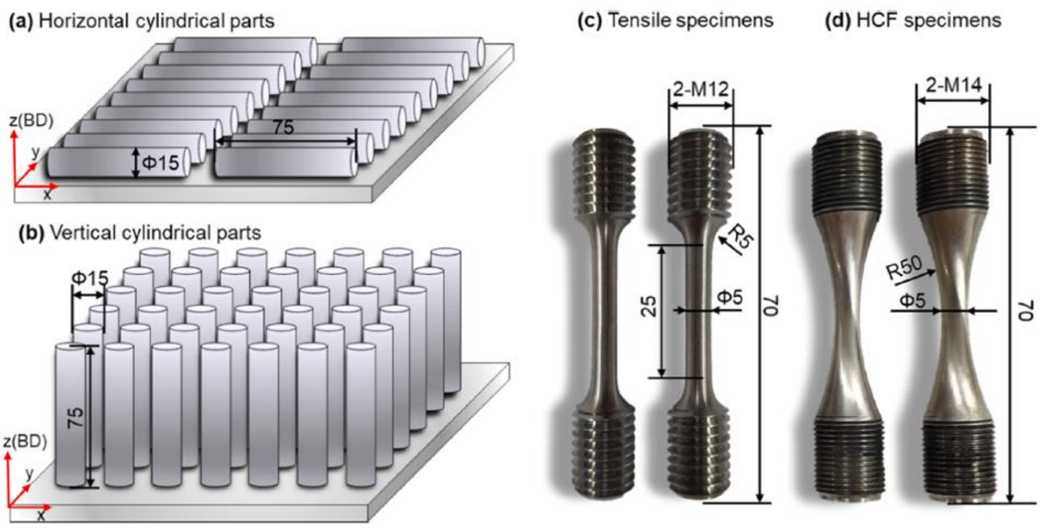

Figure 87: (a) Horizontally and (b) vertically built cylindrical parts. Sampling schematics for the (c) uniaxial tensile and (d) high cycle fatigue (HCF) test pieces. (Unit: mm).

Microstructure and mechanical properties

As shown in Figure 88 and Figure 89, with the increase of annealing temperature, the original acicular martensite α' phase is gradually transformed into lamellar $\alpha + \beta$ phases and the mechanical properties show the trend of decreased strength and increased elongation. The annealing heat treatment of 800℃/2 h will obtain the best strength/plasticity match.

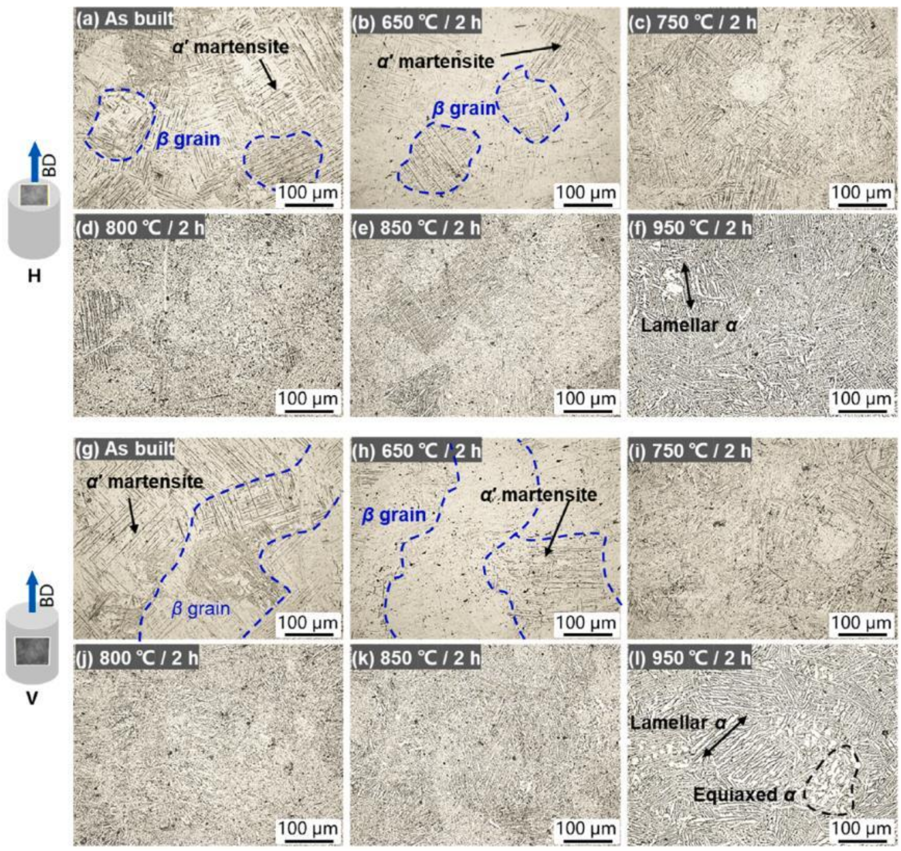

Figure 88: Comparisons between optical microstructures of L-PBF built Ti-6Al-4V alloys for the (a–f) H and (g–i) V samples after treatment under different annealing conditions.

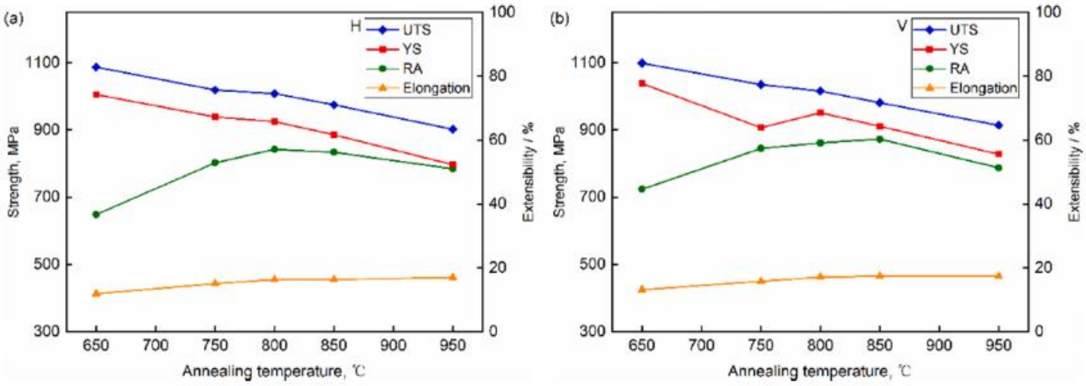

Figure 89: Influences of annealing temperatures on YS, UTS, elongation and RA of the (a) H direction specimens and (b) V direction specimens.

Fatigue resistance evaluation

After annealing, the HCF strength at 10^7 cycles of the L-PBF Ti-6Al-4V alloy is 415 MPa under the stress ratio of 0.06 (Figure 90). Defect sizes are the critical factor in the scatter of fatigue S-N data and surface defects of various sizes typically act as crack initiation sites, leading to poor fatigue resistance (see Figure 91).

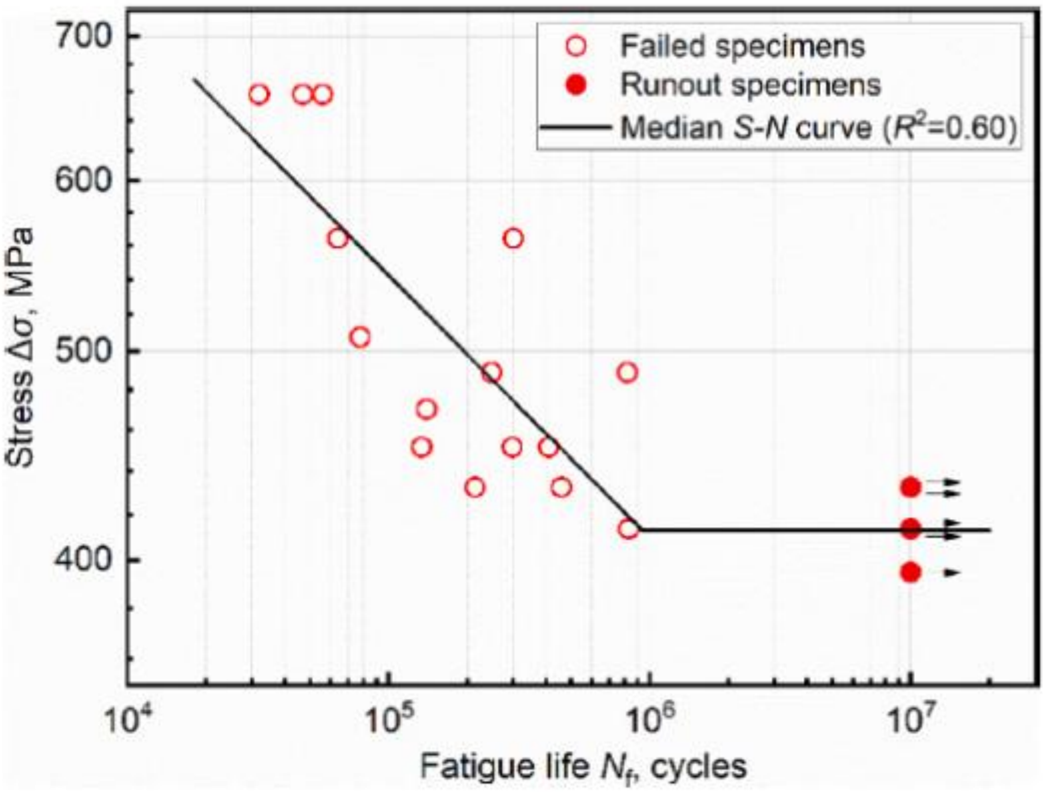

Figure 90: Fatigue S–N curve of vertically built HCF specimens under stress ratio R of 0.06.

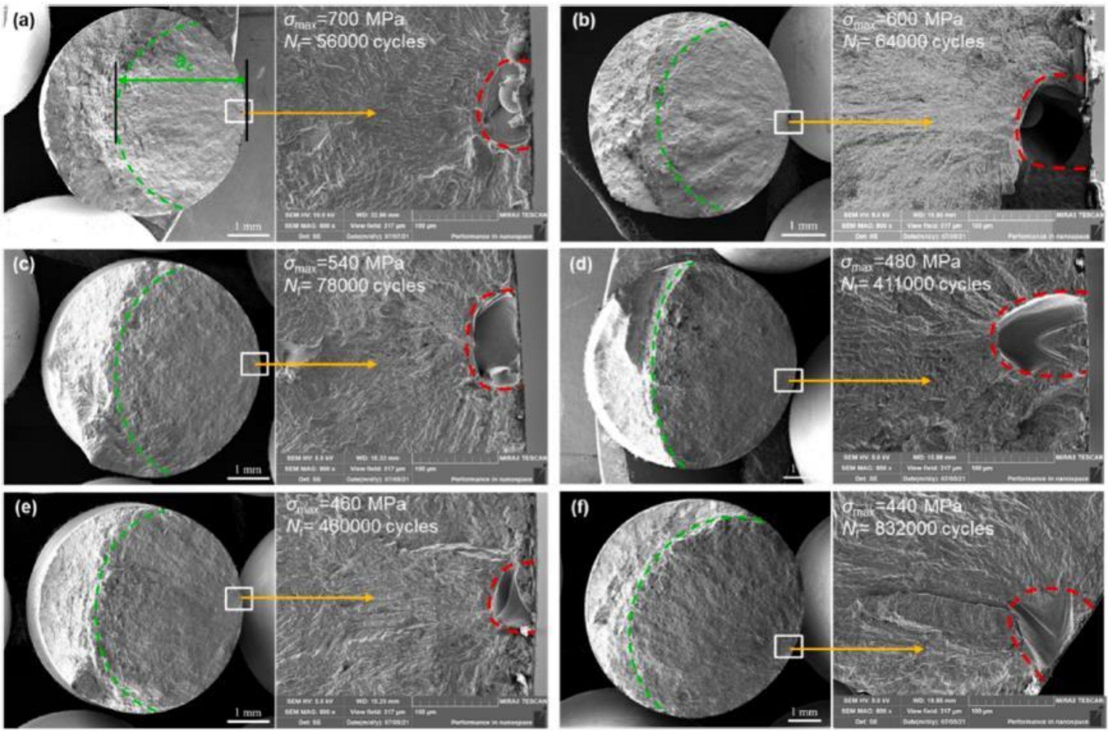

Figure 91: Comparisons between fracture surfaces of representative HCF specimens and magnified images of the crack initiation regions.

Fatigue strength prediction

The KT diagram (Figure 92) modified by the El-Haddad model is proven to better fit the HCF data than LEFM and Murakami approaches. Considering the probability distribution of defect sizes, probabilistic fatigue strength assessment can be done for the L-PBF Ti-6Al- 4V alloy by using the EVS method and improved KT diagram.

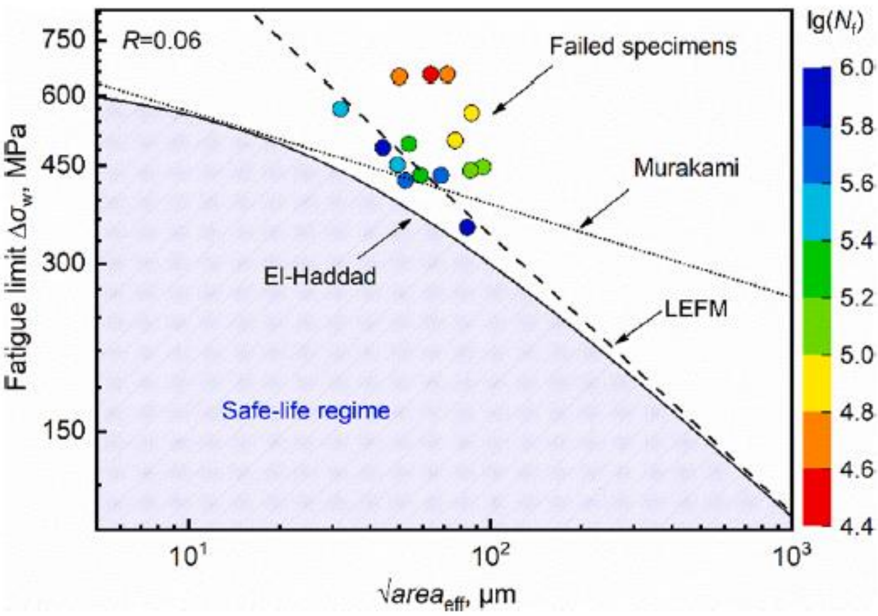

Figure 92: KT diagram based on the LEFM criteria, El-Haddad model, and the Murakami approach together with the HCF data.

An efficient HCF life prediction model (equation (1)) based on a normalized fatigue S-N curve is proposed, to correlate the critical defect size and the local stress with fatigue life. The scatter of the fatigue life, based on the normalized fatigue S-N curve is significantly reduced, compared to the original fatigue S-N model.

$$N_p = C\left(\frac{\Delta K_{th,LC}}{Y\sqrt{\pi\left(\sqrt{area_{eff}}+\sqrt{area_0}\right)}}/\Delta\sigma_{loc}\right)^m$$

7.2 Integral Analysis of Additive Manufacturing Ti6Al4V Titanium Structure[25]

Additive manufacturing Ti6Al4V titanium alloy has a great potential to be applied in aviation structural components due to its excellent corrosion resistance and high specific strength, and its mechanical performance shows strong relationships with the build direction, defect distribution, and residual stress. On the other hand, complex flight load.

Anisotropic behaviors of additive manufacturing Ti6Al4V titanium alloy

The effect of build direction on mechanical performance is related to the load condition. The 0° sample has a good performance under the compression and double shear loading, while the 90° sample has higher ultimate flexural strength and torsional strength. The 45° sample has better ductility under tensile and torsional loadings. The anisotropy of AM Ti6Al4V depends on the coupling effect of the columnar grain and the consecutive deposition layer interaction.

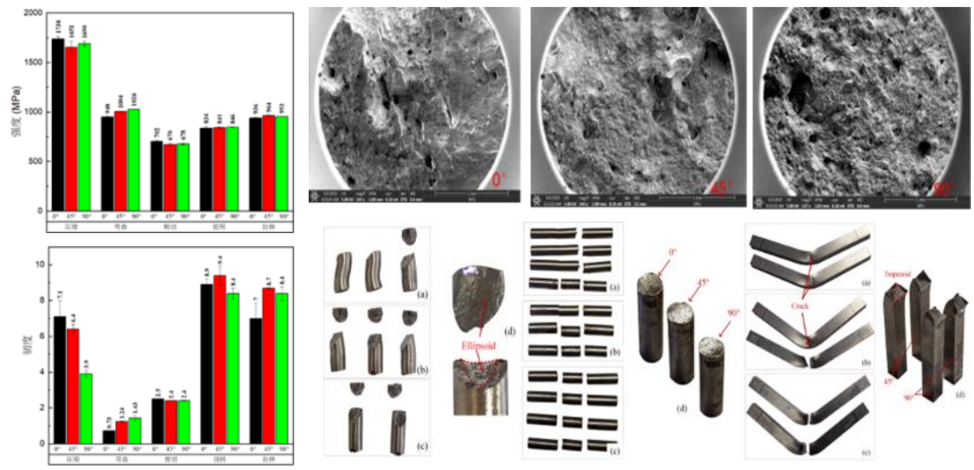

Figure 93: Mechanical responses under static loads

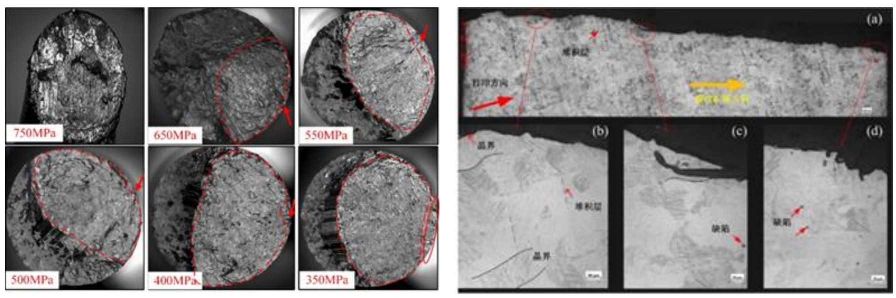

Figure 94: Fracture surface and crack path under fatigue load

25 Northwestern Polytechnical University

Spatial defect distribution

The defect distribution of AM Ti6Al4V shows strong relationship with the build direction, and the profiles of deposition layer and the section change has an important influence on the porosity distribution. The porosity curve fluctuated periodically along the build direction due to the accumulation of the defects in the interlayers. The porosity near the subsurface region with a distance of 300 μm is much higher than that of the other regions.

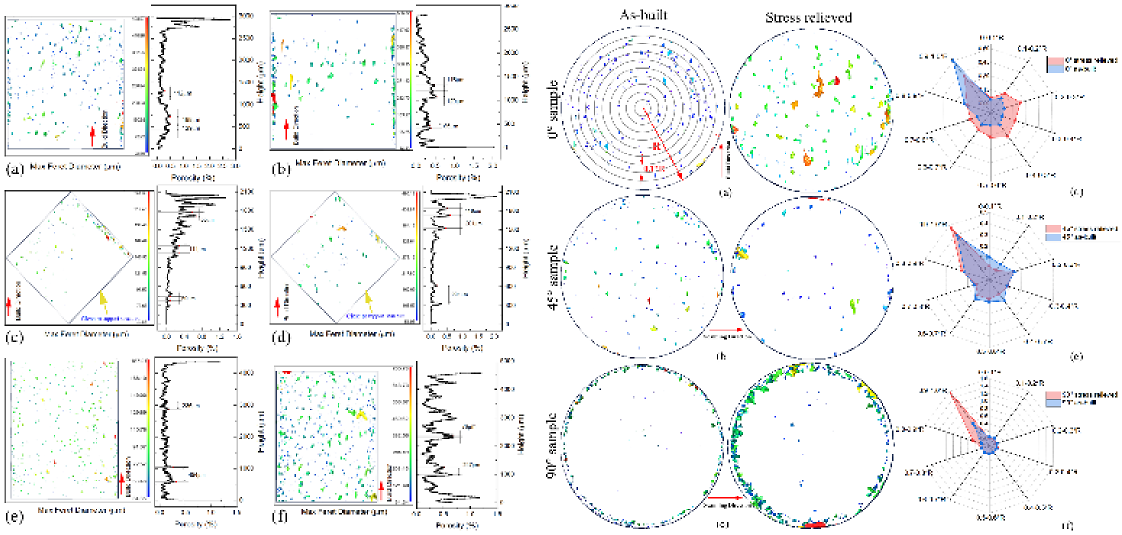

Figure 95: Defect distribution along the build direction and radial direction

Residual stress effects

Anisotropic residual stress state in AM Ti6Al4V is obvious, and it is related to the build direction. The residual stress (RS) along the build direction is more than 3 times higher than that along the scanning direction. The RS can cause the mixed mode I/II fracture and lead to the crack deflection. Fatigue cracks are prone to propagate along the deposited layers when the angle between the crack growth direction and the deposited layer is small. After post-treatment, the anisotropy of residual stress state and fatigue crack growth behavior decreased.

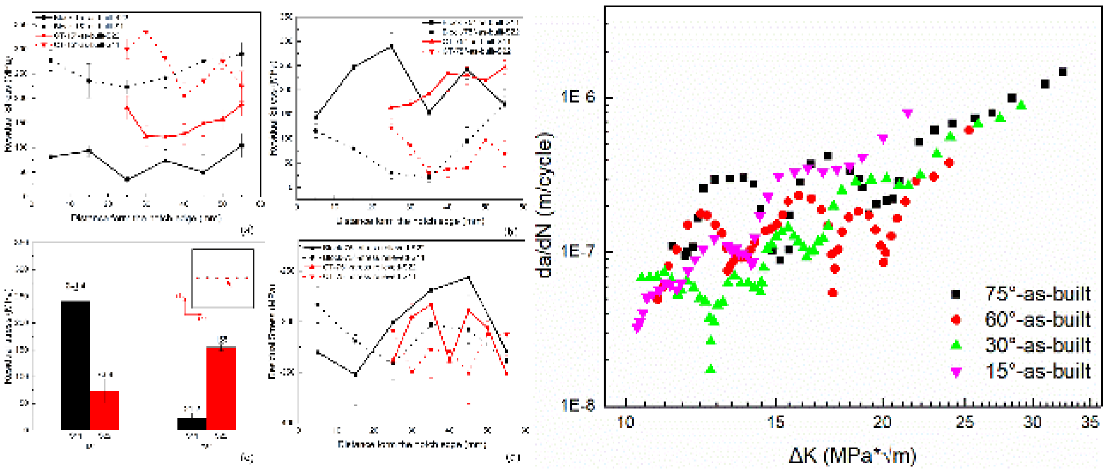

Figure 96: Anisotropy of the residual stress and fatigue crack growth rate

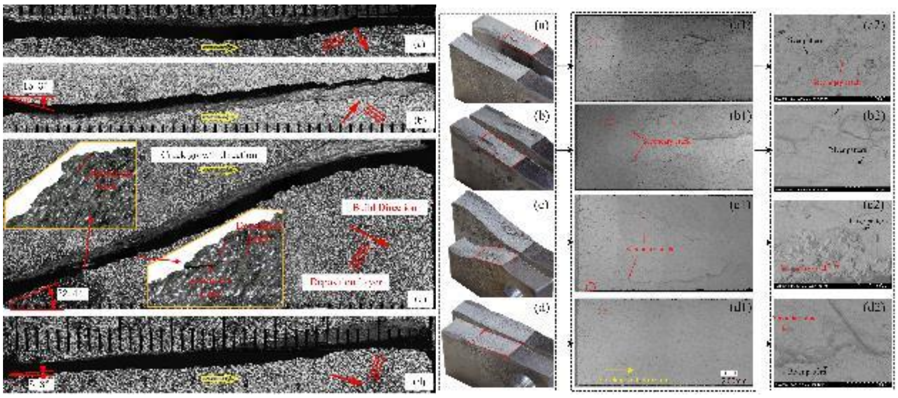

Figure 97: Crack paths and fracture surfaces of samples in different build direction and RS states

8 FULL-SCALE STRUCTURAL TESTING

8.1 Crashworthiness Pyramid Test Technology of Double Passageway Composite Fuselage Structure[26]

Composite materials have been widely used in aircraft structures, and gradually applied to the main load-bearing structure. However, the brittle characteristic of composite materials has brought new challenges for aircraft crashworthiness design and evaluation. How to obtain the energy absorption characteristics and mechanical behavior under impact loads has become one of the major technical problems for the double passageway composite fuselage structure

Several key techniques has been successfully solved in the crashworthiness pyramid test technology of double passageway composite fuselage structure, including the pyramid test plan, typical energy-absorbing element selection test and full-scale composite fuselage structure crash test.

Pyramid test of composite fuselage structure

The test matrix is optimized based on the requirements and design feature of airplane, as shown in the fig.1.

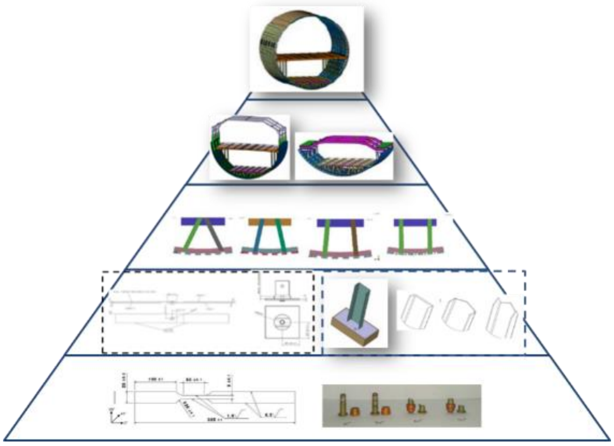

Figure 98: Pyramid test plan of composite fuselage structure

[26] COMAC Shanghai Aircraft Design & Research Institute

Typical energy-absorbing element selection test

In a survivable crash, the sub-cargo structure is the main energy-absorbing component in the process of an aircraft crash. As an important energy-absorbing element during a crash, the composite stanchion has an important impact on the crash resistance of the sub-cargo structure. The vertical crash test of the sub-cargo structure was carried out. Comparing the structural deformation failure modes and energy absorption conditions, the relationship between energy absorption characteristics of the sub-cargo structure at a crash speed of 30ft/s and the angle of the stanchion, the thickness of the stanchion and the trigger form are obtained. The results show that for the sub-cargo structure, the structure with a reasonable stanchion thickness can significantly improve the crash resistance and energy absorption capacity of the lower column assembly structure.

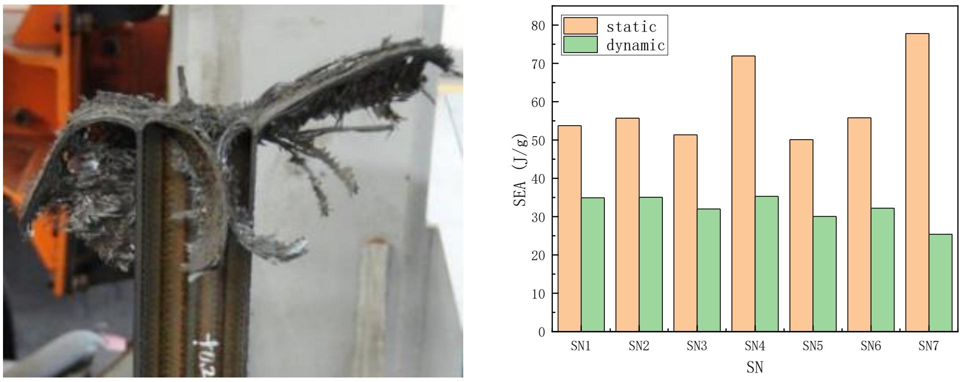

Figure 99: Typical wave section test sample’s image and comparison of tested specimens on the average SEA

Full-scale composite fuselage structure crash test

Figure 100: Comparison of the the sub-cargo structures deformation

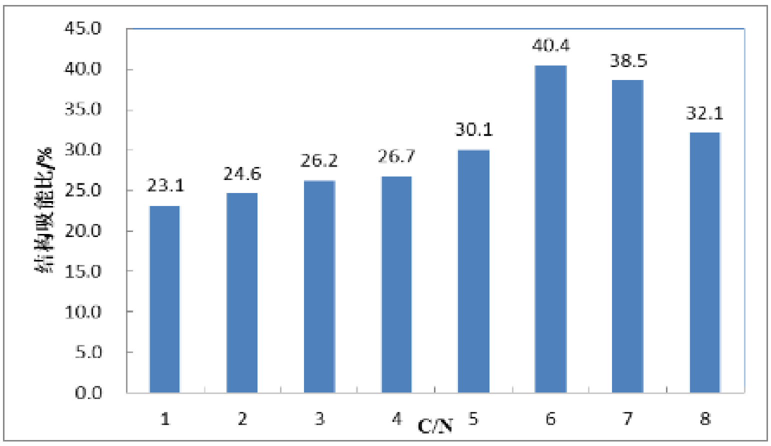

Figure 101: Comparison of the average structure energy absorption for all sub-cargo configurations

Full-scale composite fuselage structure crash test

The world's largest crash test of composite fuselage structure has been put into practice, considering for the top luggage、dummy and seat, as shown in the Figure 102. Retention of items of mass、maintenance of acceptable acceleration and loads experienced by the occupants、maintenance of a survivable volume and occupant emergency egress paths are fully researched.

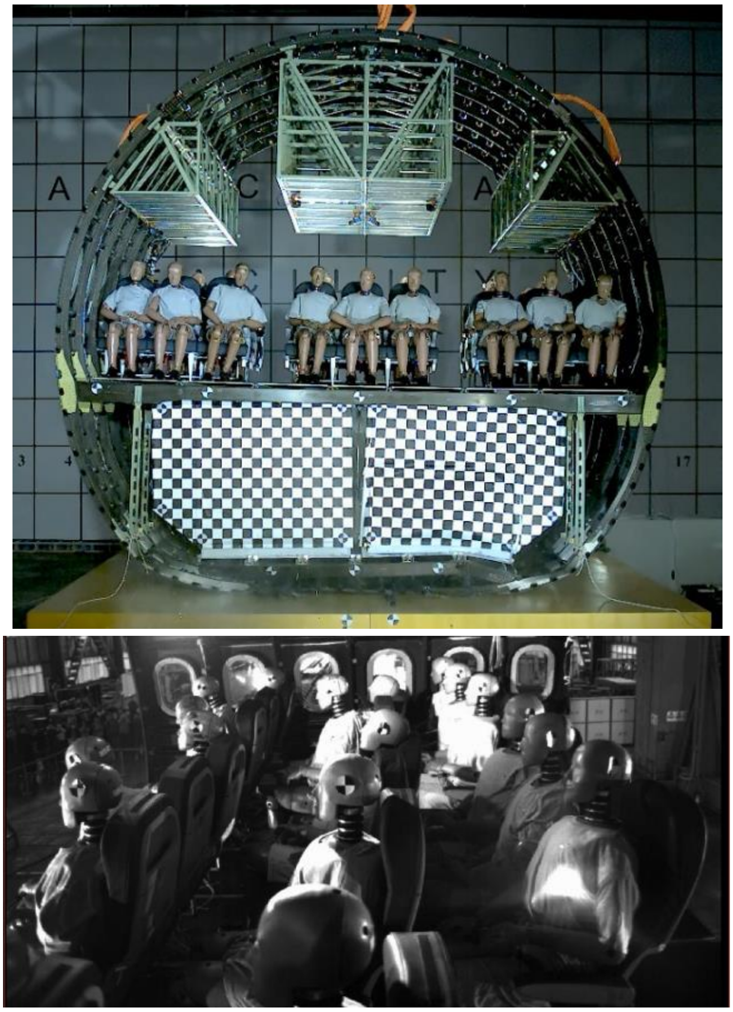

Figure 102: Full-scale composite fuselage structure crash test

8.2 Fatigue Design and Test Technology of Helicopter Spherical Flexible Rotor Hub [27]

The rotor system of helicopter rotates continuously in flight. The vibration and coupling loads are generated by the rotor blades in the asymmetric flow field. High cycle fatigue loads are the main components of the rotor system. Hub is the core part of the spherical flexible rotor. The problems of fatigue design and test load application of the hub under complex loads are studied.

Combination force system of hub

The relationships between the loads F_{Xi}, F_{Yi}, F_{Zi} (18 in total) at the connections with the elastic bearing,

---

[27] AVIC Helicopter Research and Development Institute

the loads F_{ai} (6 in total) at the connections with the damper and the loads M_X、M_Y、C, T_X, T_Y, P (6 in total) at the center of rotor are analyzed, and the combined force system of hub is characterized by them, as shown in Figure 103.

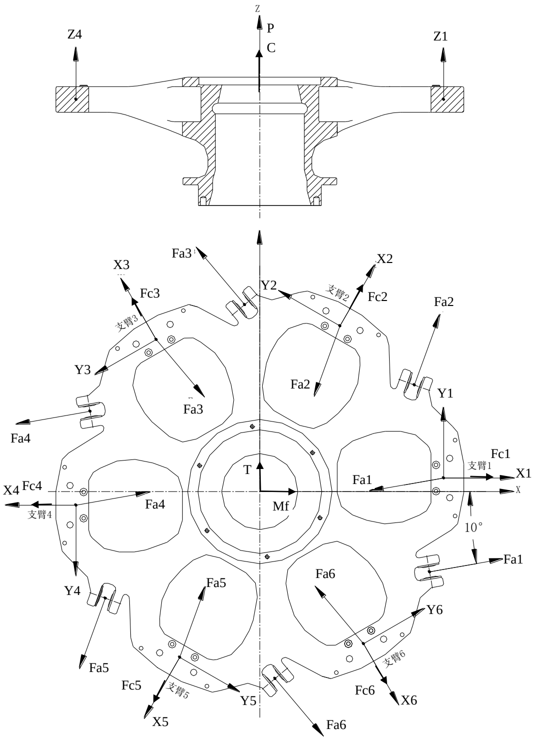

Figure 103: Combined Force System of Hub

Stress analysis of hub

The stress analysis model of hub under each load and each working case is established. The stress-load sensitivity analysis of each part is carried out to determine the dangerous parts of low cycle fatigue and high cycle fatigue and corresponding fatigue characteristic loads. The stress analysis and stress-loading-position sensitivity analysis results are shown in Figure 104 and Figure 105respectively. It can be seen that the high cycle stress level of position 5~ position 8 is high, and the fatigue characteristic load is M_f $\left(M_f = \sqrt{{M_X}^2 + {M_Y}^2}\right)$.

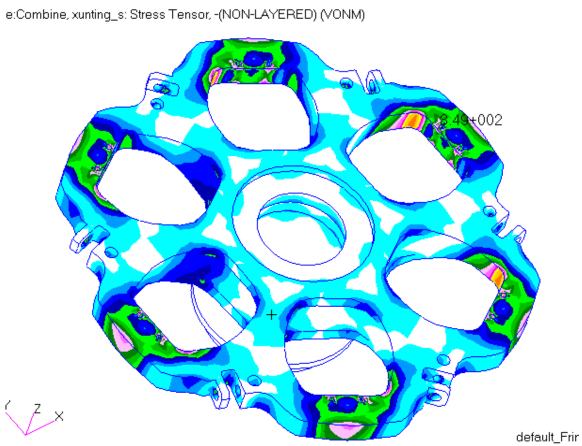

Figure 104: Stress Analysis of Hub

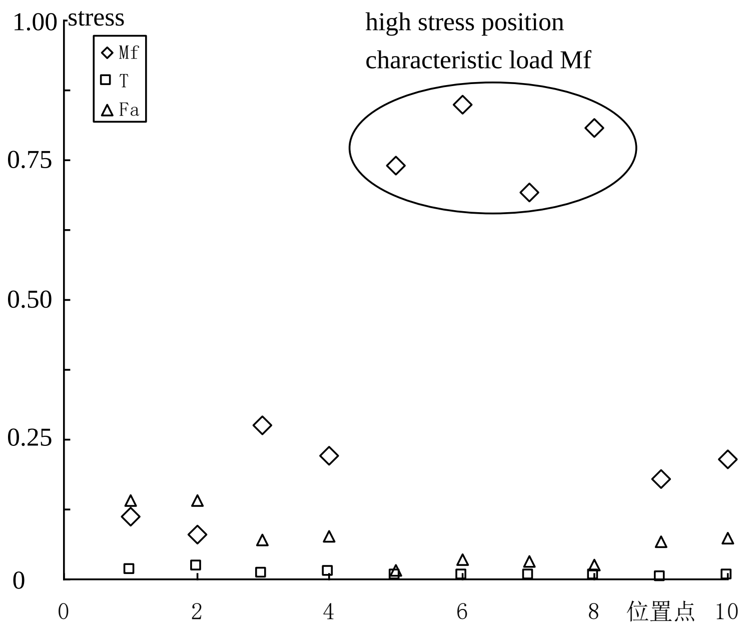

Figure 105: Stress-loading-location Sensitivity Analysis of Hub

Fatigue test of hub

Fatigue tests of the damper connection simulation part test, the damper connection test and overall test of hub are carried out, as shown in Figure 106.

In the overall fatigue test, hub is constrained at the connection with the rotor shaft, 18 actuators and 6 actuators are used for coordinated loading at the connections with the elastic bearing and at the damper respectively. The stress is measured in the test to verify the correctness of the stress analysis model. The test results are compared with the fatigue design results, and the failure analysis of the test part exceeding the expectation is carried out to verify the accuracy of the design technology, and the fatigue life of hub is finally substantiated. It is found that the unreasonable grinding process could lead to the formation of molten droplets on the surface of titanium alloy hub, as shown in Figure 107.

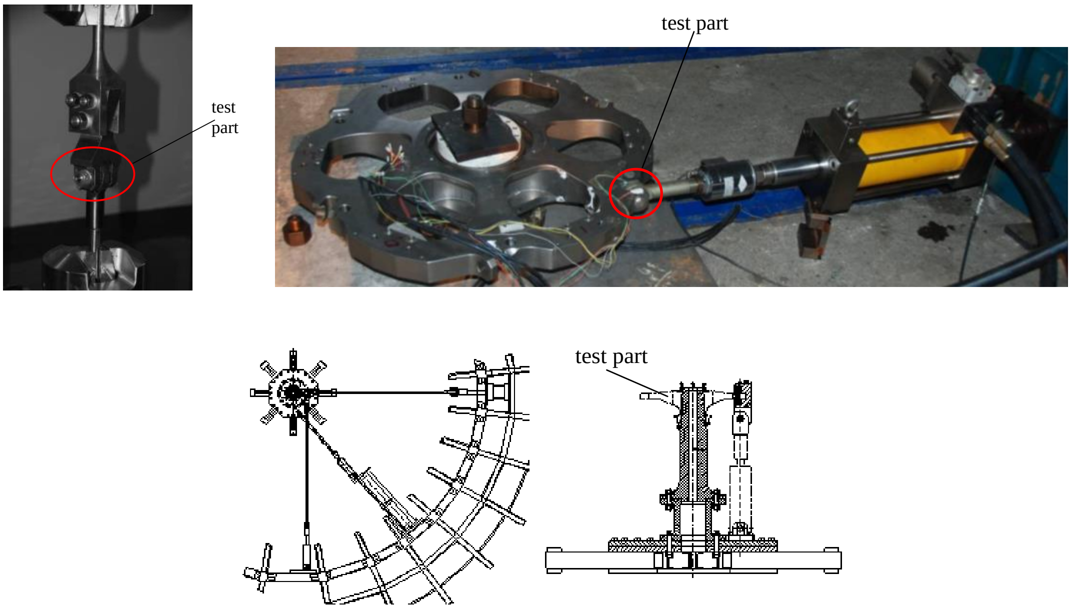

Figure 106: Fatigue Test of Hub at Three Levels

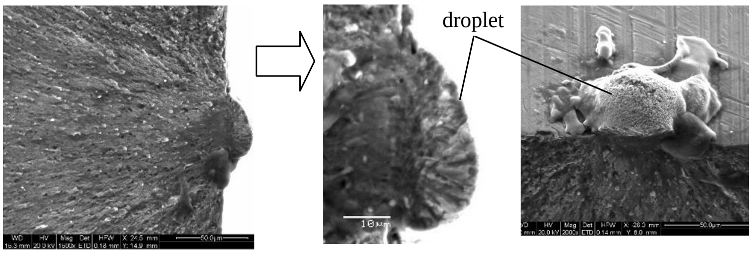

Figure 107: Surface Droplet

8.3 Rigid Loading Accelerates Full-Scale Aircraft Fatigue Test[28]

According to the structural characteristics of the test piece and the layout of the nodes of the tension pad, the tension pad lever system is designed in three forms. class A is a planar connection, where all the lever connection points of the lever system are in a plane; class B is a linear connection, where all the lever connection points of the lever system are in a straight line; class C, a mixture of class A and class B.

The primary lever is of variable section design and is bolted to the tension pad. The single lug is designed in two sizes, one is a single lug with a circular hole and a joint bearing, which serves to fix the lever position and release the rotational degrees of freedom, and the other is a long lug with a long hole, which serves to release the translational degrees of freedom caused by the deformation of the system and restrain the rotational degrees of freedom of the system in both directions, thus forming a static connection between the primary lever and the tension pad. The design result is shown in Figure 108.

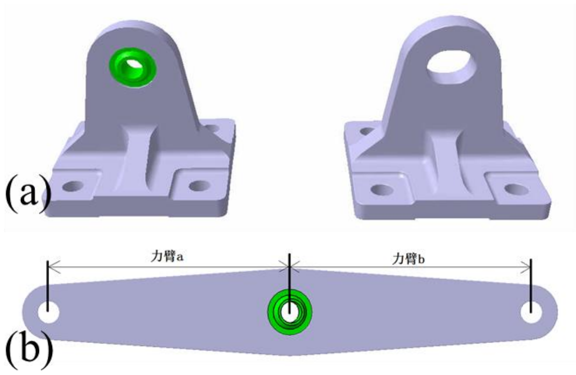

Figure 108: Primary lever design diagram ((a): Single lug design form. (b) Lever structure form.).

The secondary lever is designed to be connected according to the position of the primary lever. The secondary lever of the large angle class, the angle with the primary lever is within 90°±26°, the same plane lap design form, in the plane with the primary lever through the joint bearing connection, the middle hole to install the joint bearing. The linear connection type secondary lever, in a straight line with the primary lever, is directly connected with the primary lever by bolts, with a long hole at one end and a round hole at the other, and the middle hole is fitted with a joint bearing. The design principle of the final lever is the same as that of the secondary lever. The low stress area of the lever is grooved to reduce the weight of the lever system while avoiding stress concentration. The typical lever form is shown in Figure 109.

---

[28] AVIC Aircraft Strength Research Institute

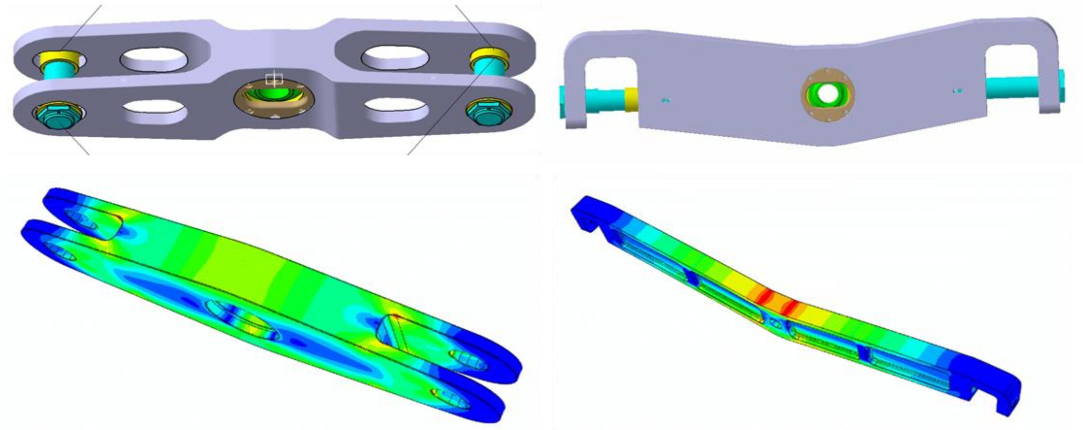

Figure 109: Schematic diagram of typical lever design and analysis results.

Typical design results for a tension pad - lever system

The wing, vertical tail and lateral fuselage parts of the aircraft are loaded by the tensile type tension pad-lever system, and the nose and rear fuselage vertical loads are applied by the shear type tension pad-lever system, as shown in Figure 110.

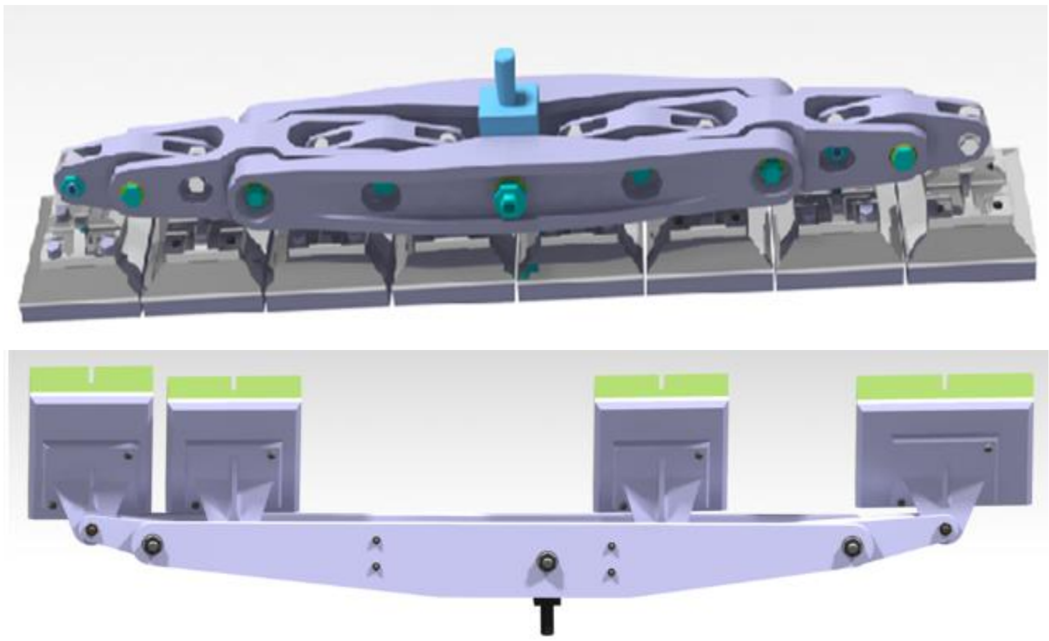

Figure 110: Typical results of tension pad-lever system design.

Full-Scale Aircraft Fatigue Test Application Examples

The above new technology is applied for the first time in the fatigue test of full-scale structure of C919 aircraft, in which the tension pad-lever system is applied to the wing vertical, nose vertical, rear fuselage vertical and fuselage lateral loading, in which 34 wing vertical loading points, 12 nose/tail vertical loading points and 10 fuselage lateral loading points are arranged symmetrically on both sides and loaded in a synchronized and coordinated manner.

The project completed installation and commissioning on November 28, 2019, and completed the 2000-cycle fatigue test by the end of December 2019, and has since continued to operate at a rate of about 2500 flights per month under the condition of continuous optimization of the control parameters. The test data showed that the loading accuracy of the full-scale fatigue test met the test requirements, the systems operated well, and no malfunction occurred during the test, and the use of the new test technology achieved the expected purpose. The test implementation is shown in Figure 111.

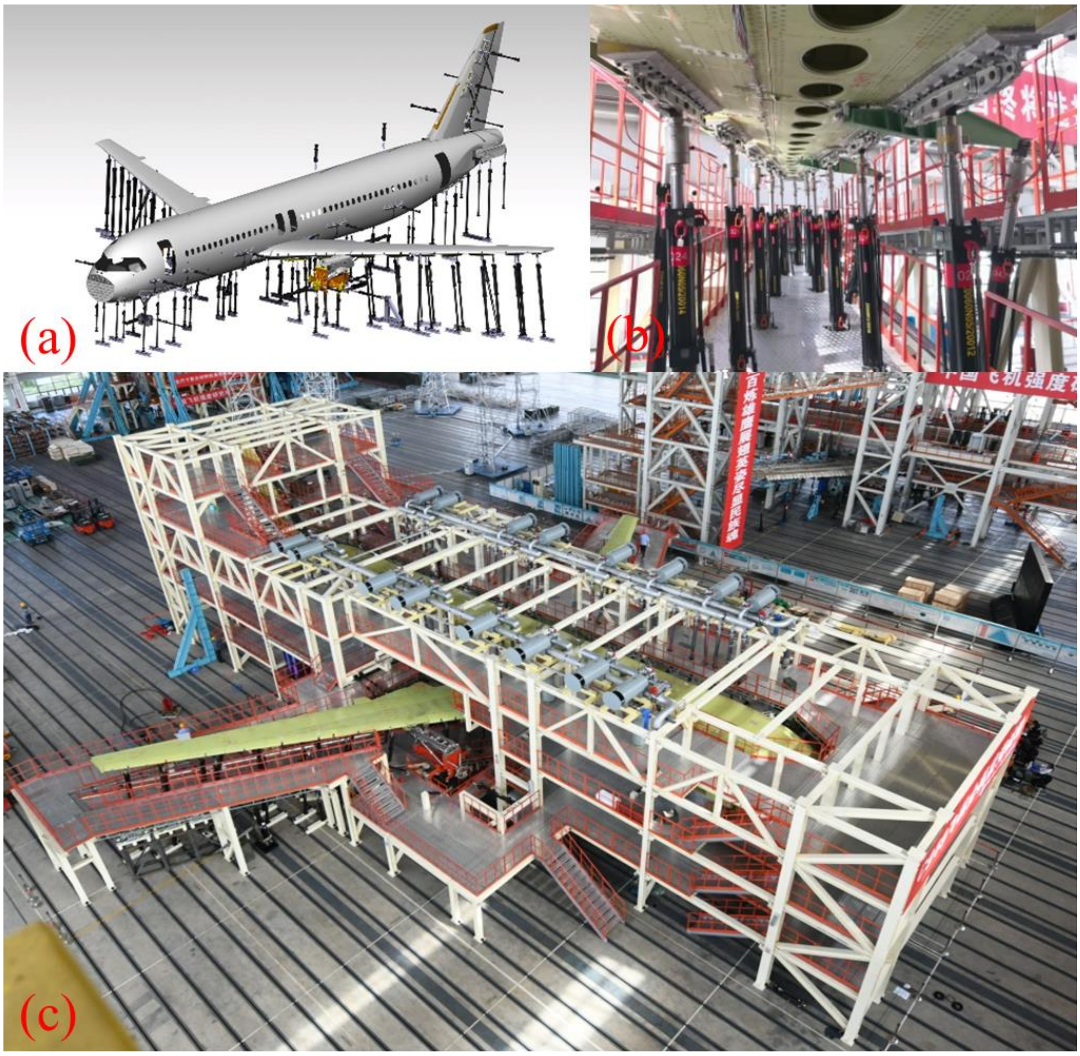

Figure 111: Tension pad-lever system application ((a): Tension pad design application position. (b): Photograph of the wing application. (c): C919 aircraft full aircraft fatigue test.).

Another integrated application case is the C919 aircraft tail/rear fuselage static/fatigue and damage tolerance test, which adopts the same design principles as the C919 full-scale aircraft fatigue test, in which 21 sets of tension pad-lever systems are used, mainly applied to the load application in the rear fuselage vertical direction, rear fuselage lateral direction, vertical tail lateral direction and rudder lateral direction. The test was installed and completed in April 2021, and the 2 times life fatigue test was completed in October 2021, taking 100 days to complete, with an average of 700 cycles per day during the test, and all static/fatigue and damage tolerance tests were completed by March 2023, thus breaking the record for the fastest test of its kind in China. The C919 EF3 test site is shown in Figure 112.

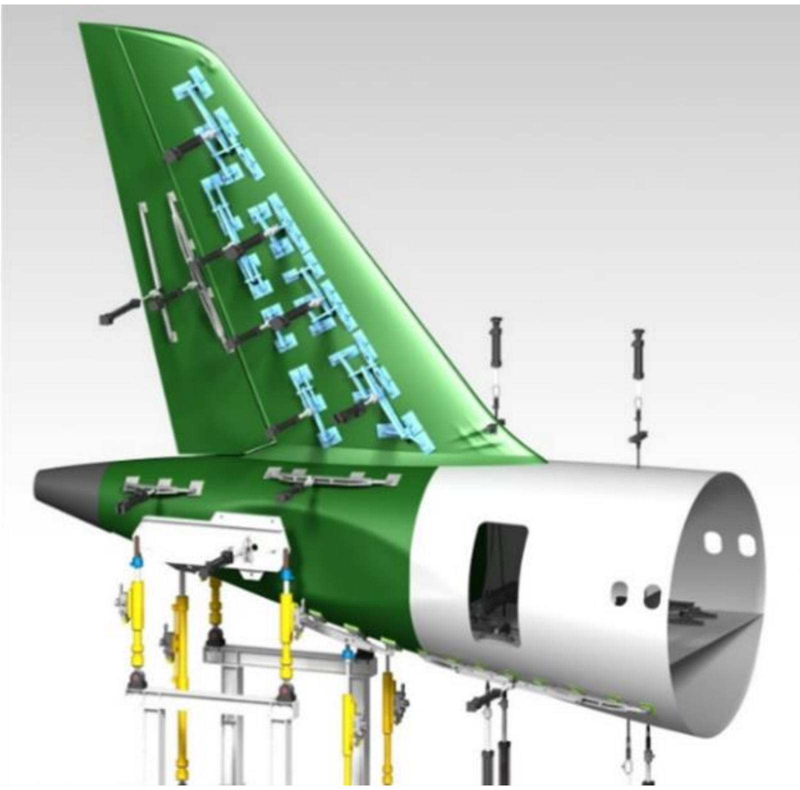

Figure 112: C919 aircraft EF3 test tension pad-lever system application schematic

Test acceleration is a constant pursuit for efficient aircraft development, and ASRI continues to work on efficient verification of aircraft design results, where the development of rigid loading technology has contributed to significant improvements in fatigue test loading efficiency. The new generation of tension pad-lever system solves the challenges of vertical loading of wings and vertical/lateral loading of nose/rear fuselage hyperbolic structures, which can increase the loading rate, reduce the usage and maintenance, make the load simulation more accurate, and make the number of loading points smaller. The integrated application of rigid loading technology shows that the two loading methods work well in the C919 full-scale structural fatigue test and the full-scale structural static/fatigue and damage tolerance test of the tail/rear fuselage, and the C919 full-scale structural fatigue test has achieved a good result of 2000 cycles in the first month of the test while ensuring test safety and test accuracy. The C919 full-scale structural static/fatigue and damage tolerance test has achieved the test results of completing 2 times the fatigue life in 100 days and zero failure of the loading system during the whole test. The successful application of these technologies can provide important reference and support for the subsequent full-scale fatigue tests of other aircraft.

8.4 Widespread Fatigue Damage Test and Evaluation of Equally Straight Section in Fuselage[29]

Firstly, the fatigue and damage tolerance test of the equally straight section in fuselage was introduced, and then according to the "Widespread Fatigue Damage (WFD) Assessment Process and Method", the widespread fatigue damage assessment of the structure of fuselage part was carried out according to the

[29] AVIC Aircraft Strength Research Institute

analysis and test results. The detailed work included: initial selection of WFD-sensitive structural parts and formation of an initial list; then identification according to the WFD-sensitive structural discrimination principle; calculation of the average WFD behavior and determination of ISP and SMP for the parts finally identified as WFD-sensitive structures according to the analysis and test results; and finally, determination of LOV and giving maintenance requirements.

Test overview

The specimen in test was sealed by endplate clamps at both ends, supported by endplates behind the 28 frames, and 7 loading joints were set up on the endplates in front of the 22 frames to apply the load, see Figure 113. Taken into account the vertical sudden wind and maneuvering load, The load spectrum was equivalent to one flight applying one cycle, while applying differential pressure load in normal case, ignoring the influence of other loads, each loading cycle simulated one flight including takeoff and landing.

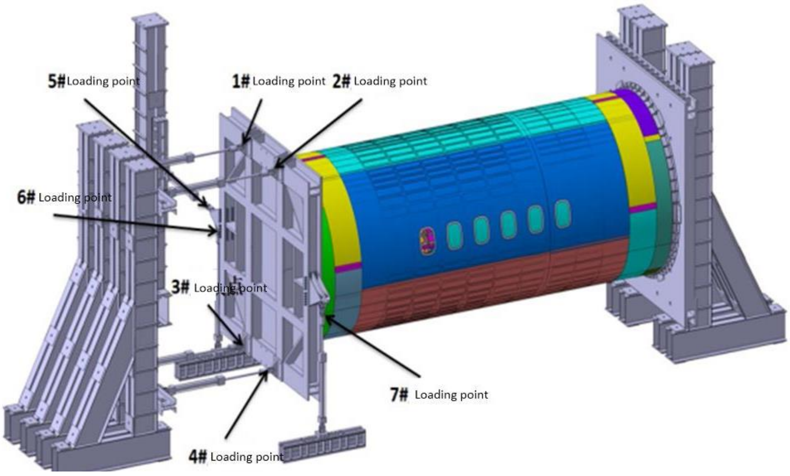

Figure 113: Schematic diagram of the support solution for equally straight section in fuselage

The equally straight section in fuselage completed the fatigue and damage tolerance test and passed the residual strength test assessment. Many cracks appeared in the fuselage frame and window corner skin during the test. The fuselage frame cracks were shown in Figure 114.

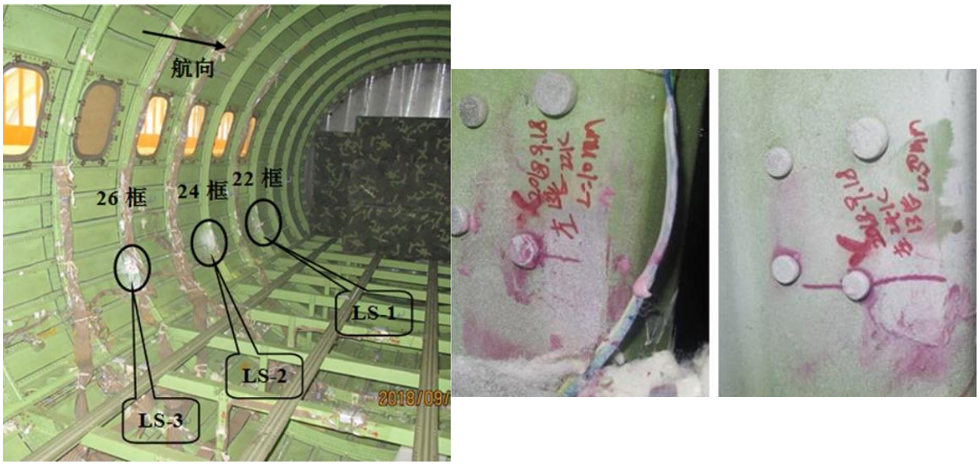

Figure 114: Fuselage frame crack situation

Widespread fatigue damage assessment

The design service goal (DSG) of aircraft structural is 60,000 FC (flight cycles). The equally straight section in fuselage test was designed according to the aircraft DSG. The target LOV is determined as 60,000 FC when carrying out the WFD evaluation of equally straight section in fuselage test parts.

Firstly, the PSE structure was selected and judged whether it belongs to the FCS structure. Then identified the structural details in the structure that were prone to cracking based on design experience. Discriminated against the 16 types of WFD sensitive structure structural items given in AC120-104, initially determine whether they were WFD-sensitive structures, and determine the possible types (MSD/MED) and specific locations. The initial list of WFD-sensitive structures is formed, and stress analysis and fatigue life analysis were performed on these structural parts to finally form the list of WFD-sensitive structures. As a result, the fatigue life of the window frame corners was same and identified as WFD-sensitive structures, as in Figure 115. The fatigue life of the skin and frame corner pieces in the sidewall area were scattered more and were not regarded as WFD-sensitive structures, as in Figure 116.Table 10 shows the WFD sensitive structure list.

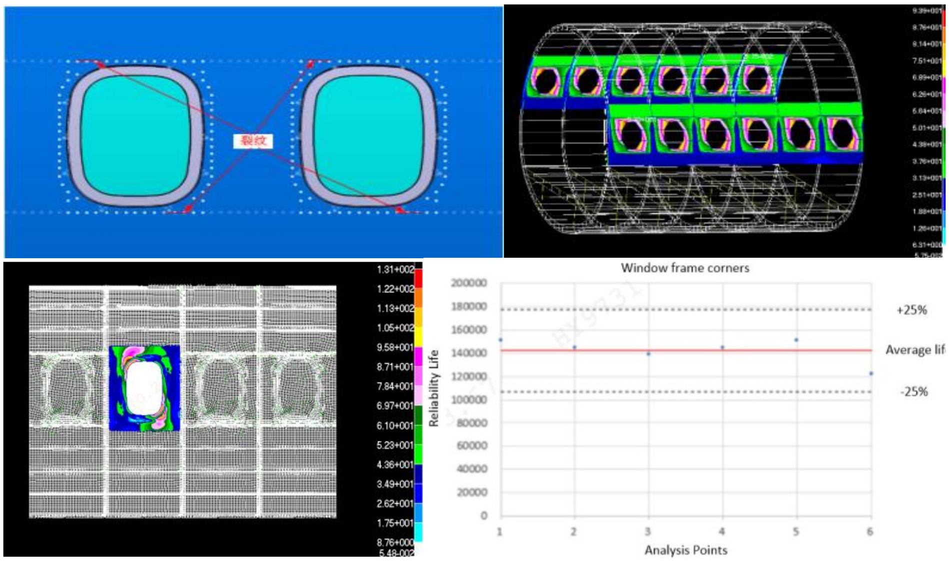

Figure 115: WFD-sensitive structure identification at the corner of the window frame

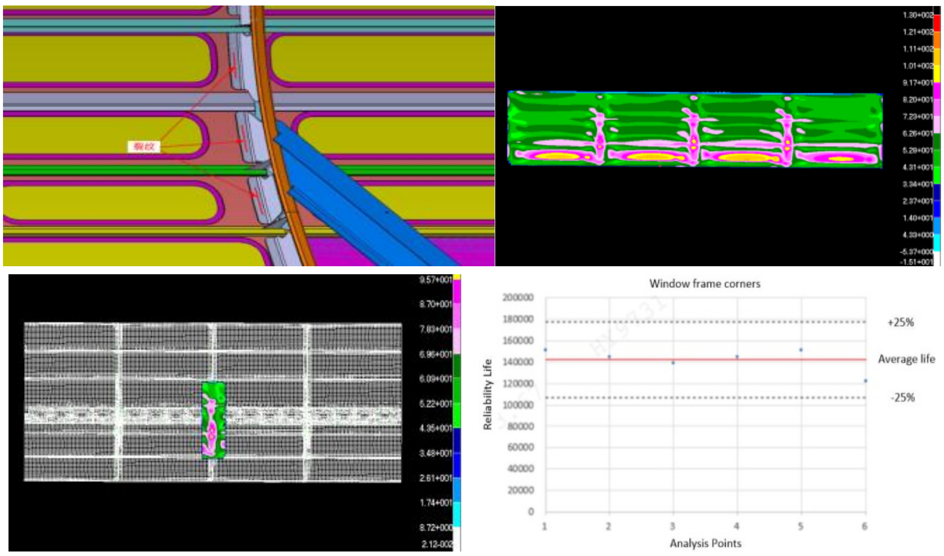

Figure 116: The WFD-sensitive structure identification of the sidewall area skin and the frame corner

Table 10: Table of WFD-sensitive structure of airframe structure

No.	WFD-sensitive structure	No.	WFD-sensitive structure
1	Panel at longitudinal lap （MSD/MED）	4	Connection of stringer to frame （MED）
2	Panel at circumferential joint （MSD/MED）	5	The floating frame cut corner piece is connected to the skin at the end rivet（MSD/MED）
3	Fuselage frame（MED）	6	Window surrounding area （MSD/MED）

Average behavior determination and LOV determination

The widespread fatigue damage average behavior (N_{WFD}) of each structure was determined by fatigue test, deterministic analysis method and probabilistic analysis method for WFD-sensitive structures, and the Inspection start point (ISP) and structural modification point (SMP) were determined according to whether inspection is effective. Finally, the ISP and SMP of each WFD-sensitive structure were plotted in Figure 117 according to the analysis and evaluation results. Compared with the target LOV, The parts which fatigue life was less than the target LOV were two.

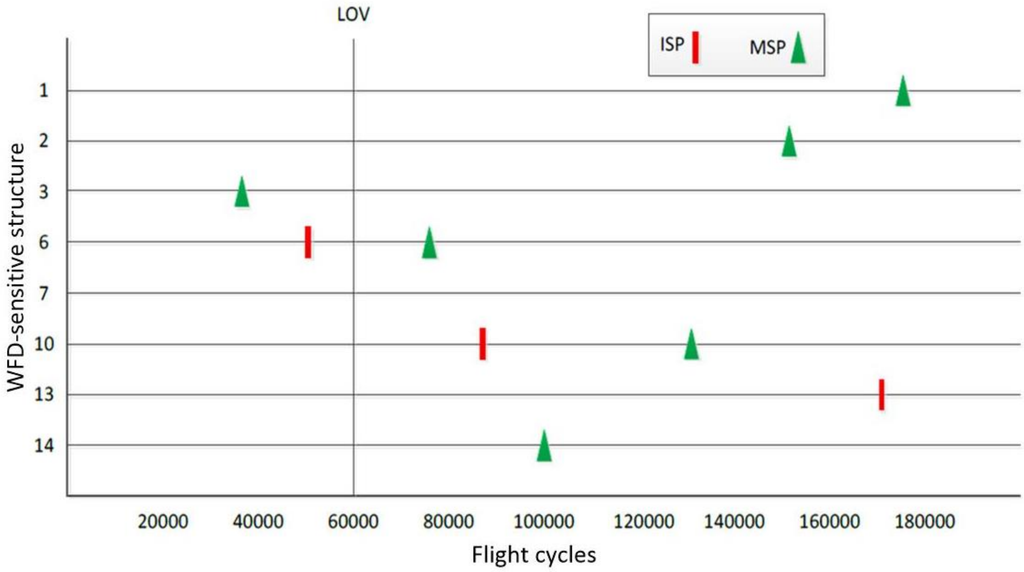

Figure 117: Determination of the LOV of the equally straight section in fuselage

Maintenance Programming

The widespread fatigue damage average behavior of two parts was less than the target LOV. These two parts were frame corner piece connection and skin opening corner in window surrounding area. The inspection of frame corner piece connection was invalid, so it should be repaired before 24875 FC. The inspection of skin opening corner in window surrounding area was valid. ISP is 50675FC and SMP is 76012FC. The skin opening corner in window surrounding area was in the normal inspection, no need additional special inspection. Therefore, an additional part needed to be repaired when the LOV is determined to be 60000FC.